A Computational Study into the Effect of Structure and Orientation of the Red Ear Slider Turtle Utricle on Hair Bundle Stimulus

Julian Ly Davis

Dissertation submitted to the faculty of the
Virginia Polytechnic Institute and State University
in partial fulfillment of the requirements of the degree of

Doctor of Philosophy

in

Engineering Mechanics

Committee:
J. Wally Grant, Chair
Romesh C. Batra
John R. Cotton
Ellengene H. Peterson
Bob L. West

November 30th, 2007
Blacksburg, Virginia

Keywords: Utricle, Finite Element, Computed Tomography, Acceleration

A Computational Study into the Effect of Structure and Orientation of the Red Ear Slider Turtle Utricle on Hair Bundle Stimulus

by

Julian Ly Davis

(Abstract)

The vestibular system consists of several organs that contribute to ones sense of balance. One set of organs, otoconial organs, have been shown to respond to linear acceleration (1949). Hair bundles (and hair cells), which are the mechano-electric transducers found within otoconial organs, respond to displacement of the overlying otoconial membrane (OM). Structure, position and orientation of the OM within the head may influence the stimulus of hair bundles by changing the deformation characteristics of the OM. Therefore, studying the deformation characteristics of the OM with finite element models presents a unique advantage: the ability to study how different variables may influence the deformation of the OM.

Previous OM models have ignored complicated OM geometry in favor of single degree of freedom (De Vries 1951) or distributed parameter models (Grant et al. 1984; Grant and Cotton 1990; Grant et al. 1994). Additionally, OMs have been modeled considering three dimensional geometry (Benser et al. 1993; Kondrachuk 2000; 2001a), however OM layer thicknesses were assumed to be constant. Further, little research has investigated the effect of position and orientation of otoconial organs on the deformation of the OM (Curthoys et al. 1999), due to natural movement of the head.

The effect of structure, position and orientation of the utricle of a red ear slider turtle on the stimulation of hair bundles in the OM is investigated here. Using confocal images, a finite element model of the utricle OM is constructed considering its full 3D geometry and varying OM layer thickness. How specific geometric variables, which are missing from other OM models, effect the deformation of the utricle OM is studied. Next, since hair bundles are part of the structure of the OM, their contribution to the deformation of the utricular OM is quantified. Then, using computed tomography of a turtle head and high speed video of turtle feeding strikes, acceleration at the utricle during natural motion is estimated. Finally, the effects of orientation of the utricle in the head on the stimulus of hair bundles within the organ is investigated.

In summary, a model and methods are developed through which deformation of the turtle utricle OM through natural movements of the head may be studied. Variables that may contribute to utricle OM deformation are investigated. Utricle OM geometry, hair bundles, position and orientation all play a role in utricle OM deflection and therefore hair bundle stimulus. Their effects are quantified and their roles are discussed in this dissertation.

Acknowledgments

First, I would like to thank my committee for the help, time, and stimulating conversations through out my time here, at Virginia Tech. I have always enjoyed talking with you about research, school or just life in general. I have learned so much. Thank you.

Secondly, I would like to thank all of my friends who have supported me through my schooling. There are too many to count, but I thank you all for your support though these many years.

Last, but certainly not least, I would like to thank my family for all of their support through the recent years. It has been a long and tough road, but my family was there to support me every step of the way. Thank you.

Table of Contents

List of Figures

List of Tables

List of Equations

CHAPTER 1. Introduction

ABSTRACT

This research focuses on an otoconial organ in the inner ear called the utricle. The utricle is a single organ in system of organs that constitute the vestibular system. The whole system is responsible for detecting movement of the head. In this chapter, structure of utricle is illustrated and discussed. In addition, previous work related to testing and modeling otoconial organs will be reviewed and the need for more detailed finite element models will be discussed.

1.1 Significance

Over 90 million Americans have had problems with dizziness or vertigo (2007), and approximately 8 million, have reported chronic problems, lasting 3 or more months (2006). Medical costs associated with caring for those with balance problems have reached over 1 billion dollars per year in the United States. In addition, dizziness is commonly reported in 30 percent of the adults over the age of 65 in the United States (2007). The medical costs associated with injuries from falls in adults over the age of 65 due to balance disorders are reported to be in the range of 8 billion dollars per year (2006).

Problems with the vestibular system, which senses balance, can be the cause for many injuries and can lead to much discomfort (NIDCD 2007). Semicircular canals are part of the vestibular system and have been researched since as far back as the 1800s (Highstein et al. 2004). It has only been since about 1950 (De Vries 1951), that another part of the vestibular system, otoconial organs have been investigated.

Before we can begin to diagnose or treat problems with balance we must first understand how the system works. This research is aimed towards understanding how otoconial organs work. We are focus specifically on the utricle because it is thought to respond only to vestibular cues whereas the saccule has been shown to respond to acoustical cues (Ashcroft and Hallpike 1934; Fay 1984; Fay and Edds-Walton 1997; Lowenstein and Roberts 1949; Lowenstein and Saunders 1975).

1.2 Otoconial Organs

The vestibular system is located in the inner ear of vertebrates and is responsible for sensing movement. It consists of two subsystems: otoconial organs to detect linear movement and semicircular canals to detect rotational movement. The semicircular canal subsystem is made up of three circular shaped fluid-filled canals positioned in approximately orthogonal planes in the head. As the head rotates, fluid in the canals lags behind the motion of the head and canals. This results in deflection of hair bundles, fixed in a gelatinous cupula (see figures 1 & 2 in (Jorgensen 1974)), located at the ends of the canals. Deflection of the hair bundles activates the hair cells to which the bundles are

attached and these hair cells transmit a signal to the central nervous system (CNS) in response to angular acceleration (Highstein et al. 2004).

The otoconial organ subsystem (Lagena, Saccule and Utricle) of the vestibular system works in a similar fashion to the semicircular canals. However, these organs do not respond to angular acceleration, instead, they respond to linear acceleration (De Vries 1951; Lowenstein and Saunders 1975). Linear motion of the head results in a lag of the otoconial layer of the utricle behind motion of the head. This bends the hair bundles contained in the organ leading to a depolarization of the hair cell to which the bundle is attached (Kachar et al. 1990). This depolarization of the hair cell then activates the neurons attached to the hair cell and transmits a signal to the CNS proportional to linear acceleration.

1.2.1. Otoconial Membrane (OM) Layered Structure

Otoconial organs have a neuroepithelium containing the cell bodies of hair cell (HC) receptors (see **A**). Each hair cell bears a hair bundle (HB) which contacts the complex gelatinous structure (Xue and Peterson 2003), the otoconial membrane, overlying the upper surface of the neuroepithelium (the macula). Hair bundles are contained in cylindrical pockets of the column filament layer (CFL). Some hair bundles have tall cilia that protrude into the overlying otoconial membrane, while others have shorter cilia.

The OM is comprised of three layers: an otoconial layer (OL), consisting of calcium carbonate crystals embedded in a gelatinous structure; a compact gel layer (GL), and a CFL, consisting of a dense network of 20 nm diameter filaments cross-linked with 12 nm filaments (Kachar et al. 1990) (see **A**). Accelerations and gravity act on the higher density OL, shearing the CFL and GL with a magnitude of displacement proportional to the vector component of acceleration acting in the plane of the otoconial organ. Shearing of the CFL and GL (**B**) displaces the hair bundles within these layers. The hair cells then translate bundle displacement into receptor potentials that modulate neural signals to the central nervous system.

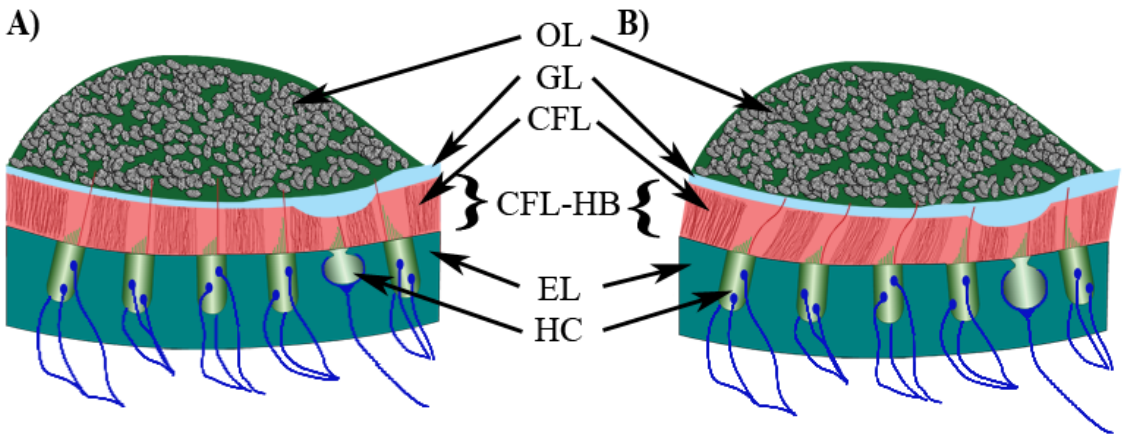

Figure 1: Schematic Cross Section of The Layered Structure of Utricle

This is a representative diagram of the layered structure in the Lateral-Medial Transect of the utricle (Lateral to the right and Medial to the left). From the top down, the layers are labeled: OL for the otoconial layer; GL for the compact Gel Layer; CFL for the column filament layer; and EL for the Epithelial Layer.

Also indicated in this figure are nerve endings in blue which attach to Hair Cells (HC), residing in the epithelial layer. There are two types of hair cells: Type I and Type II. Type I hair cells are rotundly shaped and are only found in the striolar region. Type II hair cells are cylindrically shaped and are generally found in the all over the utricle maculae.
A) shows an undeformed state with the lateral to the right and the medial to the left. In B) a deformed state of the utricle is shown. The otoconial layer shears the column filament and compact gel layers in response to linear acceleration or head tilt.

Note: For clarity, when referring to the CFL and hair bundles together, I will use CFL-HB complex.

1.2.2. Macuale Shape

Otoconial organs are varied in shape and size across species. (Lewis et al. 1985) In particular, the macular surface of otoconial organs can sometimes be flat (mammals) or curved (turtles) and the macular perimeter (outline of the macular surface as seen from above – see) of the utricle can also vary greatly depending on the species. Utricles have a large variety of macular perimeter shapes. They range from somewhat square with an elongated ends in birds, to oval with extended medial ends in reptiles, to kidney-bean shaped in mammals (Lewis et al. 1985).

Otoconial organs are dynamic as well as static sensors, transducing linear acceleration and head tilt (Lowenstein and Roberts 1949; Lowenstein and Saunders 1975) through OM displacement. They have also been tested through direct stimulus of the OM and the response measured via microphonic potentials (Corey and Hudspeth 1979; 1983a). In mammals, there are typically two otoconial organs: the saccule and utricle.

These organs are oriented to detect changes in linear acceleration in planes that are approximately oriented vertically and the horizontally (Lewis et al. 1985). Changes in OM structure, through the macular and OM shape, or different hair bundle morphology, may effect the stimulus of hair bundles within the otoconial membrane.

1.2.3. Otoconial Membrane Modeling

Otoconial membrane models have been used to investigate how otoconial organs operate. They range from the simple single degree of freedom models (De Vries 1951) to more complicated distributed parameter models (De Vries 1951; Grant and Best 1986; Grant et al. 1984; Grant and Cotton 1990). Missing from these early models is adequate geometry of the organ structure. Several models consider only two dimensional uniformly distributed geometry of the OM when constructing the models. Recently, however, there have been efforts made to include macular perimeter and curvature in the models of otoconial membranes (Jaeger and Haslwanter 2004; Jaeger et al. 2002; Kondrachuk 2001a). Now, using confocal images of carefully sliced cross sections of the turtle utricle, I assembled a geometrically accurate model of the utricle OM structure.

1.3 Hair Bundles (HBs)

1.3.1. Hair Bundle Structure

Hair bundles consist of several hexagonally arranged stereocilia and a single kinocilium that extend from the apical surface of a hair cell. The stereocilia are arranged in a “staircase–like” pattern: decreasing in height with respect to increasing distance from the kinocilium. The kinocilium and all stereocilia are attached to each other via (protein) linkages (**B**), at several locations on the stereocilia. Hair cells are stimulated when hair bundles are deflected along their E-I (excitatory-inhibitory) axis (**A)**.

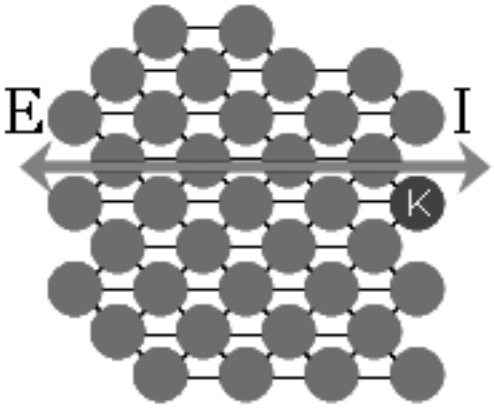

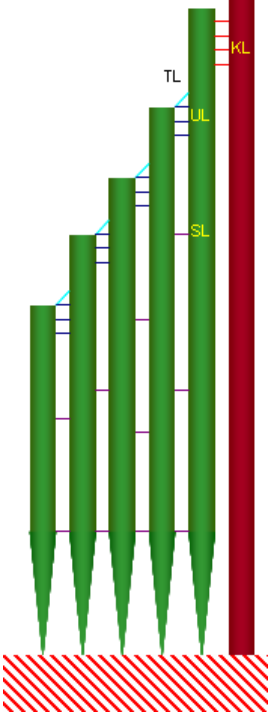

A) Top view of turtle utricle HB B) Side View of a generic HB

Figure 2: Hair Bundle Structure

In A) the top view of a turtle utricle hair bundle is shown. Stereocilia are indicated with circles, the kinocilium is marked with a K, and the Excitatory-Inhibitory (E-I) axis is shown with an arrow. Deflections in the excitatory direction along this axis will maximally stimulate the hair cell to which the bundle is attached. Deflection perpendicular to this axis will not excite the hair cell. In B) a side view of the hair bundle is shown indicating the extracellular links between stereocilia and the kinocilium.

Kinocilium = dark red	Stereocilia = green
TL = tip links	SL = shaft links
UL = upper lateral links	KL = kinocilia links

1.3.2. Hair Cell Activation

Deflection of hair bundles within the OM opens ion channels located on the individual stereocilia allowing primarily calcium or potassium ions to flow into the hair cell (Highstein et al. 2004).The result of this inward ion flow is the depolarization of the

hair cell to which the hair bundle is attached. Once depolarized, a synaptic response between the hair cell and the nerve ending attached to the hair cell occurs (). This response is transmitted through a nerve to the central nervous system (CNS). The frequency of this signal is proportional to the magnitude of the deflection within the OM. Information is also transmitted through the regularity or irregularity of the spacing of the output spikes measured from the neuron (Goldberg et al. 1990).

1.3.3. Turtle & Bullfrog Hair Bundles

The turtle utricle is divided into 4 zones that can be distinguished by hair bundle structure and hair cell afferent terminals. The striola region, marked Zones 2 and 3 (– Arrow heads), is an arched band of bundles that can be distinguished by features of the hair bundles themselves (Moravec and Peterson 2004).

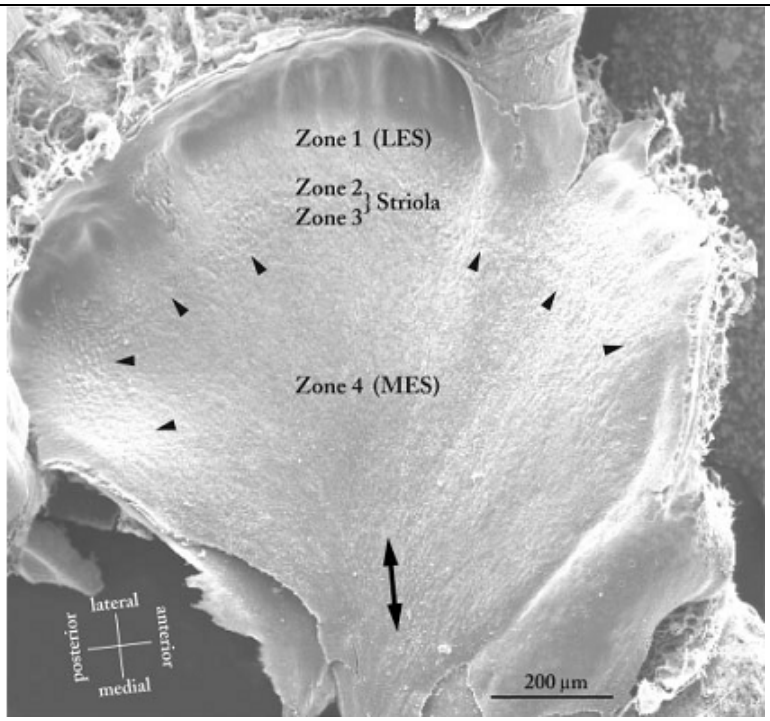

Used with permission (Rowe and Peterson 2006)

Figure 3: Top View of Turtle Utricle – HBs are removed via sonication

This is a top view of the utricle (from:(Rowe and Peterson 2006)) whose OM layers, shelf, & HBs (via sonication) have been removed. This figure also labels the different regions in the utricle: striola, medial extrastriola (MES – Zone 4) and lateral extrastriola (LES – Zone 1). The striola is further broken down into Zones 2 and 3. Zone 3 is the only region that contains Type I cells.

Type I striolar hair bundles have on average 96 stereocilia (Moravec and Peterson 2004) arranged in a hexagonal pattern. One of their distinguishing features is their large

array widths (median width = 2.55 μm) (Rowe and Peterson 2006) and their small KS ratios (ratio of kinocilium height to tallest stereocilia height) (Xue and Peterson 2006). The large number of stereocilia, along with the bundle's wide base, contributes to the bundle's relatively high stiffness: measured to be on the order of 45 μN/m (Spoon et al. 2005). Some striolar bundles are associated with Type I hair cells, which are rotundly shaped and are found only in Zone 3 (Moravec and Peterson 2004).

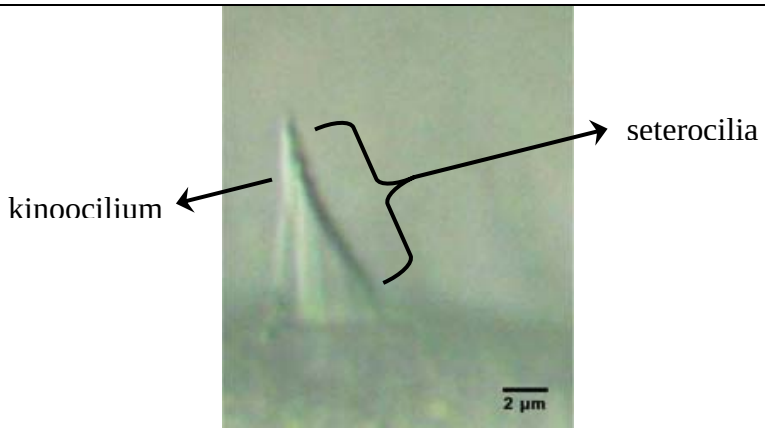

Figure 4: Light Microscope Picture of Striolar HB

Striolar hair bundles in the turtle utricle have kinocilia that are on the same order of height as their tallest stereocilia. They also have a large number of stereocilia (~96) that make up the bundle.

Extrastriola regions, Zones 1 and 4, on the lateral (LES) and medial (MES) side of the striola region respectively, have Type II hair cells with bouton afferent endings. In contrast to the striola, extrastriolar hair bundles have on average 51 stereocilia (Moravec and Peterson 2004) arranged such that an extrastiolar hair bundle has a smaller array width (median width = 1.15 μm) (Rowe and Peterson 2006) and a larger KS ratio than bundles found in the striola (Xue and Peterson 2006). Thus, extrastriolar hair bundles are weaker than those found in the striola, with stiffness measured between 9 and 12 μN/m (Spoon et al. 2005).

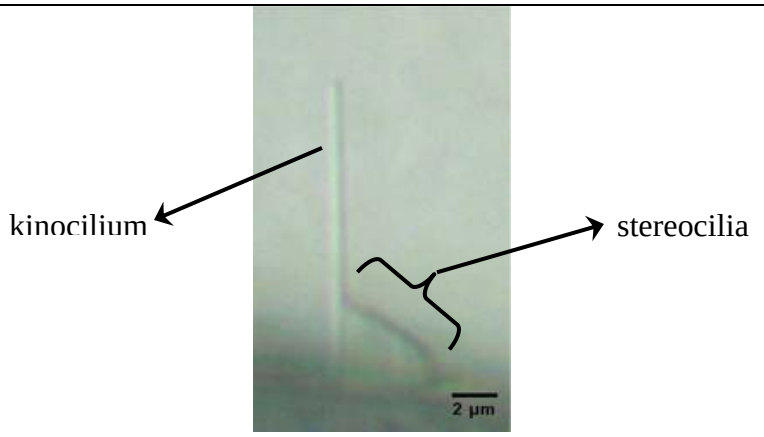

Figure 5: Light Microscope Picture of medial extrastriolar HB
Medial extrastriolar hair bundles tend to have taller kinocilia than their counterparts in the striolar and fewer (~51) stereocilia.

In addition, the LES bundles have been shown to have a similar range of stiffness as MES bundles (Spoon et al. 2005). Therefore, when considering hair bundles in this work, only a distinction between striolar and Extrastriolar is considered.

Bullfrog saccule hair bundle structure is similar throughout the maculae (Benser et al. 1993; Hillman and Lewis 1971). They are generally stout hair bundles with KS ratios near 1. Their stiffness is on the order of 500-900 μN/m (Benser et al. 1993; Kondrachuk 2000).

1.3.4. Hair Bundle Count

There are generally several thousand hair bundles in an otoconial organ, depending on the size of the macular surface of the organ (Severinsen et al. 2003). In the bullfrog saccule, the number of hair bundles have been estimated to be around $6x10^9$ per/m^2 on the maculae (Kondrachuk 2000; Trincker 1962). Based on Benser et al. (1993), and Kondrachuck's work (estimated bullfrog saccule maculae area = .2484 mm^2) (Kondrachuk 2000), this translates to about 1490 hair bundles in the bullfrog saccule maculae.

From Severinsen et al. (2003), the total number of hair bundles in the turtle utricle model is estimated to be about 8670 bundles. This is calculated from a macular area in the utricle model of 0.80446 mm^2 and the equation () prescribed in Severinsen et al. (2003), where the number of hair bundles (# of HBs) is linearly proportional to the utricular macular area (A_{UM}) in square millimeters.

$$\#\text{ of HBs} = (A_{UM} \text{ in } mm^2)/\ 92.8\ E\text{-}6$$

Equation 1: Number of Hair Bundles per macula area for Red Ear Slider Turtle

1.4 Research Goals and Dissertation Overview

Aspects of the utricle OM that may contribute to changing the response measured from hair cells are studied in this research. Microphonic potentials have been measured as a result of direct (bullfrog) (Corey and Hudspeth 1979; 1983a; b) and indirect (fish-haddock) (Enger et al. 1973) stimulus of the saccule OM. In addition, previous experiments and models have quantified the response of turtle utricle hair bundles to experimental stimuli (Nam et al. 2005a; b; Nam et al. 2006; Silber et al. 2004; Spoon et al. 2005). Some of the blanks between natural and experimental stimulus of hair bundles may be filled using FE models, computed tomography, and high speed videos of turtle head movement. Eventually the response of hair bundles to a natural gravtioinertial stimulus of the turtle utricle OM may be quantified, but first the variables that may influence this displacement are investigated.

In this study, the effects of these 3 aspects of the OM that may modulate the neural response from the utricle are quantified. First, the effects of structural geometry of the OM are investigated using eight systematically varied finite element models whose geometry varies between including and excluding 1) macular curvature, 2) varying OM layer thickness and 3) macular perimeter. Secondly, hair bundles themselves may contribute to the total stiffness of the OM sublayers, thereby limiting their deflection. Two utricle OM models, including both explicit and implicit hair bundles, are used to quantify the stiffness contribution of hair bundles to shearing of the utricle OM. Third, the effect of position and orientation of the utricle OM within the turtle skull is investigated. Computed tomography is used in conjunction with a finite element model of the turtle utricle OM, to determine change in the stimulus imparted to the utricle OM due to head orientation.

CHAPTER 2. Layer Thickness and Curvature Effects on Utricle Deflection in the Red Ear Slider Turtle

ABSRACT

Finite element models of a turtle utricle otoconial membrane (OM) were developed to investigate the effects of three geometric variables on static and modal response of the OM: 1) curvature of the macular surface, 2) spatial variation in thicknesses of three OM layers, and 3) shape of the macular perimeter. A geometrically accurate model of a turtle utricle was constructed from confocal images. Variants of this model were formed by modifying values for each variable: modeling the macula surface as flat, OM layer thicknesses as spatially invariant, and the macular perimeter as a rectangle. Static tests were performed on each modified OM model, and the results were compared to determine the effects of each geometric variable on static mechanical gain (deflection at CFL/GL interface below center of mass of OL per unit acceleration). Results indicate that all three geometric variables affect the magnitude and directional properties of OM static mechanical gain. In addition, through modal analysis, the natural frequencies and displacement modes of each model are determined. The displacement modes illustrate the effects of the three geometric variables on OM dynamics. This study indicates the importance of considering three-dimensional OM geometry when attempting to understand responses of the OM and, therefore, the modulation of hair cell signals to accelerations during head movements.

2.1 Introduction

The otoconial organs of vertebrates are dynamic as well as static sensors. They transduce linear acceleration and head tilt. The utricle, one of these otoconial organs, has a neuroepithelium containing the cell bodies of hair cell receptors. Each hair cell bears a hair bundle, composed of multiple stereocilia and a single kinocilium, on its apical surface. These hair bundles contact a complex gelatinous structure, the otoconial membrane, which overlies the upper surface of the neuroepithelium (or macula). The OM, in turn, is comprised of three layers (see **A**): an otoconial layer, a compact gel layer, and a column filament layer. Accelerations and gravity act on the higher density OL, shearing the CFL and GL with a magnitude of displacement that is proportional to the component of acceleration acting in the plane of the otoconial organ. Shearing of the CFL and GL (see **B**) displaces the hair cell bundles. The hair cells then translate bundle displacement into receptor potentials that modulate neural signals to the central nervous system.

Initially, otoconial organs were mathematically modeled as flat bodies with uniform OM layers, usually ignoring three dimensional geometry in favor of two or even one dimensional models (De Vries 1951; Hudetz 1973; Kondrachuk 2001a). The first model to describe the motion of an OM was a 2^{nd} order lumped parameter model (De Vries 1951). Studying the otoconial organs of a fish statically and dynamically, this model was used to estimate the stiffness of the OM-bundle complex in each otoconial organ (utricle, saccule and lagena) with a static test, and damping in the saccule with a dynamic test. Dynamic measurements for the saccule were deemed more reliable than those for the utricle and lagena due to larger displacements in the saccule.

The utricle has also been modeled as having a flat neuroepithelium, a single-layered OM, and a curved OL perimeter (Hudetz 1973). The OL perimeter, when seen from a top view, defines the perimeter of the utricular macula (see). Single fiber discharge rates from a utricle in response to static pitch (i.e. nose up and nose down) and roll (i.e.: side up and side down) rotations, observed by Lowenstein and Roberts (1949), were qualitatively matched in the gel layer deflections in this finite difference model:

thus implying a connection between gel layer deflection and response of the hair cells in the utricle.

Distributed parameter dynamic OM models were developed that included the effects of viscosity of the CFL and GL as well as the surrounding endolymph (Grant et al. 1984; Grant and Cotton 1990; Grant and Best 1987). Treating the OM as a single degree of freedom model with uniform OM layer thicknesses and a neuroepithelium and OL that were flat and rigid, the full analytical partial differential equations describing its dynamic behavior were derived and solved. This analytical time domain solution was later transformed into the frequency domain so that different response-stimulation relationships could be investigated (Grant et al. 1994).

It was not until 2000, that material properties were determined from experiments on the bullfrog saccule. The CFL and GL from a bullfrog saccule were represented with a parallelepiped finite element (FE) model that considered separate but uniformly thick OM layers (Kondrachuk 2000). Displacements in this FE model were compared with the experimentally measured OM deflections from tests performed by Benser et al. (1993). The results of this comparison yielded Young's moduli of the CFL (E=250 Pa) and GL (E=6.6 kPa) for the bullfrog saccule. A curved macular perimeter was later considered in an FE model of a guinea pig utricle; however, curvature of the macular surface and varying thicknesses of the individual OM layers were not included (Kondrachuk 2001a).

More recently, macular curvature of otoconial organs has been considered (Jaeger and Haslwanter 2004; Jaeger et al. 2002). While still modeling uniformly thick OM layers, these models of a human utricle and saccule are the first to include curvature of the macular surface. Curvature in a small region of the macular surface (300 μm length x 300 μm width) with uniformly thick OM layers above the curved macula was considered in Jaeger et al.'s (2004) work. They concluded that local curvature of the macular surface reduces the amplitude of displacement within the organ over the frequency range investigated. However, these models of the utricle and saccule did not consider curvature of the whole macular surface.

The objective of this study is to analyze the effects of three-dimensional macular and OM geometry on the global response of the OM to linear accelerations, such as those that are generated by head movements and gravity. It is important to understand these

phenomena because macular and OM geometry influence the deflection and therefore stimulation of hair bundles. The influence of three geometric variables on displacements in the OM are investigated: 1) curvature of the macular surface, 2) varying thickness of the OM layers, and 3) macular perimeter (estimated from the perimeter of the OL as seen from above). A detailed FE model of a turtle utricle is developed directly from confocal images. The model is modified to investigate the effects of changing these three geometric variables.

This study shows that including such geometric details results in changing how the OM deforms in shear and, therefore, can affect the stimulus applied to hair cell bundles. The results of changing the geometry are manifest in the static and modal response of the OM models. Statically, effects on the magnitude of OM static mechanical gain, and on its maximum and minimum deflection directions are observed. Dynamically, effects of these geometric variables are observed in changes to the modal response: natural frequencies and displacement modes.

2.2 Methods

2.2.1. Confocal Images

Utricle preparation and confocal imaging was performed by Jing-bing Xue at Ohio University. The following 3 sections, written by Dr. Peterson (2.2.1.1 Specimen Preparation, 2.2.1.2 In-Vivo Dimensions & 2.2.1.3 Imaging), were adapted from our paper (Davis et al. 2007). It is necessary to include these sections here to express the care that was taken to preserve in-vivo dimensions of the utricle OM.

2.2.1.1. Specimen Preparation

Utricles from two turtles (carapace lengths 4.74 and 5.5 inches) were used to quantify dimensions of the otoconial membranes. Turtles were sacrificed via intramuscular injection of 0.5 ml Euthasol followed by intracardiac perfusion. The guidelines of the Ohio University Animal Care and Use Committee were followed in all experiments. Otoconial membranes are bathed in artificial endolymph *in vivo*. To retain as closely as possible to the *in vivo* condition, 0.065 mM $CaCl_2$ artificial endolymph (AE) was used in all stages of tissue processing (KCl: 140 mM; $CaCl_2$: 0.065 mM; K-HEPES:

5 mM; Glucose: 4 mM; adjusted to pH 7.4 with HCl; (Crawford et al. 1991)). Following a brief intracardiac rinse with AE, turtles were perfused for 30 minutes with 7.4% (W/W) formaldehyde solution (170 ml AE with 40 ml 37% formaldehyde), bisected the head, exposed the labyrinth, and immersed it in this fixative overnight.

One utricle was prepared as a whole-mount (). Following overnight fixation, the utricle was removed, pinned it in a dish filled with AE, opened the vestibule, and removed the falx that overlies the lateral macula (Fontilla and Peterson 2000). Otoconial membranes were visualized by staining them for 3 days using wheat germ agglutinin (WGA) conjugated to Oregon Green 488 (Molecular Probes; 0.1 mg in 1 ml AE).

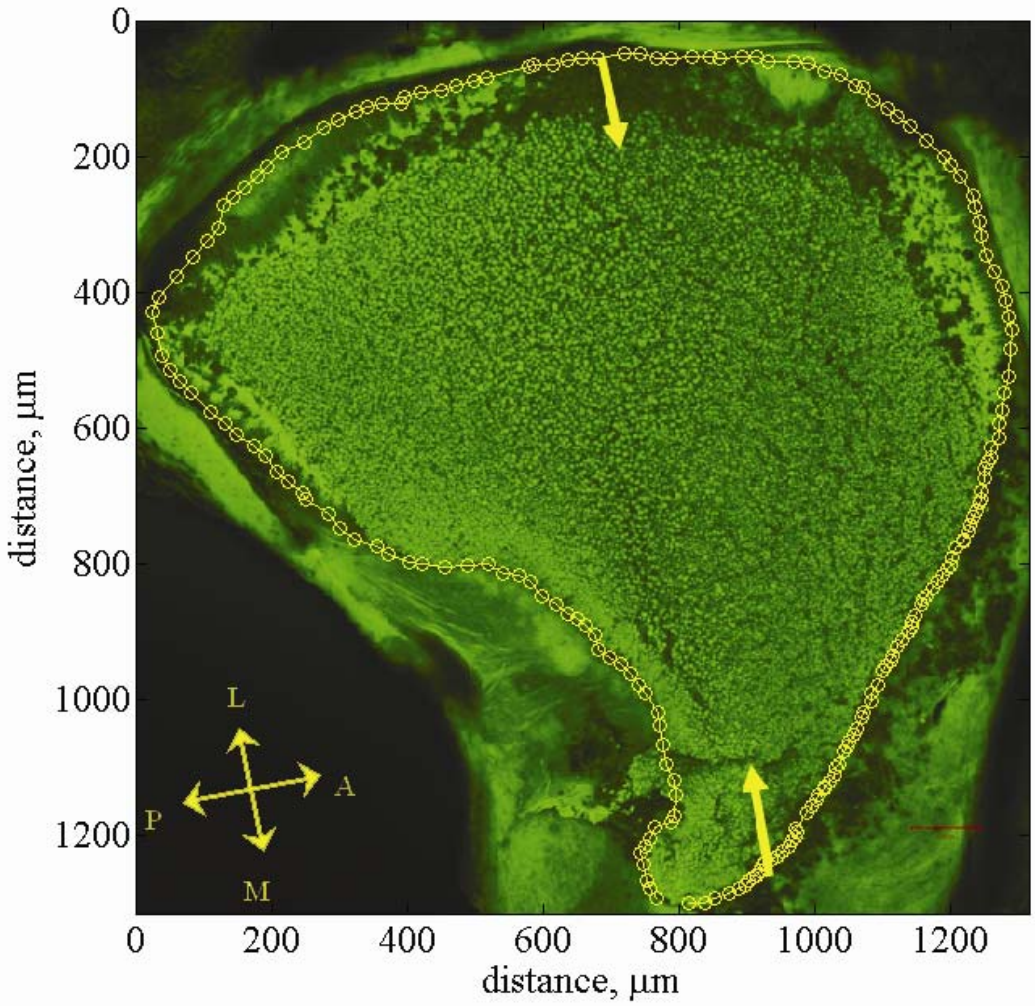

Figure 6: Utricle Whole mount with Macular Perimeter

This figure shows a confocal image of a utricle whole-mount (Xue & Peterson 2003). This whole-mount provides a top down view of the left utricle. The falx overlying the lateral macula is removed but the otoconial layer left intact. The otoconial layer is stained green using WGA. Yellow arrows indicate the lateral-medial transect. Yellow circles indicate the outline of the macular surface. This outline is called the macular perimeter. The macular perimeter is used as a guideline for placement of cross sections in model generation. Approximate anatomical directions are indicated with the double headed arrows. The letters L, M, A, and P indicate the Lateral, Medial, Anterior, and Posterior directions respectively. The striolar is a region about 75 microns wide and starts about 100 microns in from the lateral edge. It is arched from anterior to posterior following the curve of the lateral edge of the utricle (see). The lateral extrastriola region is lateral to this arched region. The medial extrastriola region is medial to this arched region.

2.2.1.2. In Vivo Dimensions

Two strategies were used to ensure that measurements reflect *in vivo* conditions as closely as possible. First, the tissue was fixed with formaldehyde but not dehydrated. Aldehyde fixation alone causes no significant dimensional changes in auditory tectorial structures (Edge et al. 1998). Second, the tissue was only exposed to appropriate electrolites with correct osmotic concentrations, at the proper pH: artificial turtle endolymph with 65μM Ca^{2+} at physiological pH (Crawford et al. 1991). This is important because inappropriate concentrations, especially elevated calcium concentrations or extreme pH levels, can cause swelling or shrinkage of tectorial structures in several vertebrates including reptiles (Freeman et al. 1994; Freeman et al. 1997; Freeman et al. 1993; Shah et al. 1995).

2.2.1.3. Imaging

Utricular slices were used to visualize macular curvature and to measure the thickness of the three otoconial membrane layers. Both utricles were removed from one turtle and embedded using 4% low melting point agarose (Bio Rad) in AE. The left utricle was sliced in the plane designated by yellow arrows in . This slice is called the lateral-medial (LM) transect (**Figure 7**). Measurements of otoconial membrane thickness were taken from a single, 100 μm thick slice along this line (Fontilla and Peterson 2000).

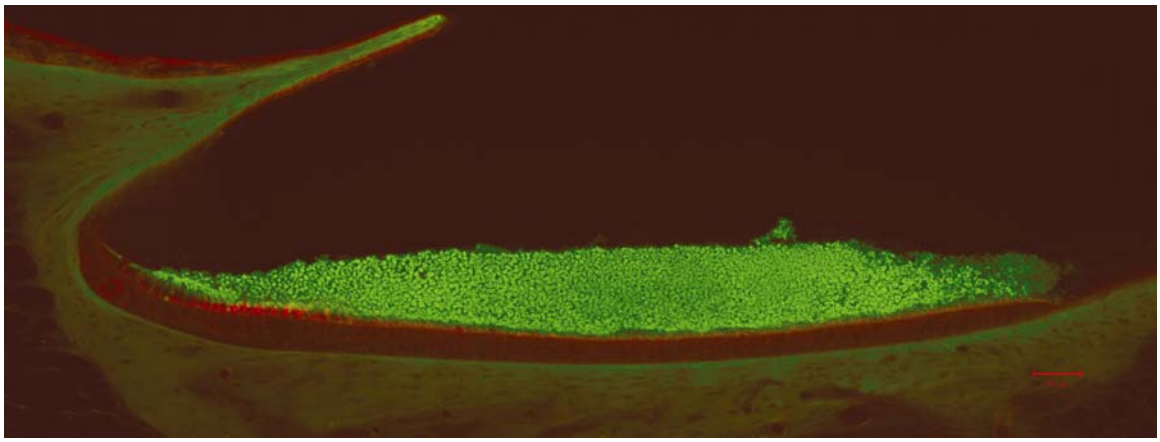

Figure 7: Confocal Image of Lateral-Medial Transect

This figure shows a confocal image of the lateral-medial transect of the left utricle (scale bar = 50 μm) (Xue & Peterson 2003). The otoconial layer is stained green and the epithelial layer is stained red. Clearly visible in this image is the curvature of the LM transect. This figure was enlarged and the top of the epithelial layer was visually fit at approximately 50 microns increments to determine macular curvature in this plane. This figure is also used to determine individual layer thicknesses in the LM transect.

To determine macular curvature and the shape of the OM across the surface of the utricle, the right utricle was sectioned serially, in a plane perpendicular to the LM transect, i.e., approximating the anterior-posterior (AP) plane. These slices are called the orthogonal cross sections. All utricular slices were stained with WGA as described above, followed by phalloidin-Alexa Fluor 633 (Molecular Probes; 10μm of in 400ul AE) for 1 hour to visualize hair bundles.

Utricular whole-mounts and slices were imaged using an upright Zeiss LSM 510 confocal microscope. A Plan-Neofluar 10x objective for low magnification images of the utricular whole-mount and all slices, and a Zeiss C-Apochromat 63x water immersion objective (N.A. = 1.2) was used to collect high magnification images of the transect. Zeiss LSM 510 software (ver 3.0) was used to measure the relative thickness of the three otoconial membranes across the LM transect.

2.2.2. Finite Element Models

2.2.2.1. OM Model Assembly

First an anatomically correct and dimensionally accurate OM model was constructed directly from the confocal images. This process was performed using a

custom Graphics User Interface written in Matlab™ (ver. 7.2.0.232 - Image Processing Toolbox ver. 5.2). This model is labeled the CV3D model. This label indicates that the model includes: 1) a curved macular surface–C, 2) varying OM layer thicknesses–V, and 3) a macular perimeter in three-dimensional space–3D. The CV3D OM model accurately describes the geometry of the turtle utricle. Modifications to this model, used to investigate the effects of different geometric configurations, are discussed later in Section 0: OM Model Variations.

The first step in constructing the CV3D model was fitting a curve to the neuroepithelium of the LM transect. This process was performed by visual inspection on an enlarged image of the LM transect. One data point at the top of the neuroepithelium was collected approximately every 50 microns. This provided curvature of the macula in the lateral-to-medial direction. Then OM layer thicknesses from the LM transect () was added to the curved neuroepithelium.

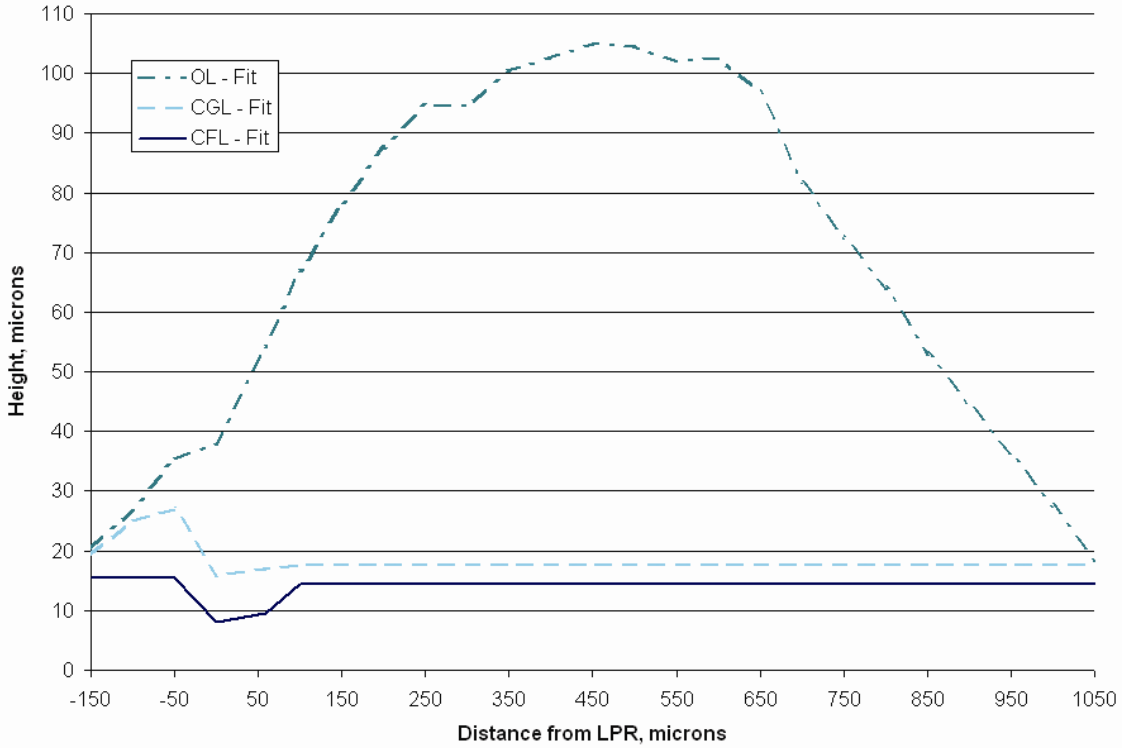

Figure 8: Lateral-Medial Transect Layer Thickness

Plotted in this figure are curve fits of lateral-medial transect layer thickness data from Xue & Peterson 2003. This blue line (solid) represents the column filament layer thickness relative to the epithelial layer. The striolar region is clearly visible here from approximately negative 10 microns to approximately positive 75 microns, and is the thinnest region in the CFL. The cyan line (dashed) represents the thickness of the compact gel layer. And finally the aqua line (dash-dot) represents the thickness of the otoconial layer along the lateral-medial transect. Layer thickness data between 950 and 1050 microns was linearly extrapolated from Xue and Peterson (2003) to accommodate the 12 orthogonal cross sections (see **Figure 7**) that were collected from the right utricle at 100 micron increments. Each discretized layer is used to construct the finite element models. The Quasi-2D model set layer thicknesses are based on this figure.

Next, a curve was fit by visual inspection to the neuroepithelium of each of the 12 orthogonal cross sections, which provides macular curvature in approximately the anterior-to-posterior direction, and to the upper boundary of the OL (). Each visual curve fit contained 120-180 points which were later cubically interpolated to include 29 points for each AP section (in both OL and EL boundary fits). Twenty-nine points were enough to see the features of the OL and EL which we were interested in representing: curvature of the macular surface and varying OM layer thickness. In addition, it was necessary to have the same number of points for each AP (orthogonal) section fit for ease of

constructing the model in ANSYS. Converging the model using ANSYS (See Appendix A) would determine if further discretization was necessary.

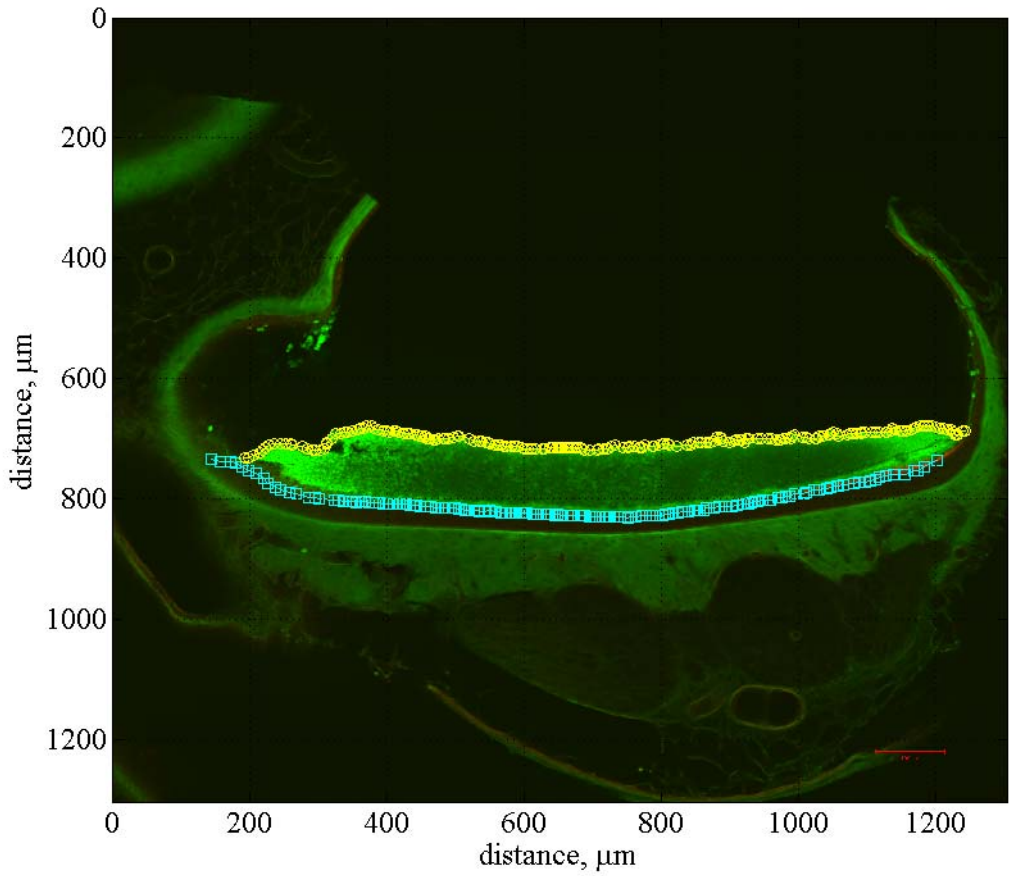

Figure 9: Anterior-Posterior (Orthogonal) Cross section

This figure shows a confocal image of Anterior-Posterior cross section number 6 of the right utricle. All of the Anterior-Posterior cross sections (12 total) were sliced at 100 micron increments. They are numbered sequentially from 1, indicating the lateral end of the utricle to 12, indicating the medial end. Also displayed in this figure is the curve fit used to locate the top of the EL, identified with cyan squares, and the top of the OL, identified with yellow circles.

Finally, a perimeter of the OL as seen in a whole-mount () was approximated by visual inspection and used to define the macular perimeter. Investigations into the sensitivity of OL displacement to slight variations in the macular perimeter were not part of this study. While Tribukait et al. (2001) have looked at the effects of variations of a macular perimeter on the response of the OM, the focus of this study is to investigate

what should be included in models. Macular perimeter will be shown to be an important feature to be included in otoconial organ models.

The confocal sections with their associated curve fits were assembled in a “fishbone” fashion (LM transect as the “back bone” and the orthogonal cross sections as “ribs”). An example of this is shown in .

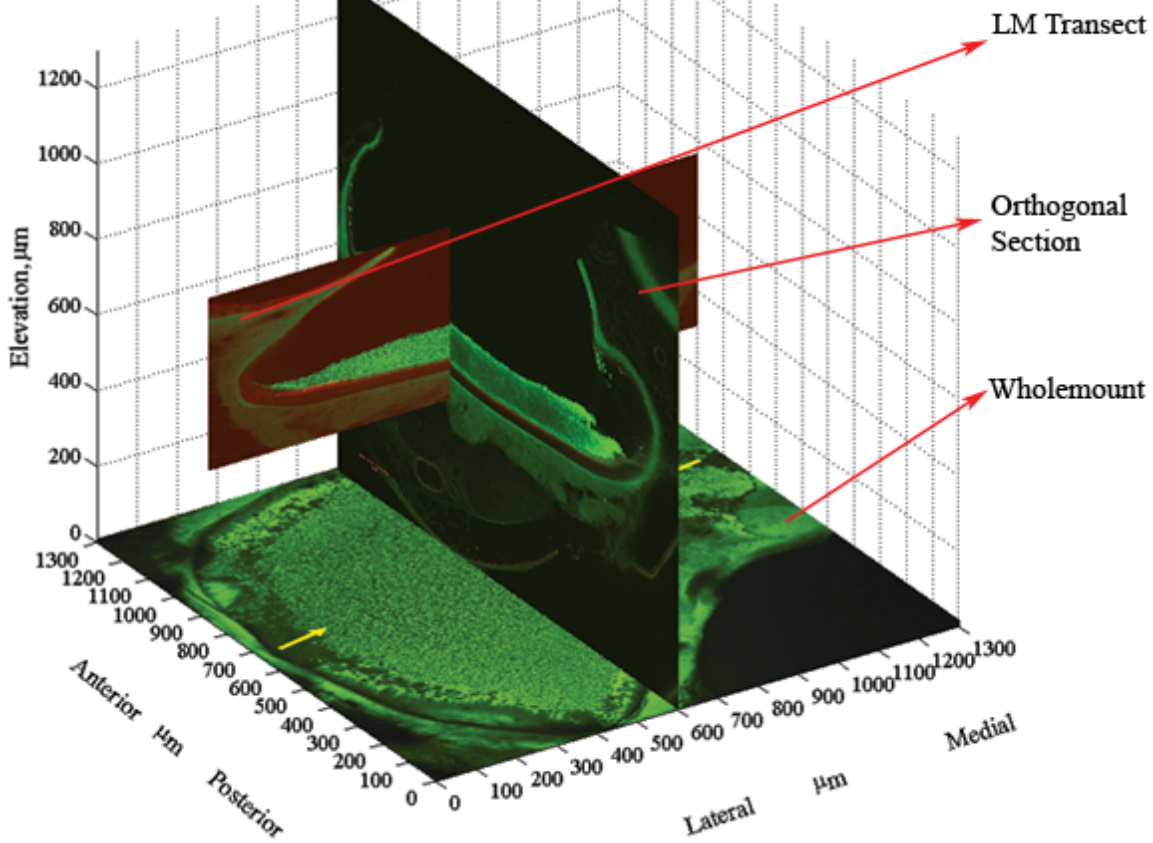

(Wholemount and LM Transect from: Xue & Peterson 2003)

Figure 10: Fishbone Assembly

, **Figure 7**, & are used to illustrate how the utricle model is assembled from the curve fits of each section. This represents the fishbone architecture. The placement of the LM transect (backbone) and one of the 12 AP sections (ribs) is shown. The whole-mount is fixed in its location. It is primarily used to adjust the AP sections anteriorly and posteriorly. Once the AP sections are adjusted within the utricle outline, their elevation is adjusted to match the EL of the LM transect to the EL of the AP section (Note: Elevation origin is arbitrarily defined in this image). This is repeated for all of the 12 AP sections. Linear interpolation between the AP sections is used to create the surfaces representing the neuroepithelium and the superior margin of the OL.

With the whole-mount providing a guideline for placement, the LM transect was placed appropriately on this whole-mount view (yellow arrows in). Each of the 12 orthogonal cross sections were then placed perpendicular to the whole-mount view and adjusted in the horizontal plane until their OL margins were aligned with the macular perimeter. Then the neuroepithelium from each orthogonal cross section was aligned with the neuroepithelium of the LM transect. Linear interpolation is used between the aligned curve fits to create surfaces representing the neuroepithelium and the superior margin of

the OL. Finally, the measured thicknesses of the CFL and CGL along the LM transect was assumed to be representative of layer thicknesses along any other radial transect through the macula. This places the 75 micron wide striolar region along an arc from anterior to posterior following the curve of the lateral edge of the utricle (See).

Previous models usually assume the macular surface to be flat (Grant et al. 1984; Grant and Cotton 1990; Kondrachuk 2000; 2001a; b). However, this is not the case with the turtle: the macular surface is curved. The best fit plane to the macular surface is defined as the macular plane. The planar fit was determined by minimizing the distance between the fit plane and all of the points defining the macular surface. This plane will later be used to reference stimulus applied to the utricle.

2.2.2.2. OM Model Variations

Next, the physiologically accurate (CV3D) OM model (A) was modified to examine the influence of two geometric variables on the response of the OM: 1) curvature of the macular surface and 2) spatial variation in OM layer thicknesses. The neuroepithelium was modeled as a flat surface and/or used average thickness for each of the OM layers across the entire macula (i.e.: no spatial variation in layer thickness). Macular perimeter remained constant in these models. The resulting OM models are named as follows (B–D): Curved macular surface with Constant layer thickness 3 Dimensional (CC3D) OM model, Flat macular surface with Varying layer thickness 3 Dimensional (FV3D) OM model, and Flat macular surface with Constant layer thickness 3 Dimensional (FC3D) OM model.

To compare the results from the 3D OM model set to those typically seen in the literature, the Quasi-2D OM model set (E–H) was created. These OM models are not literally two dimensional, but they are based solely on the geometry of the LM transect. This set differs from the 3D OM model set in that a curved macular perimeter is not included (i.e.: the macular perimeter is rectangular) and there is no variation of curvature in the orthogonal (anterior–posterior) direction. The first of the four models, Curved macular surface with Varying layer thickness Quasi-2 Dimensional (CV2D) OM model, is formed by simply extruding the LM transect in the orthogonal direction (E) until the mass of the OL is the same as the mass in the 3D OM models. The remaining Quasi-2D OM models (CC2D, FV2D, FC2D; F–H) were created in the same manner as the 3D OM

models: removal of curvature of the neuroepithelium and/or spatial variability in the thickness of each layer.

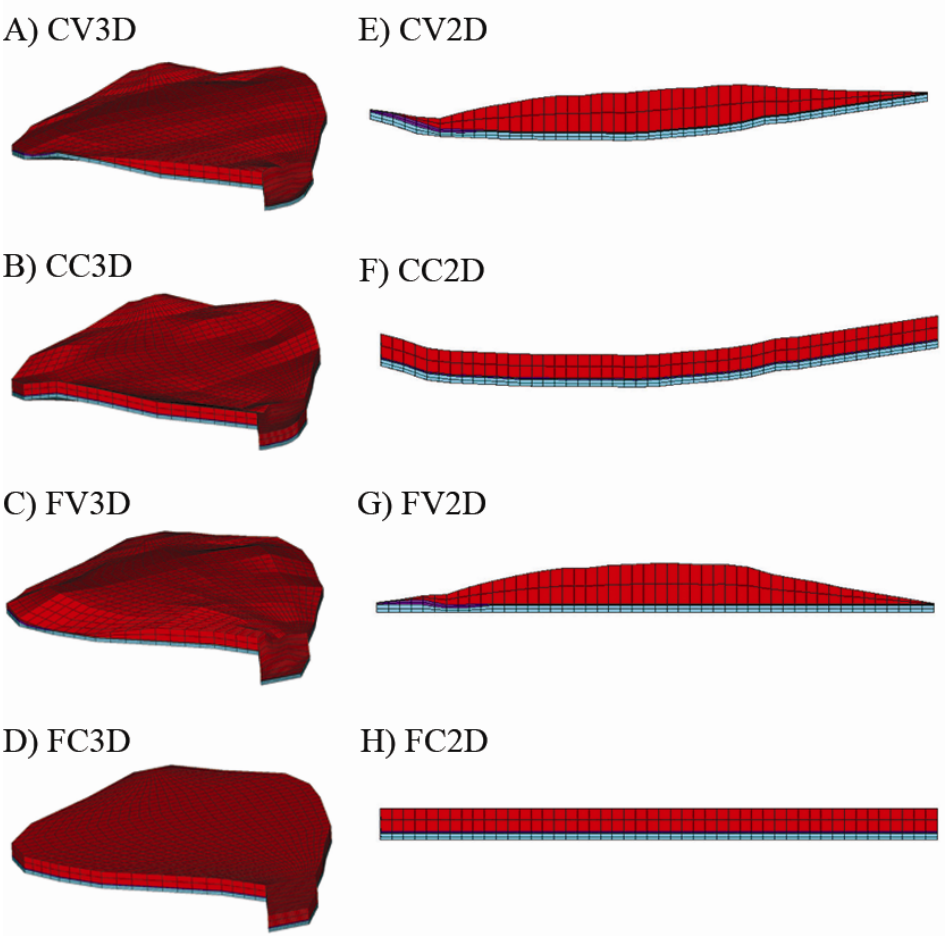

Figure 11: Three Dimensional and Quasi-Two Dimensional Models

In A) the most accurate representation of the turtle utricle is shown: the Curved macular surface with Varying layer thickness 3 Dimensional (CV3D) model. Each of the variations within the 3D set either removes the curvature from the macular surface or averages the layer thickness of each of the layers, while holding the macular perimeter as a constant.

The remaining 3D models are the: B) Curved macular surface with Constant layer thickness 3 Dimensional (CC3D) model; C) Flat macular surface with Varying layer thickness 3 Dimensional (FV3D) model and; the D) Flat macular surface with Constant layer thickness 3 Dimensional (FC3D) model.

In E) the model that is based solely on the LM transect is shown with lateral to the left and medial to the right. This is the first of the Quasi-2D models set. The macular perimeter that was used with the 3D models has now been removed to create the Quasi-2D models. Each of the variations within the Quasi-2D set either removes the curvature from the macular surface or averages the layer thickness of each of the layers.

The remaining 2D models are the: F) Curved macular surface with Constant layer thickness 2 Dimensional (CC2D) model; G) Flat macular surface with Varying layer thickness 2 Dimensional (FV2D) model and; H) Flat macular surface with Constant layer thickness 2 Dimensional (FC2D) model.

E through **H** also represent the lateral-medial transect of their 3D counterparts: **A** through **D**, respectively.

Careful attention was paid to maintain the same total mass of the OL (5.442E-8 kg) between all of the OM models. Depth of the 2D models was not of concern here. The important issue is the equal OL mass as it provides inertia which allows accelerations to shear the CFL and GL. Thus the effects on displacements of varying OM layer thickness are due to changes in OL mass distribution, not the total mass of the OL. If the OL mass was not held constant between models, deflections with the same static stimulus would yield results that may not be entirely due to the variables studied here. The same is true for the mode frequencies.

In addition, juxtaposing the Quasi-2D and 3D OM model sets demonstrates how the curved macular perimeter effects displacement of the OM. Within the Quasi-2D or 3D OM model sets the effects of adding either macular curvature or varying OM layer thickness are isolated.

2.2.2.3. OM Material Properties

The GL and CFL have been described as having a "jelly-like" consistency (De Vries 1951) and are viscoelastic (Grant and Cotton 1990). These layers are saccharide gels and have the potential to behave nonlinearly, in addition to having anisotropic and viscoelastic material properties. The CFL, for example, consists of a network of interconnected filaments which has been described as visually anisotropic (Kachar et al. 1990). However, due to lack of available material property information on these layers, they have previously been modeled as linear elastic (Jaeger et al. 2002; Kondrachuk 2000) and linear viscoelastic (Grant and Cotton 1990; Grant et al. 1994).

Because the material deformation properties of the OM layers in the turtle utricle are not known, results from Kondrachuk's modeling efforts, shown in Table 1 (Kondrachuk 2000; 2001a) were used. These are the only results, that isolate the material properties of the CFL-HB complex (the layer consisting of both the CFL and HBs) and GL utilizing animal experimental tests (Benser et al. 1993; Kondrachuk 2000). Modeling Benser et al.'s experiment on the bullfrog saccule, Kondrachuk arrived at material properties for the GL (6600 Pa – See Table 1) and the CFL–HB complex (250 Pa – See Table 1).

Table 1: Material Properties
This table summarizes the material properties & constants used in each of the FE models.

Variable	CFL-HB	CGL	OL (turtle utricle only)
Modulus, *E* (Pa)	250	6600	6.6e6
Density, ρ (kg/m^3)	1000	1000	2400
Poisson's ratio, ν	0.45	0.45	0.45

Material deformation properties for the OL are difficult to estimate due to variability in the crystal-gel ratio and mineral composition of crystals across species (Pote et al. 1993). The OL has been assumed to be much stiffer than the gel layer due to the combination of otoconial crystals and gel. It has been suggested that an increase of stiffness between 20 times (Jaeger et al. 2002) and 3 orders of magnitude (Kondrachuk and Ross 1997) over the GL is sufficient to describe the OL modulus. However, because the otoconial layer is thought to behave as if it were approximately rigid (Jaeger et al. 2002), any modulus that produces rigid body movement of the OL will suffice. A modulus of 6.6 MPa was used here, which is 3 orders of magnitude higher than the modulus of the GL.

Lateral anchoring attachments between the periphery of the OL and the otoconial membrane, whose postulated purpose is to hold the OL in place, have been seen in some species (Money and Correia 1972). These attachments are not explicitly included in these models, although they would add additional stiffness and reduce deflections. These effects were assumed to be incorporated into the moduli of the CFL and GL as measured by Benser et al. (1993) and Kondrachuk (2000).

The densities and Poisson's ratios for the CFL and GL used in this study are shown in Table 1. These layers are treated as incompressible with a density of water (Grant and Best 1986; Grant and Best 1987; Jaeger and Haslwanter 2004; Jaeger et al. 2002; Kondrachuk 2000). Poisson's ratio equal to 0.45, 0.49 and 0.499 were tested with no change in the results. Therefore, for all intents and purposes, Poisson's ratio of 0.45 can be considered incompressible here. The OL density, however, is based on the 3:1 ratio of calcite (2710 kg/m^3) and aragonite (2930 kg/m^3) (Carlstrom 1963) and the

approximately 4:1 ratio of crystal to gel (Pote et al. 1993) seen in turtles. The resulting OL density is 2400 kg/m^3.

2.2.2.4. Mesh and Boundary Conditions

ANSYS™ 11.0 was used for meshing and solving each of the OM model displacements, mode shapes and natural frequencies. Each of the OM models was meshed with 8 node brick elements having 3 degrees of freedom per node, yielding mass and stiffness matrices describing the discretized properties of the utricle. The 3 degrees of freedom account for deflections in each Cartesian direction. Because the utricle primarily deforms in shear the only concern in these models is deflection. Each of the finite element models was converged to less that 1 percent error for both static and modal solutions (see Appendix A - Model Convergence).

2.2.2.5. Static and Modal Tests

Each of the eight OM models was tested under the same boundary conditions. For static testing: the neuroepithelium was fixed and a body force of 1g (i.e.: weight) acting in the macular plane was applied to the OL. Because of buoyancy effects from surrounding endolymph fluid, the body load acts only on the much denser OL, reducing its effective density by that of the endolymph fluid, 1000 kg/m^3 (Grant et al. 1994; Grant and Best 1987). Displacements of the OM were obtained by solving :

$$[K]\{x\} = [M]\{g\}$$

Equation 2: Static Analyis Matrix Equations

where $[K]$ is the stiffness matrix, $[M]$ is the mass matrix, $\{x\}$ is the resulting displacement vector, of the discretized OM, and $\{g\}$ is the applied gravitational vector. Recall (as discussed in section 0), that for each of the OM models, careful attention was paid to keeping the total mass of the OL constant between the models. This is important as the deflections of the OM, obtained from , are dependent not only on the total mass, but also the distribution of mass within the structure.

The gravitational vector was rotated in the macular plane at 15 degree increments. Displacement at the CFL-GL interface below the center of mass (COM) of the OL measured for each application of the g vector. This displacement is divided by the applied load, and is referred to as the static mechanical gain. It should be noted that the location of the COM is not necessarily the same between the models. However, the displacement

below the COM of the OL is a good way to represent the global motion of the OL as it pertains to hair bundles. Results from each model illustrate how the stimulus to hair bundles is affected by macular curvature and spatial variation in OM layer thickness. Although the CFL-GL interface is not exactly where all hair bundles contact the OM (Kachar et al. 1990; Ross et al. 1987), understanding the movement of this interface is an important step into characterizing the overall motion of the organ. This will then lead to an understanding of how hair bundles may respond to the motion of the OL.

The effects of macular curvature, OM layer thickness, and macular perimeter on the modal response of the utricle is also investigated. Results from modal analysis are the undamped natural frequencies and displacement modes of vibration of a mechanical system. In the case of the utricle model, undamped natural frequencies of displacements within the OM are proportional to eigenvalues (λ), and the eigenvectors ($\{\Psi\}$) represent the magnitude and direction of these displacements (i.e., displacement modes of vibration; see below) when the neuroepithelium is fixed. Eigenvalues and eigenvectors are solved for using , where: $[M]^{-1}$ is the Inverted Mass matrix (from), $[I]$ is an identity matrix. Setting the determinant of equal to zero one may solve for all of the eigenvalues.

$$\left[[M]^{-1}[K] - \lambda[I]\right]\{\Psi\} = \{0\}$$

Equation 3: Modal Analysis System of Equations

Eigenvectors are determined by directly solving for each λ.

Each FE model used in this analysis was meshed with over 13 thousand nodes having three degrees of freedom per node, i.e., three possible directions of displacement per node. In addition, each model has as many natural frequencies (eigenvalues) and characteristic displacement modes of vibration (eigenvectors) as degrees of freedom in the model (Reddy 1984). Each displacement mode represents a linearly independent combination of displacements at nodes in the model. The phase relationship of nodal movement can be represented by modes, which describe the relative magnitude and direction of each nodal displacement with respect to other nodal displacements in the model (Meirovitch 1986). For example, if the whole structure moves in-phase, as in a low frequency mode, all of the nodes would be moving in approximately the same direction at the same time.

Low frequency displacement modes represent the largest whole-body-in-phase displacements of a structure. This is because the amplitude of displacement is inversely proportional to the square of the frequency. High frequency displacement modes represent motion in which parts of the structure move out-of-phase with other parts of the structure (Meirovitch 1986). Low frequency displacement modes are of interest here for two reasons. First, low frequency displacement modes are easily excited (they require less energy to excite) and are therefore most frequently excited. Secondly, in these OM models these low frequency displacement modes represent shear displacement of the OL. This is the characteristic motion of the OL that excites hair bundles. Higher order displacement modes represent more complicated, non-characteristic motions of the OL. For example, the third displacement mode of the CV3D model represents torsional rotation of the OL over the macular surface about a point near the center of the OM. This displacement mode, as well as other remaining higher frequency displacement modes, is probably not excited under normal physical conditions due to: 1) displacements in high frequency modes generally being of small out-of-phase amplitude would be ineffective in exciting hair bundles or groups of hair bundles with similar orientation and 2) damping in the structure would further attenuate the displacement magnitude.

2.3 Results

2.3.1. Static Results

Static mechanical gain (magnitude of displacement of the CFL-GL interface below the mass center of the OL/ Gravitational vector) is used to illustrate the static results because it 1) captures the global behavior of the OM at 2) a region in which most hair bundles interact with the OM. Asymmetry of the 3D macular perimeter and thickness variation of the OM models (e.g.: CV3D OM model) contribute to a maximum variability of 15 nanometers of displacement magnitude between macular locations at the CFL-GL interface. This variability is avoided by using mass center measures but is later explained with the displacement mode shapes. Therefore, static mechanical gain is a good representation of displacement in the OM at a height pertinent to hair bundle stimulus.

Static mechanical gain is observed to change with stimulus direction (). Static mechanical gain of each 3D OM model, when plotted in the macular plane, outlines a

peanut shape, having orthogonal maximum and minimum gains. These plots are similar to the maximum response figures shown by Jaegar et al. (2004).

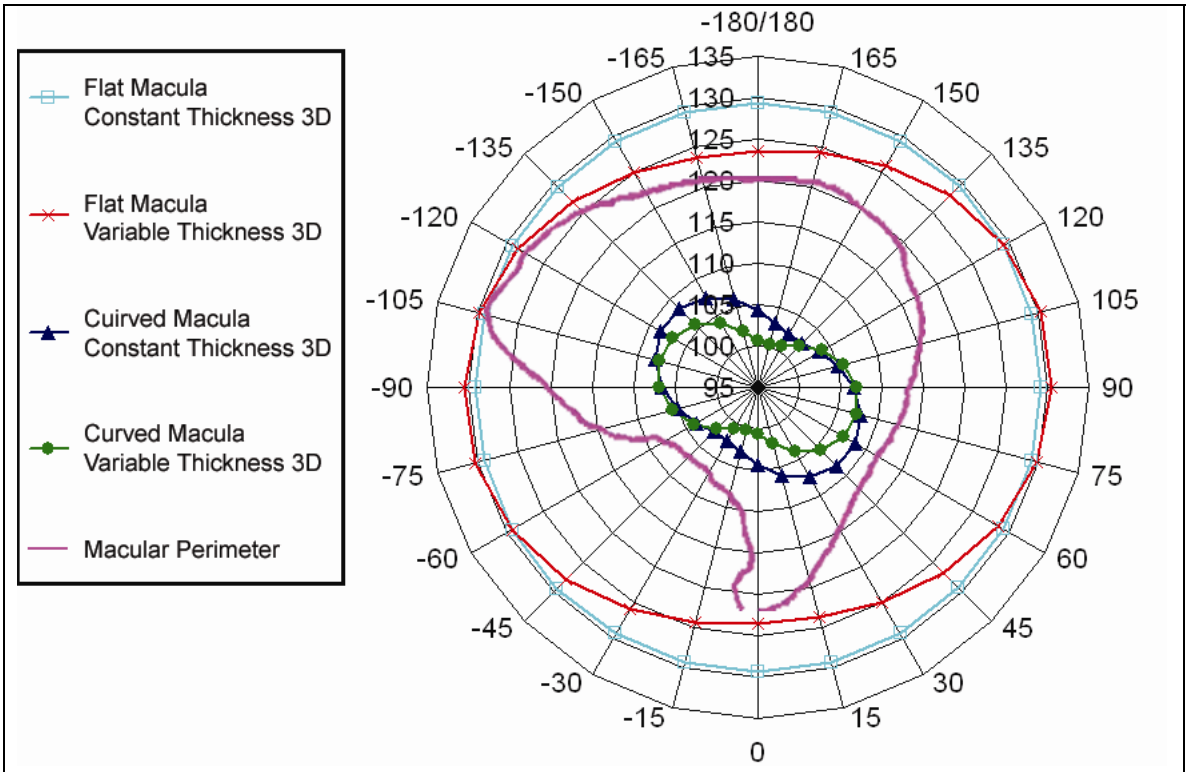

Figure 12: Static Mechanical Gain (in nm/g) for all 3D models

This image shows a polar plot of the static mechanical gain for the four three dimensional models. The scale is from 95 nm/g at the center, to 135 nm/g. This scale is chosen to visually enhance the variation in the gain. The variation in the flat models are similar to the curved models in that they do have a "peanut shape" although the variation between maximum and minimum gain is slight. The macular perimeter is shown as a reference for orientation. From this plot it curvature of the macular surface is shown to contribute to decreasing the static gain in all directions. In addition, variable thickness also is shown to contribute to the changing gain by rotating maximum and minimum directions.

In order to determine if minor errors in the curve fitting or tissue preparation of the OM may affect results of the static mechanical gain, the density of the OL in different regions of the utricle was increased. These tests indicate that static mechanical gain increases due to an increase in the overall mass of the OL, but the orientation and shape of the static mechanical gain remains unaffected.

Static mechanical gain results indicate that magnitude and orientation vary with 3D OM geometry. For example, the OM model with flat macular surface and spatially

varying OM layers (FV3D; , red crosses) has the greatest maximum gain of all the OM models (see Table 2). The OM model with flat macular surface and constant OM layer thickness (FC3D; , blue squares) has a slightly lower maximum gain (reduced by about 1 nm/g) but this OM model's direction of maximum gain has rotated at least 60 degrees in the macular plane from the FV3D OM model. The change in orientation of the OM maximum static mechanical gain is due to spatial variation of the thickness of the OM layer thickness.

Macular curvature reduces the magnitude of maximum static mechanical gain by 17-18 percent. This is shown in as a reduction in the maximum magnitude of the gain peanuts from about 130 nm/g to about 108 nm/g. Recall that this is the displacement per unit g at the height at which most hair bundles interact with the OM, and therefore a 22 nm/g average reduction may effect a hair bundle's activation. With the addition of macular curvature to the OM models, the effect of spatially varying OM layers is reduced, only changing the orientation of the maximum static mechanical gain about 15 degrees between (CC3D and CV3D) OM models. This could be slightly less or slightly more considering our interval for testing was 15 degrees.

Table 2: Static mechanical gain results

This table includes the maximum static mechanical gains for all of the models. In addition for the 3D models, this table includes the corresponding angle of excitation for which the maximum deflection occurs. This is not included in the Quasi-2D models because the only deflection of interest in these models is along the LM transect.

		Quasi 2D Models	3D Models	
Macular Surface	**OM Layer Thickness**	**Max. Static Mechanical Gain (nm/g) [LM Transect]**	**Max. Static Mechanical Gain (nm/g)**	**Corresponding Angles (degrees)**
Flat	Constant	131.02	129.31	15 & -165
Flat	Variable	132.94	130.53	90 & -90
Curved	Constant	122.77	108.55	75 & -105
Curved	Variable	124.52	107.39	60 & -120

The effect of macular perimeter on the direction of maximum static mechanical gain is evident in the 3D OM models. These results indicate macular perimeter should be included in future OM models because macular perimeter can effect the response of the OM. Tribukat et al.(2001) showed that changes in the shape of the macular perimeter

may also effect the gains in different regions of human utricle, and in the future, these subtle changes could also be considered in structural models. The Quasi-2D models were not considered here because the only static mechanical gain that is relevant to the model is the gain along the direction of the LM transect. Since the perimeter of these models is rectangular (i.e.: symmetric), there is only a change in the magnitude of the peanut, not its direction.

2.3.2. Modal Analysis Results

In addition to static mechanical gain, the undamped natural frequencies and displacement modes (of vibration) of the OM response were calculated to learn how our three geometric variables may effect OM response dynamics. Recall that total mass is kept constant across all models, thereby eliminating total mass as an independent variable.

Undamped natural frequencies corresponding to the lowest (i.e.: first) mode of vibration for all the OM models are reported in Table 3. In the case of the Quasi-2D OM models, these frequencies correspond to displacement modes in which the rigid displacement of the OL shears underlying CFL and GL along the LM transect. This is the only meaningful direction of displacement for these models, since they do not account for either macular perimeter or spatial geometry in the orthogonal directions.

Table 3: Modal Analysis Results – Shearing Mode Frequencies

Presented in this table are the natural frequencies of the shearing mode along the LM transect for the Quasi-2D,and the first shearing natural frequency for the 3D models each of the models discussed. The effects of curvature are seen in the increase in the natural frequency and are interpreted as an increase in model stiffness. A decrease in the natural frequency when comparing the constant thickness models to the variable thickness models speaks to the effect of distributed mass on the natural frequency of the system.

		Quasi 2D	3D
Macular Surface	**OM Layer Thickness**	**ω_n, Hz**	**ω_n, Hz**
Flat	Constant	1389.76	1396.06
Curved	Constant	1436.09	1515.06
Flat	Variable	1377.90	1376.84
Curved	Variable	1426.88	1530.19

The displacement modes shown in **Figure 13A–D** correspond to the natural frequencies of the 3D OM models listed in Table 3. These displacement modes also indicate a rigid displacement of the OL, thereby shearing the underlying layers of the OM. However, unlike the 2D OM models, the rigid displacement of the OL has a slight rotation in all of 3D OM models. The point about which the OL rigidly rotates in each mode is referred to as the center of rotation for that mode. This point is determined by calculating the location of the intersection of two lines perpendicular to the direction of displacement of two nodes in the OL for each mode, ignoring any out-of-plane motion. Its location for each mode is indicated in **Figure 13A–D** by a circled X. The color bar indicates the relative magnitude of deflection within each mode (red = largest magnitude and blue = lowest magnitude).

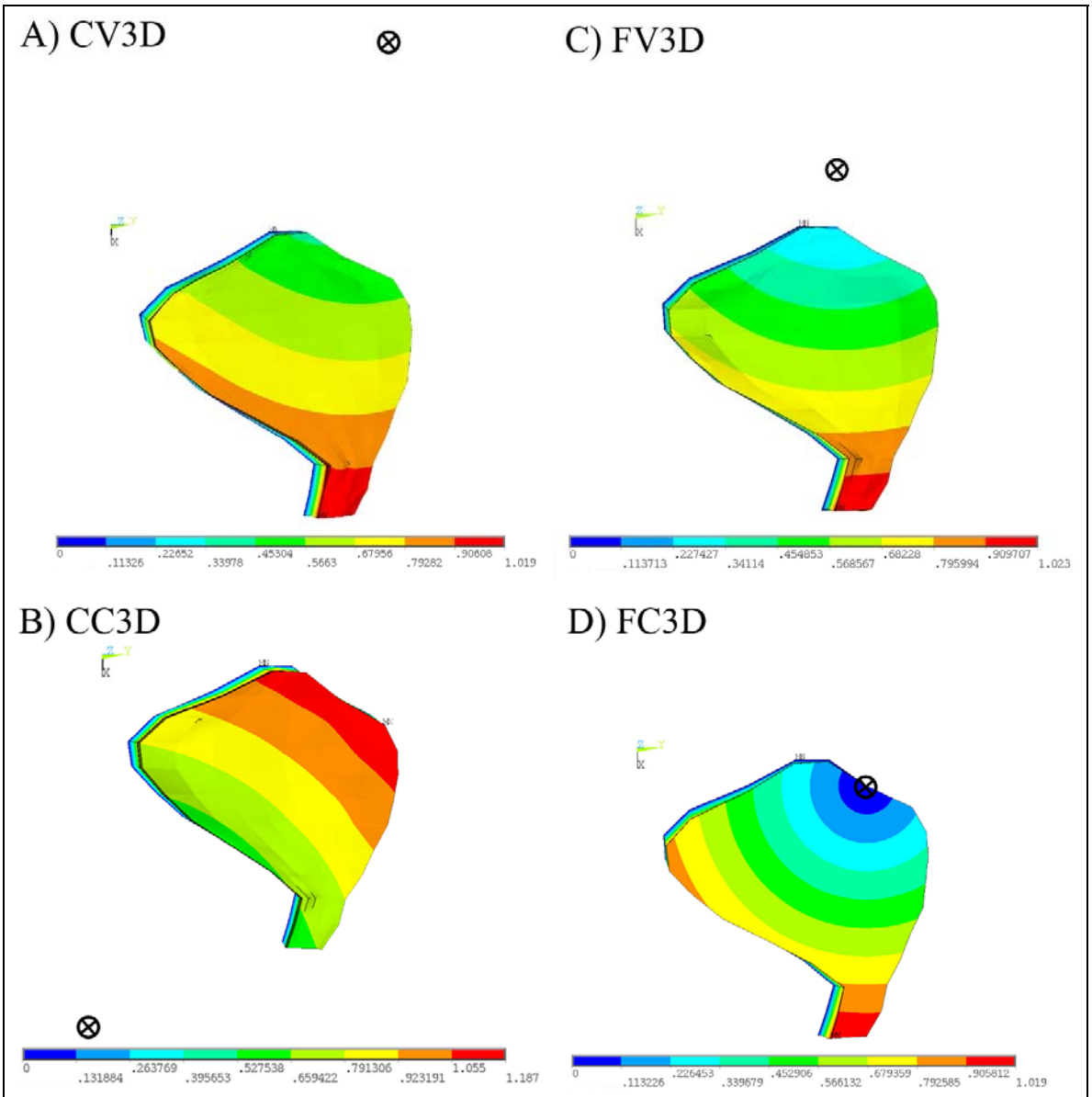

Figure 13: Mode Shapes and centers of rotations corresponding to first natural frequency of 3D OM models

This figure indicates the displacement magnitude (red = large & blue = small) and the center of rotation (circled X) for each of the mode shapes corresponding to the 1st natural frequency for each of the 3D OM models. The deflection in the first mode causes a shearing of the CFL. This shearing, however, is no longer restricted to be parallel (or perpendicular) to the LM transect, as is the case in the 2D OM models. The center of rotation is located by calculating the intersection of two lines drawn in the macular plane & perpendicular to the directions of defelction of two points in the OL.

Additionally, the direction of deflection of the center of mass in the first two undamped displacement mode shapes of the utricle OM is discovered to align with the maximum and minimum static mechanical gains. Spatial variation of OM layers does not affect the magnitude of the natural frequency significantly, just as it does not affect the magnitude of the maximum gain in the static analysis. However, redistributing the OL mass over the macular surface does shift the center of rotation of the OL in the macular plane. For example, the first displacement mode of the FC3D OM model indicates a maximum displacement of the OM (shown in red) at the medial extreme of this OM model. The minimum displacement of the OM (shown in blue) is located at the anterior-lateral portion of this OM model. This minimum displacement also coincides with the center of rotation of the OL for this displacement mode. While this displacement mode is similar to the first displacement mode of the flat macular surface and spatially varying OM layer model (FV3D OM model), in that the maximum and minimum displacements occur in similar regions of the OM, the difference between these displacement modes is the location of the center of rotation.

The center of rotation for the first displacement mode of the FV3D OM model is not located on the anterior-lateral portion of the utricle. It is located at a point lateral to the utricle. Additionally, the center of rotation for all the models except the CC3D model is towards the lateral side of the utricle. This is probably due to both the curvature of maculae and more OL mass in the lateral region of the CC3D model. These shifts in the centers of rotations are analogous to changing the directions of the maximum static mechanical gain. In fact, close alignment between the direction of deflection of the center of mass in displacement mode 1 of each OM model is observed when the center of rotation is not located within (or on) the macular perimeter (i.e.: all except the FC3D OM model). This slight rotation in the lowest frequency (i.e.: the frequency closest to zero or static) displacement mode shape is indicative of the influence of the first displacement mode shape on the static displacement and thus explains the slight (15 nm) variation in displacements over the macular surface observed in the static test. A 15 nm variation in displacement is probably insignificant to the activation of MES hair bundles, due to their large operating range (Baird 1994; Nam et al. 2005a). However, there is a steep rate of

change in activation in striolar hair bundles at the low end of their operating range (Nam et al. 2005a). Therefore, a striolar hair bundle may be able to detect this small variation.

Curvature of the macular surface, in addition to changing the location of the center of rotation of the displacement modes, also increases the natural frequency of the OM models. This indicates an increase in stiffness, as the square of the natural frequency is directly proportional to stiffness (see). Thus, comparing the stiffness (i.e.: the square of the natural frequency) between models with and without curvature, indicates an increase in stiffness of between 17 and 23 percent when curvature of the macular surface is included. This change in magnitude of stiffness is close to those calculated using static mechanical gain in the static analysis, in which stiffness is directly proportional to displacement.

Finally, not including macular perimeter in the OM models geometrically restricts the displacement in the mode shapes. The only geometric variation in the Quasi-2D OM models is along the LM transect, therefore, the only meaningful displacement modes are parallel to this direction (see Table 3: Quasi-2D). Once asymmetry of the macular surface is introduced, with the inclusion of a curved macular perimeter, the meaningful mode shapes of the utricle are no longer restricted to just the lateral-medial directions (See **Figure 13 A-D**). In fact, the first mode of vibration, the easiest mode to excite, of the geometrically accurate OM model (CV3D) is observed to have an anterior-posterior component of deflection. These displacement modes are not apparent in OM models without macular perimeter.

2.3.3. Hair Bundle Displacement

It is important to keep in mind that hair bundles are the mechano-electric transducers of OM stimulus. Contained in the CFL, displacements are transduced to the hair bundles through the displacement of the OM. While geometry of individual hair bundles may effect their own displacement, location on the macular surface may also effect hair bundle displacement. This is potentially due to varying OM structure over different regions of the curved macular surface. Therefore, how static displacements along the LM transect of the CV3D utricle model under a static 1 g load (parallel to the LM transect) differ from one another is investigated. Displacements in three representative regions are measured: medial extrastriola, striola (STR), and lateral

extrastriola. The results are shown in **Figure 14**, in which each curve represents the displacement throughout the CFL and GL (relative to the neuroepithelium) for each representative region. The point of inflection in each curve indicates the transition between CFL-HB and GL. These results indicate a bundle contacting the OM in the striolar region may experience twice as much angular deflection, due to the thinner CFL, than bundles contacting the OM in the extrastriolar (MES or LES) regions.

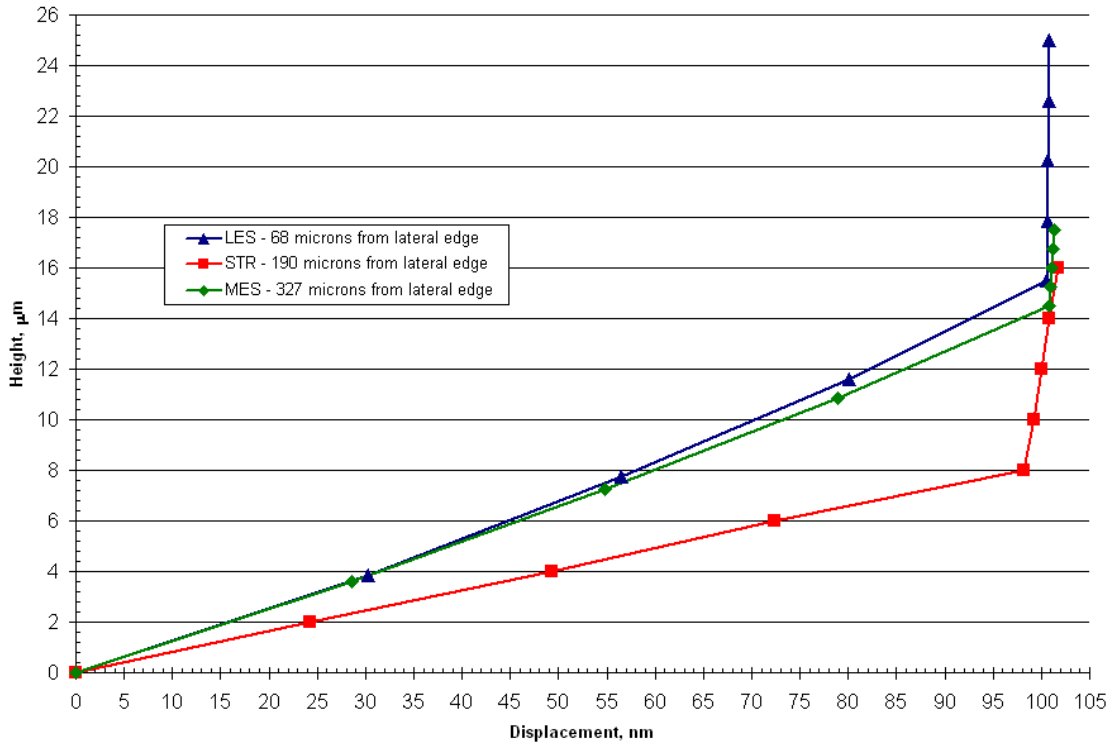

Figure 14: Displacement Profile for 3 regions along the LM transect of CV3D OM (Utricle) Model

This figure shows displacements through the GL and CFL-HB complex for 3 regions along the LM transect in the CV3D model. Triangles represent the Lateral Extrastriola region (located 68 microns from the lateral edge), squares represent the striolar region (located 190 microns from the lateral edge) and diamonds represent the Medial Extrastriola region (located 327 microns from the lateral edge). The point of inflection in each curve indicates the transition between CFL-HB and GL. Most of the shearing occurs in the more compliant column filament layer of the model. These displacement profiles are linear in a given region and reflect the general behavior throughout their region.

In addition, there are locations in LES of the CV3D OM model in which the displacement profile through the CFL-HB complex does not follow the same linear

profile as in other regions of the utricle. These regions (along the LM transect) and approximate distance from the lateral edge of the utricle are shown in **Figure 15**. Possible reasons for these results are discussed in the following section.

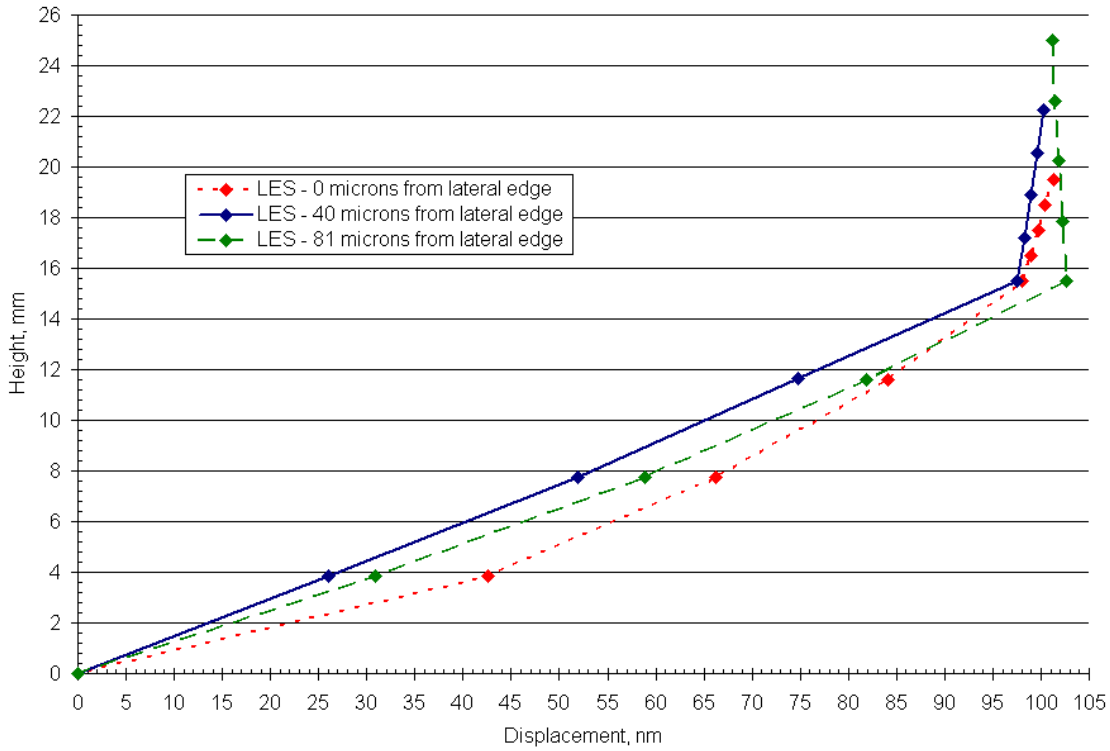

Figure 15: Displacement Profile for 3 locations in the Lateral Extrastriola (LES) along the LM transect of the CV3D OM (Utricle) model

This figure illustrates the displacement profile of the GL and CFL-HB complex for 3 discrete locations (0,40, and 81 microns from the lateral edge) in the LES. The point of inflection in each curve indicates the transition between CFL-HB and GL. In the LES, displacement profiles arise in the CFL-HB complex that depart from the linear profile observed throughout the interior region. These displacement profiles indicate that proximity to the lateral edge is not the only mechanism to disrupt the linear deformation profiles in this region. Additional suspected causes for this disruption are the thinning OL in this region and an increased curvature of the macular surface.

2.4 Discussion

2.4.1. Possible Function of Geometric Variables

The results of this investigation indicate structure of the utricle can influence OM and presumably hair bundle deflections. The effect of each geometric variable (macular perimeter, macular curvature and spatially varying OM layers) on the static and modal

response of the OM was tested. Static mechanical gain and modal analysis reveal similar information as to the effect of each variable. Including macular perimeter in OM models introduces asymmetry in the macular plane of the models. The most obvious effect is seen in the redistribution of OL mass in the macular plane. This contributes to both amplitude and direction changes in the static and dynamic OM displacements. Curvature of the macular surface acts to stiffen the utricle. This is observed first in the magnitude of static mechanical gain. Curved macular surface models have lower static mechanical gains when compared to the models with flat macular surface. The increase in stiffness may also be seen in the larger OM natural frequencies than the natural frequencies of the flat macular surface OM models. And while macular curvature and macular perimeter may both contribute to the direction of the maximum gain and the center of rotation for the displacement modes, it is the spatial variation of the OM layers that may act as a tuning mechanism. Variation of the OM layer thicknesses provide minor adjustments to the direction (and magnitude) of maximum static mechanical gain. In addition, in the modal results, the centers of rotation of the displacement modes are adjusted through a redistribution of OL mass. Therefore, changes in structure of the OM may change our interpretation of the otoconial organ and/or hair bundle's function within the otolithic system.

2.4.2. Loss of Linearity in CFL-HB complex and CGL Displacement Profiles

Observed locally in the CFL-HB complex of the LES region of the utricle are departures from linear displacement profiles (**Figure 15**) not observed in other regions of the utricle (**Figure 14**). One possible reason for this observation is the lack of knowledge as to the effects of the lateral anchoring attachments observed in this region (Money and Correia 1972). These changes in displacement may also be influenced by two geometric changes in this region: 1) a thinning OL and 2) a concave inflection in curvature of the macular surface. Because there is little OL mass to inertially shear the LES of the CV3D OM model (see), the displacement profile of the CFL-HB complex, in this region, is potentially a result of MES and striola regions forcing the displacement in the CFL-HB complex of this region. This change in curvature (which be seen in **E**, representing the geometry of the true utricle's LM transect) combined with a thinning OL, may also effect

the overall stiffness and therefore displacement in the CFL-HB complex and GL of this region of the utricle.

2.4.3. Additional Influencing Variables

The three variables chosen to test (curvature of the macular surface, varying OM layer thicknesses and macular perimeter,) are not the only variables that will contribute to changing deflection in the OM. Structure of each individual OM layer may also influence OM deflections. For example, the column filament layer consists of densely-packed-inter-connected filaments (Kachar et al. 1990), for which the overall material properties of this layer is assumed to be isotropic (Grant and Best 1987; Jaeger and Haslwanter 2004; Jaeger et al. 2002; Kondrachuk 2001a). There has been only one experimental measure of the elasticity of the CFL by Benser et al. (1993), and one finite element model of these experiments, by Kondrachuk (2000). In each of these cases isotropy of the CFL was assumed. However, yet to be determined, is the influence of the interconnectivity and number of filaments on the material properties of this layer. The CFL could indeed be anisotropic, which may influence the displacement of these organs and therefore the force boundary conditions on hair bundles.

A similar example of a variable that could influence displacement of the OM is the channels or holes that have been reported in the GL in the striola region of the turtle utricle (Xue and Peterson 2002). Hair bundles already sit in channels in the CFL. However, in the striola, these channels extend through the GL to the OL. This may decrease the stiffness of the GL in this region resulting in a decrease in the magnitude of displacement transmitted to hair bundles in the CFL. If rigid displacement of the OL is assumed, a weaker GL in this region would displace more when compared to GL deflection in other regions of the utricle. Thus, for the same overall OL displacement, the CFL in the striolar region may deform less due to the weaker GL above absorbing some of the displacement. Recall, from **Figure 14**, that there is another mechanism that may affect stimulus applied to hair bundles: the thickness of the CFL. Hair bundles in the striola already experience twice the shear gradient through the thickness of the CFL than hair bundles in the Extrastriola. This is due to the thinner CFL in the striola. Therefore a proposed purpose for GL holes in the striola may be a mechanism to protect hair bundles

from damaging stimulus by reducing the magnitude of the stimulus transmitted striolar hair bundles.

2.4.4. Limitations of this study

There are some limitations of the model, however, these results are based on the best information currently available on OMs. The first limitation has to do with the material properties of each layer of the utricle. The only available material properties for these types of organs were used. These material properties correspond to a different species (bullfrog) and a different organ (saccule). In addition, the modulus was assumed to be linear, which is still yet to be proven. It has been observed in other organs of the inner ear (eg: tectorial membrane - (Freeman et al. 2003)) that these organs could have anisotropic properties.

Secondly, the thickness of the CFL-HB complex and CGL was assumed to be the same along any transect in the utricle as the thickness observed in the LM transect. This assumption was based on hair bundles having similar morphology and regional variation along different transects in the utricle (Xue and Peterson 2006). The OM, by which hair bundles are stimulated, was assumed to follow the same patterns.

Finally, a more detailed model would consider the hair bundles as separate components of the utricle OM structure instead of lumping their effects together with the modulus of the CFL. While more difficult to model, this may provide more insight into how hair bundles are excited and their interactions with the surrounding OM.

CHAPTER 3. Shear stiffness contribution of hair bundles in the red ear slider turtle to the stiffness of the CFL-HB complex

ABSTRACT

Two finite element models of turtle utricle otoconial membranes are constructed to determine the stiffness contribution of hair bundles to the column filament layer and hair bundle (CFL-HB) complex: the shear layer containing both column filament and hair bundles. The first model implicitly accounts for hair bundles, combining the stiffness of hair bundles and column filament layer into an isotropic shear layer modeled with (linear elastic) volume elements. The second model removes the volume elements of the CFL-HB complex and replaces this shear layer with finite element Euler-Bernoulli beams, explicit representations of hair bundles, whose stiffness matches experimentally measured stiffness values (Grant et al. 2007). The stiffness of the CFL-HB complex in each OM model is compared using undamped natural frequency (a result from finite element modal analysis), which is proportional to the square root of the ratio of stiffness to mass. Since the driving mass of the system (otoconial layer) remains unchanged between models, the resulting change in natural frequency is due to a change in stiffness of the underlying shear layer. This method for isolating stiffness is first confirmed against previous results from experiments (Benser et al. 1993), and models of (Kondrachuk 2000), a bullfrog saccule. These methods are then applied to the turtle utricle. Results indicate hair bundles in the turtle utricle contribute only 3-4 percent to the total stiffness of the CFL-HB complex, where as the calculated contribution of hair bundles in the bullfrog saccule is between 48 and 70 percent: the same as reported in previous works (Benser et al. 1993; Kondrachuk 2000).

3.1 Introduction

Otoconial organs of vertebrates are transducers of linear movement and head tilt (Lowenstein and Roberts 1949). The organ consists of hair cell (HC) bodies located in the neuroepithelium (NE). From the apical surface of these cell bodies hair bundles (HB) protrude into the surrounding otoconial membrane (OM). The OM, which sits atop the neuroepithelium, is made up of three layers (see): an otoconial layer (OL), a compact gel layer (CGL) and a column filament layer and hair bundle complex (CFL-HB). Acceleration acts on the higher density otoconia crystals located in the OL, thus shearing the remaining layers of the OM. This shear displacement is transduced to the hair bundles, located in cylindrical holes or pockets in the CFL-HB complex. Hair cells then translate bundle displacement into receptor potentials that modulate neural signals to the central nervous system.

Hair bundles are active participants in OM displacement; however, it is still not very well known as to how much hair bundles contribute to mechanical resistance of shear displacement of a utricle OM. In 1993, Benser et al. tested eleven bullfrog saccules after removing the otoconial layer in an effort to estimate hair bundle stiffness contribution to CFL-HB stiffness. A flexible glass probe was used to apply a measured force to the remaining membrane layers and a glass sphere on the surface of the remaining membrane layers was used to track the resulting displacement. Using Hooke's law and estimated displacement fields, the stiffness contribution of a single hair bundle to the CFL-HB complex was estimated. **Equation 4** was used to approximate stiffness of the OM. The whisker's applied force, $\vec{F}$, measured and the displacement field, $\vec{D}(x, y)$, is measured at one location and assumed to follow an exponentially decaying (away from the insertion point of the forcing whisker) elliptical or diamond shaped contour. Thus, knowing the density of the gel, ρ, displacement may be integrated over the spatial domain, x and y (minimum 480 x 430 μm^2 (Benser et al. 1993)), in order to approximate stiffness.

$$k_e = \frac{\vec{F}}{\rho \iint \vec{D}(x, y) dxdy}$$

Equation 4: Elemental stiffness from (Benser et al. 1993)

The results of this experiment indicate hair bundles in the CFL-HB complex of the bullfrog saccule dominate, accounting for over 40% of, the stiffness of this OM layer.

Kondrachuk later modeled the Benser et al. (1993) experiment with a finite element model to determine a modulus for the CFL-HB complex and the compact gel layer (CGL) of a bullfrog saccule (Kondrachuk 2000). Stiffness per unit area, S, of the CFL-HB complex was calculated based on the shear deformation formula:

$$\frac{F}{\delta} \sim S = \frac{E_s}{2(1+\upsilon)H_s}$$

Equation 5: Shear Stiffness (per unit area) from (Kondrachuk 2000)

where F is the whisker applied force, δ is the displacement parallel to macular surface, H_s is the height of CFL (12 μm), ν is Poisson's ratio for the CFL-HB complex (between 0.4 and 0.49), and finally, E_s is Young's modulus of CFL-HB complex (E_s=250 Pa). The stiffness (per unit area) of the CFL-HB complex was assumed to be proportional to linear stiffness and estimated to be about 7 x 10^6 N/m^3. In addition, Kondrachuk estimated the stiffness (per unit area) of the sum of all the bundles, to range from 3 x 10^6 – 4.2 x 10^6 N/m^3. This estimation is based on an average density of 6 x 10^9 HB/m^2 (Trinkner, 1962) and a stiffness range of 500-700 μN/m. This yields a shear stiffness contribution of 48-70% of the hair bundles to the shear stiffness of the CFL-HB complex. These results support Besner et al.'s experimental findings: Hair bundles account for 43-60% of total CFL-HB complex stiffness in a bullfrog saccule.

Table 4: Previous Results of HB Stiffness Contribution in the Bullfrog Saccule

Previous results from Benser and Kondrachuk indicate that bullfrog saccule hiar bundles account for as much as 40% of the stiffness in the CFL-HB complex.

	Stiffness of Elemental CFL-HB complex	HB stiffness	Percent contribution of HB
Benser et al. 1993	1350 μN/m	650-950 μN/m	48.1 – 70.4
Kondrachuk 2000	7E6 μN/m^3	3 - 4.2 E6 μN/m^3	42.9 – 60.0

Although this work is not the first attempt at multi-scale modeling of otoconial membranes (Kondrachuk 2001b), it is the first to pair physiologic geometries of an OM, taken directly from confocal images, with models of hair bundles matching

experimentally measured stiffness (Spoon et al. 2005). Using FE models that explicitly and implicitly account for hair bundles in the turtle utricle and bullfrog saccule OMs, contribution of turtle utricle hair bundle stiffness to the shear stiffness of the CFL-HB complex is quantified. In addition, using results from these FE models, a dichotomy between efficient OM displacement transduction to hair bundles and OM displacement magnitudes, with respect to modulus of the CFL-HB complex, is discussed.

3.2 Methods

3.2.1. FE OM Models

3.2.1.1. Bullfrog Saccule Model Information

Benser et al.'s model of the bullfrog saccule consisted of a rectangular plate, with one homogeneous deformable layer consisting of both the CFL-HB complex and the CFL (Benser et al. 1993). The rectangular plate approximates the shape of the saccule and the displacement field approximated from the measured displacement can be integrated over the domain, assuming the elliptical or diamond displacement pattern over the maculae.

Several years later, Kondrachuk constructed a cuboid model of the bullfrog saccule of dimension 540 x 460 μm^2 with a 12 and 48 μm thick CFL-HB complex and CGL, respectively, with 3 degree-of-freedom volume elements (Kondrachuk 2000). From this model of the bullfrog saccule, material properties of each of the layers of this bullfrog organ were approximated. Using the exact same model dimensions and material properties, a method is developed for testing for hair bundle shear stiffness contribution to the CFL-HB complex (see Section 3.2.3). The method is confirmed in the bullfrog saccule against Kondrachuck's (2000) and Benser et al.'s (1993) results.

3.2.1.2. Turtle Utricle Model Information

Turtle utricle OM data is the same is in the previous chapter. The CV3D, true utricle, model was used in this study.

3.2.1.3. Explicit and Implicit Hair Bundles

The goal of this research is to determine the stiffness contribution of hair bundles to the turtle utricle CFL-HB complex. Hair bundle contribution has actually been estimated in the bullfrog saccule, using experiments, analytical (Benser et al. 1993)and finite element models(Kondrachuk 2000). In this chapter two sets of finite element OM

models are used to determine the stiffness contribution of hair bundles to the CFL-HB complex. The first considers the CFL-HB complex to consist of both CFL and hair bundles (See **Figure 16**). Hair bundles are *implicitly* modeled and this layer is treated as a continuous isotropic layer. This model is referred to as the column filament layer & Hair Bundle otoconial membrane (CFL-HB OM) model.

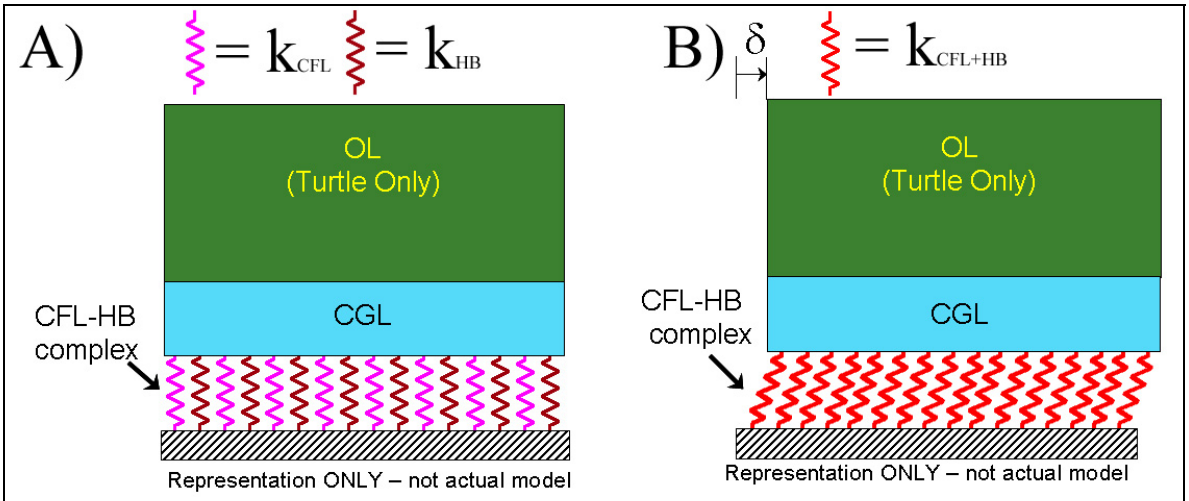

A) CFL and Bundle stiffness act in parallel

B) CFL and Bundle stiffness can be represented with an elemental stiffness. This is a representation of the CFL-HB OM model.

Figure 16: Representation of CFL-HB OM model

In a single degree of freedom system, the stiffness of the CFL (k_{CFL}) represented here with a magenta spring and stiffness of the hair bundles (k_{HB}) represented here with a brown spring (A), have a combined effect on the displacement, δ, of the overlying mass of the system, (or in the case of the bullfrog saccule model, just the CGL), may be represented with one stiffness, whose value (k_{CFL+HB}) is equal to the sum of each individual stiffness represented here with the red springs (B).

For the turtle model, this is the same model as discussed in the previous chapter (CV3D model). For the bullfrog saccule, there is no otoconial layer information available for the bullfrog OM, therefore a model of the same dimension and layer thickness as used by Kondrachuck (Kondrachuk 2000) is used here.

In this model, the CFL and HBs are assumed to work in parallel. Therefore their stiff nesses are additive as shown in **Equation 6**. Here, $k|_{CFL+HB}$ is the stiffness of the CFL-HB complex: both hair bundles and CFL combined. The other stiffnesses are of the CFL, $k|_{CFL}$ and of all of the hair bundles, $k|_{HB}$.

$$k\big|_{CFL+HB} = k\big|_{CFL} + k\big|_{HB}$$

Equation 6: Stiffness in parallel is additive

The second model replaces the elements of the CFL-HB complex with hair bundles (See **Figure 17**), represented with FE Euler-Bernoulli beams, fixed (i.e.: no rotation allowed) to the CGL and fixed to the neuroepithelium (see **Figure 18B**) with equivalent stiffness to experimentally tested hair bundles (Grant et al. 2007). This model is referred to as the Hair Bundle otoconial membrane (HB OM) model, as hair bundles are *explicitly* modeled.

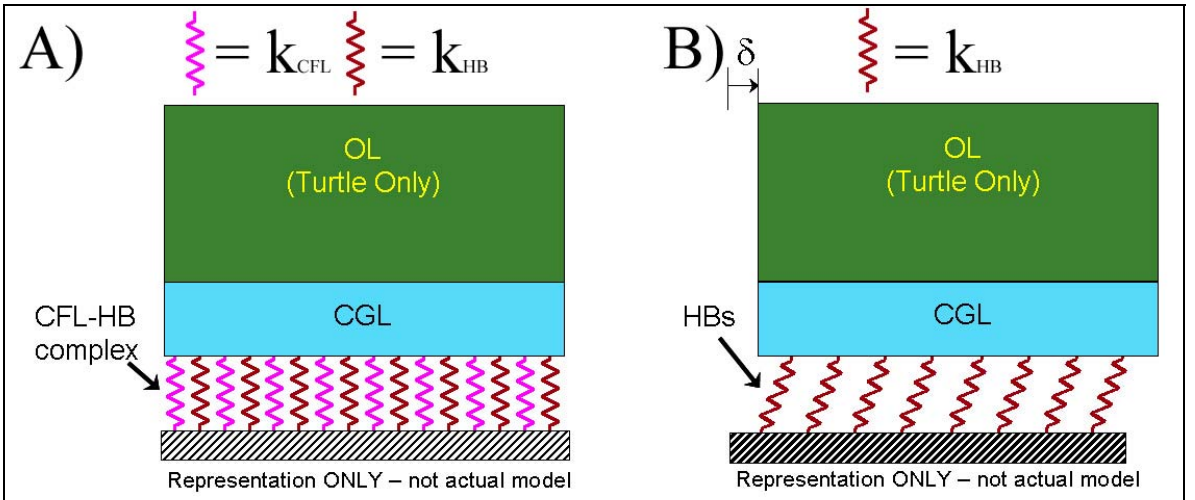

A) CFL and Bundle stiffness act in parallel

B) Removing the CFL from CFL-HB complex leaves just the hair bundles to resist the shear deformation of the OM. This is a representation of the HB OM model.

Figure 17: Representation of HB OM model

This figure illustrates the concept behind the HB OM models of the bullfrog saccule and turtle utricle. In previous OM models, CFL–HB complex is represented with isotropic volume elements that implicitly account for the shear stiffness of the hair bundles.

In B), the HB OM model, the CFL-HB complex is removed and hair bundles are explicitly modeled with FE beams. Comparing the CFL-HB & HB OM models allows for a determination of how much hair bundles contribute to the shear stiffness of the CFL-HB complex. This can be done comparing natural frequency results from modal analysis. Again, since there is no OL layer information available for the bullfrog, only the layers modeled in Kondrachuk's model (2000) were modeled.

The beam elements represent the stiffness of the hair bundles (k_{HB}) for the appropriate animal. They also matched degree of freedom constraints between the solid elements of the CGL and the beam elements representing hair bundles.

3.2.2. Hair Bundle Models

Typical methods used to characterize bundle stiffness require measurements at the kinocilium tip (See **Figure 18A**) (Crawford and Fettiplace 1985; Flock and Strelioff 1984; Howard and Ashmore 1986; Strelioff and Flock 1984). These methods assume that force is transduced to the hair bundle via an attachment to the overlying otoconial membrane. Stiffness is defined as the force applied at the tip of kinocilium divided by linear displacement at the tip of kinocilium.

To model the hair bundles here, Euler-Bernoulli beams with uniform circular cross sections and moduli calculated to estimate the stiffness of the hair bundles were used. The same method of characterizing stiffness is used (linear force over linear displacement); however, the beams are modeled with fixed-fixed (i.e.: no rotational degrees of freedom at either end of the beam) boundary conditions (see **Figure 18B**) in order to preserve the degree of freedom continuity (between beams elements which have displacement and rotation DOFs and solid elements which have just displacement DOFs) in the finite element models.

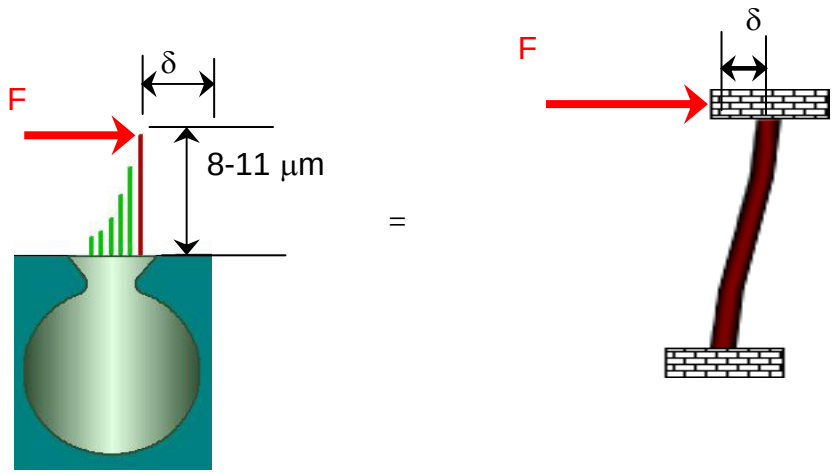

A) Typical Bundle Forcing B) Finite Element Beam representation

Figure 18: Bundle Forcing and Beam Representation

A typical experiment to measure hair bundle stiffness places a glass whisker on the kinocilum and deflects the hair bundle (A). If tip force and (linear) deflection are measured and used to characterize stiffness, then hair bundles may be modeled as beams (B) in which tip force and deflection are used to characterize their stiffness.

In this case, Euler-Bernoulli FE beams, which have displacement and rotational degrees-of-freedom, are used in conjunction with Volumetric FE solids, which have only displacement degrees-of-freedom, the beams used to represent hair bundles will act as if a fixed boundary condition is applied to the beam at the CGL-bundle connection. Thus, experimentally measured stiffness may be matched, considering a fixed-fixed boundary condition in addition to knowing the stiffness of the hair bundle, and geometric properties of the beam, by varying modulus of the FE beam.

Therefore, modulus values calculated from **Equation 7** characterize the fixed-fixed nature of the FE beams and yield the same force displacement characteristics of experimentally tested hair bundles.

$$\frac{\vec{F}}{\delta} = \frac{12\,E_{bundle}\,I}{L^3}$$

Equation 7: Fixed-Fixed Beam Stiffness

|The length of the beam *(L)* is assumed to be the approximate thickness of removed the CFL, and an area-moment of inertia *(I)* to be 7.85E-25 m^4 (calculated from the 1 μm

beam radius). Modulus (E_{bundle}) can then be determined knowing the experimentally measured stiffness ($\vec{F}/\delta - \vec{F}$ is the force applied and δ is the measured displacement of the HB in the same direction as the force) for the different types of bundles.

3.2.2.1. Hair Bundle Parameters

Macular hair bundle count for the bullfrog saccule is approximated to be $6x10^9$ HB/m^2 (Kondrachuk, 2000; Trinkner, 1962) which translates to 1490 hair bundles in the maculae. Since the geometry of our bullfrog OM model allows for only 320 attachment points for hair bundles in the bullfrog saccule model, the modulus of each beam (E_{beam}) is scaled by the ratio 4.66 (1490/320) in order to account for the total number of hair bundles in the bullfrog saccule. This assumes that the hair bundles close to one another work in parallel. Therefore, the full effect of the shear resistance of hair bundles may be approximated by adding their individual stiffnesses. Two stiffnesses for the bullfrog hair bundles were tested: a lower extreme of 500 μN/m and an upper extreme of 900 μN/m (see **Table 5**).

Similar to the bullfrog saccule OM model, the turtle utricle OM model geometry allows for 1305 locations at which beams may be placed to intersect with the CGL. Therefore, the effects of 7.36 striolar bundles are lumped into each beam representing striolar hair bundles. In the MES region, 6.57 MES bundles are lumped into the modulus of a MES beam; this accounts for all 8670 thousand bundles in the utricle (see **Table 5**).

In addition, due to a large variation of and bundle morphology in the turtle utricle the macula of the utricle OM model was divided into two regions: striolar and Extrastriolar. Stiffness values measured from striolar and Extrastriolar bundles (Spoon et al. 2005) are used to calculate modulus based on bundle heights similar to the thickness of the removed CFL (see **Table 5**). The striola is approximated as a region following the curve of the lateral edge of the utricle to be approximately 75 microns wide, starting about 100 microns medial to the lateral edge. This fixed 11 percent of the total number of beam elements to be in the striolar region. This is very similar to the percentage of hair bundles that are located in the striola of the LM transect – (~12 to 13 percent) (Peterson 2004).

Table 5: Geometric & Material Properties of Beam models of Hair Bundles
Variables used to determine modulus of finite element beams representing hair bundles in the bullfrog saccule and turtle utricle OMs.

Variables	Bullfrog Saccule		Turtle Utricle	
	Konrdachuk, 2000	Benser et al.,1993	Spoon et al. 2005	
			striola	Extrastriola
k (μN/m) [Range]	500 [500-700]	900 [650-950]	45 [11-161]	11 [2-25]
r (μm)	1	1	1	1
I (μm^4)	.785	.785	.785	.785
L (μm)	12	12	9.5	14.5
ρ (kg/m^3)	1000	1000	1000	1000
# of HBs/Macula	1490	1490	920	7749
E_{bundle} (kPa)	91.673	165.01	4.093	3.558
# of Beams/Macula	320	320	125	1180
E_{beam} (kPa)	426.85	763.34	30.13	23.37

3.2.3. Stiffness Comparison

Column filament layer and hair bundles have been modeled as working in parallel (Benser et al. 1993). Therefore, the CFL-HB complex may be represented as two springs driven by a superior mass (either CGL or OL). Since they operate in parallel, their stiffness is additive (see **Figure 16**).

Modal analysis is used to determine undamped natural frequency in order to characterize the stiffness of each OM model. Since the undamped natural frequency is directly proportional to the square root of ratio of stiffness to mass, and because the mass driving the system does not change (either in distribution or total mass), the change in the square of the natural frequencies may be interpreted as a change in stiffness. Since the driving mass of the system, the OL, is 8.7 times more massive and over 25,000 times more rigid than CFL-HB complex, it is assumed that replacing the CFL-HB complex with beams representing hair bundles will reflect the change in stiffness more significantly than any change in mass.

Additionally, since it has been shown that OMs have different maximum static displacements depending on the direction of the stimulus, it is more convenient to compare undamped natural frequencies of the characteristic modes of the OM, thus

eliminating the need to find and compare maximum static deflection directions (Jaeger and Haslwanter 2004; Jaeger et al. 2002). The average directions of deflection of the first two modes align with the maximum and minimum static sensitivities when the modulus of the CFL-HB complex is assumed to be linear elastic.

The first two undamped natural frequencies are of interest for three reasons:

(1) These low natural frequencies require the least amount of energy to excite and thus are generally most commonly observed.

(2) The displacement mode shapes (displacement profile of the whole OM at specific frequencies) corresponding to these natural frequencies represents the characteristic motion of the OM: a shearing of the CFL-HB complex.

(3) The direction of displacement in modes 1 and 2 is close to the direction of maximum and minimum static deflection directions since linear elastic moduli are being used in the models. This may change if the CFL-HB modlus is discovered to be nonlinear.

Undamped natural frequencies of the structure can be used to make conclusions about the stiffness of that structure. In the case of otoconial membranes it is assumed that the hair bundles work in parallel with the surrounding CFL. This has been modeled as two springs working in parallel (Benser et al. 1993). Their effective stiffness is calculated by adding the two individual stiffnesses, representing both working in parallel (see **Figure 16**).

If the total and distribution of the driving mass are the same in each model, the transition to natural frequencies can easily be made by dividing stiffness by the mass of the system. This ratio represents the square of the natural frequency. In the case of the CFL-HB models, this ratio is $\omega_n^2|_{CFL\text{-}HB}$. And in the case of the HB-OM models, where the CFL-HB complex is replaced with just hair bundles, this natural frequency is $\omega_n^2|_{HB}$.

$$\omega_n^2\Big|_{CFL+HB} = \omega_n^2\Big|_{CFL} + \omega_n^2\Big|_{HB}$$

Equation 8: Stiffness contribution of HBs and CFL can be separated using natural frequencies

Therefore if hair bundles dominate the shear stiffness of the CFL-HB complex, the HB model will have natural frequencies close to the natural frequencies observed in

the CFL-HB model. The percent contribution to the total stiffness is calculated using the square of the natural frequencies from each model. For example, a 50 percent shear stiffness contribution of hair bundles to the shear stiffness of the OM would see the natural frequency of the CFL-HB model scale by a factor of the square root of two, over the natural frequency of the HB model.

3.3 Results

The shear stiffness contribution of hair bundles to the CFL-HB complex was analyzed. Results from two sets of finite element models (CFL-HB and HB) of both the bullfrog saccule and turtle utricle are compared. Recall that the CFL-HB model implicitly models hair bundles, considering the CFL-HB complex as one (isotropic volume element) layer. Additionally, the HB model explicitly models hair bundles by removing the CFL, leaving just hair bundles (beam elements) in this layer of the OM. Therefore, if hair bundles dominate the stiffness, then the undamped natural frequencies from each FE model will be close to one another.

3.3.1. Bullfrog Saccule

Previous work to measure the shear stiffness contribution of hair bundles to the CFL-HB complex in the bullfrog saccule has yielded similar results (Benser et al. 1993; Kondrachuk 2000). This begins with the CFL-HB bullfrog saccule model, in which model dimensions come from Kondachuck's work (2000). The resulting natural frequencies and percent contribution of HB stiffness are shown in **Table 6**.

Next, the CFL-HB complex is removed from the bullfrog saccule model, and this layer is replaced with finite element beams whose material properties approximate the stiffness of the bullfrog saccule hair bundles. Moduli were calculated assuming geometric characteristics of a beam shown in **Table 5**. In the first case, the stiffness for the bundles is assumed to be 500 μN/m; the lower extreme of bullfrog bundle stiffness. In the second case, hair bundles were assumed to have a stiffness of 900 μN/m. This is near the upper extreme of the bullfrog bundle stiffness reported by Benser et al. (1993). The results shown in Table 4, indicating a 42 to 70 percent stiffness contribution on HBs to the CFL-HB complex matching the experimental measurements of Benser et al. (1993) and the modeling results from Kondrachuk(Kondrachuk 2000) (2000).

Table 6: Percent contribution of stiffness of HBs to stiffness of CFL-HB for two displacement modes of the bullfrog saccule models.

Also indicated in square brackets is the natural frequency of each mode.

Bullfrog Saccule Model	Mode 1	Mode 2
CFL-HB [ω_n (Hz)]	N/A [1809]	N/A [1812]
OM with explicit HB : (k_{bundle}=500 μm/m) [ω_n (Hz)]	42.05 % [1173]	41.98 % [1174]
OM with explicit HB : (k_{bundle}=900 μm/m) [ω_n (Hz)]	71.53 % [1530]	71.48 % [1532]

3.3.2. Turtle Utricle

The datum to which the results from the turtle utricle models are compared, are natural frequencies of the CFL-HB Turtle Utricle model from Chapter 2. The first two natural frequencies are listed in **Table 7**. Next, the CFL-HB complex is removed and replaced with beams of modulus prescribed in **Table 5**. Stiffness of the CFL decreases significantly. Natural frequencies for the first two displacement modes for the utricle OM model with just hair bundles are listed in **Table 7**.

Table 7: Percent contribution of stiffness of HBs to stiffness of CFL-HB for two displacement modes of the turtle utricle models.

Also indicated in square brackets is the natural frequency of each mode.

Turtle Utricle Model	Mode 1	Mode 2
CFL–HB ($E_{CFL\text{-}HB}$ = 250 Pa) [ω_n (Hz)]	N/A [1530.19]	N/A [1591.64]
HB OM : (k_{STR} = 45 μN/m; k_{MES} = 11 μN/m) [ω_n (Hz)]	3.15 % [271.459]	3.10 % [280.413]
HB OM: Increase k_{MES} (k_{STR} = 45 μN/m; k_{MES} = 11*<u>*20*</u> μN/m) [ω_n (Hz)]	42.3 % [995.192]	45.56 % [1074.43]

These results indicate that the turtle utricle hair bundles do not dominate the stiffness in this OM layer, accounting for less than 3.25 % of the total layer stiffness. CFL-HB complex stiffness is proportional to the square of 1530 Hz, and the shear stiffness contribution of the hair bundles (for the similar mode) is proportional to the square of 271 Hz. Thus, the stiffness contribution of the hair bundles accounts for only about 3.15 percent of the total stiffness.

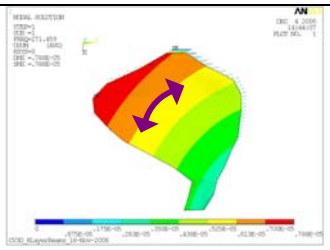

A) Mode 1: ω_n = 271.459 Hz

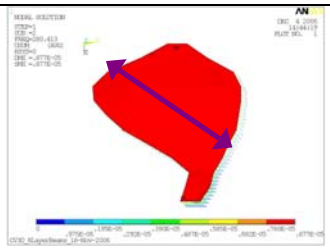

B) Mode 2: ω_n = 280.413 Hz

Figure 19: Mode Shapes for HB Turtle Utricle

The first two resulting displacement modes for the HB turtle utricle model are shown here. The first displacement mode (A) indicates an anterio-lateral/posterio-medial displacement of the OL while the second displacement mode (B) indicates anterio-medial/posterio-lateral displacement. These displacement modes are not exactly the same displacement modes as those characteristic to the CFL-HB turtle utricle models. But they are similar in that they represent a shearing of the underlying hair bundles. The relatively low natural frequencies associated with each mode show that the hair bundles are too weak to dominate the stiffness of the turtle utricle given the information currently available on its structure.

There are two additional questions that must be considered:

1) How much would the stiffness of bundles in the ES region have to increase, accounting for the different forcing location (along the kinocilium as mentioned in section 2.4.2.2) in ES bundles, in order for the bundles to account for at least 42 percent of the stiffness of the CFL-HB complex?
2) How low would the modulus of the CFL-HB complex have to be in order to have the turtle utricle hair bundles, as they are currently modeled, account for at least 42 percent of the stiffness in the utricle OM?

To answer the first question, modulus of the ES beams can be adjusted until their stiffness is enough to drive the natural frequency of the HB-OM model to approach the natural frequency of the CFL-HB turtle utricle model. Extrastriolar beam moduli must increase 20 fold, in order to contribute stiffness proportional to that of the minimum observed in the bullfrog (see **Table 8**).

A 20 fold increase translates to a stiffness of 220 μN/m. This is beyond the range of even the stiffest bundle in the turtle utricle and is probably an unattainable increase in stiffness by only moving the point at which the ES bundle attaches to the OM.

To answer the second question, the modulus of the CFL-HB layer is reduced until the natural frequency approaches that of the natural frequency of the HB model. In order for the hair bundles to account for approximately half of the stiffness of the CFL-HB complex, the modulus must be reduced to less than 10 % of the original CFL-HB model shear layer modulus: from the 250 Pa to 16 Pa. This begs to question: Is safe to assume that these material properties are constant across species or organs?

This second question is also yet to be answered experimentally; however, the impact of this reduction in CFL-HB layer stiffness on hair bundle stimulus may be determined with the model. The result of the modulus reduction is an approximate 20 fold increase in OM displacement, and to follow, a potential increase in hair bundle displacement.

Table 8: Percent contribution of stiffness of HBs to stiffness of CFL-HB complex for three displacement modes of the turtle utricle models.

This table shows the percent contribution of hair bundles to the stiffness of the CFL-HB complex sublayer of the turtle utricle assuming that hair bundles ***should*** contribute about 40-70 percent of the stiffness (the same as in the bullfrog saccule OM). Also indicated in square brackets is the natural frequency of each mode.

Turtle Utricle Model	Mode 1	Mode 2
CFL–HB: Reduce $E_{CFL\text{-}HB}$ ($E_{CFL\text{-}HB}$= 16 Pa) [ω_n (Hz)]	N/A [392.564]	N/A [408.387]
HB: (k_{STR} = 45 μN/m; k_{MES} = 11 μN/m) [ω_n (Hz)]	47.8 % [271.459]	47.1 % [280.413]

The problem with a lower modulus for the CFL-HB complex in the turtle utricle is the increase in OM deflections. With modulus of 16 Pa OM displacement magnitudes increase to approximately 3-5 microns for a 1 g load. This is within the operating range of ES hair bundles but are beyond the operating range of striola hair bundles (hundreds of nanometers) (Nam et al. 2005a). With our linear model, displacements will increase linearly with respect to the load applied. For example, a 2G load would present displacements on the order of 6-10 microns; these large displacements maybe damaging to hair bundles.

3.4 Discussion

3.4.1. Mode of Operation

Saccules have been shown to be acoustic (i.e. velocity) and seismic (i.e.: displacement) sensors (Ashcroft and Hallpike 1934; Fay 1984; Fay and Edds-Walton 1997; Lowenstein and Roberts 1949; Lowenstein and Saunders 1975). This theory is supported mechanically with the turtle, as the saccule has a larger OL mass than found in its utricle (see **Figure 25**). The large mass drives the natural frequency of the system down, to a point where the displacement response to displacement excitation gain is flat at the high frequencies, making the saccule ideal for detecting sound or seismic activity (Meirovitch 1986). Utricles, on the other hand, may act as accelerometers (Davis and Grant 2004; Grant et al. 1994). In the turtle, utricles have a smaller OL mass than the saccule, which would drive the natural frequency of the system up. This makes the utricle an ideal sensor for detecting acceleration up to the lowest natural frequency of the system (Meirovitch 1986). At frequencies above the lowest natural frequency, system dynamics begin to interfere with the utricles ability to transduce OM state information without phasing issues.

3.4.2. Damping Effects on Dynamic Range

To investigate the effects of damping on the dynamic range of the utricle, a Single Degree of Freedom (SDOF) model whose natural frequency is the same as the first undamped natural mode in the turtle utricle (1530 Hz), is used. This frequency is much higher than hair bundles have been known to operate (Denk et al. 1989). However, otoconial organs may be considered over damped systems (Wilson and Melvill Jones 1979) (near critically damped in the frog saccule (De Vries 1951)) and thus dynamic range is attenuated by damping in the system.

The SDOF transfer function in **Figure 20** shows displacement of the otolith relative (X_{OL}) to acceleration (a) of the skull at indicated damping ratios (ζ). Damping ratio is a measure of the viscous damping in the system relative to the damping that would provide the fastest response of the system: critical damping. Higher damping values, suggested by Grant et al. (Grant et al. 1994) who suggest that an otoconial organ can be damped as much as twenty times critical, are also shown.

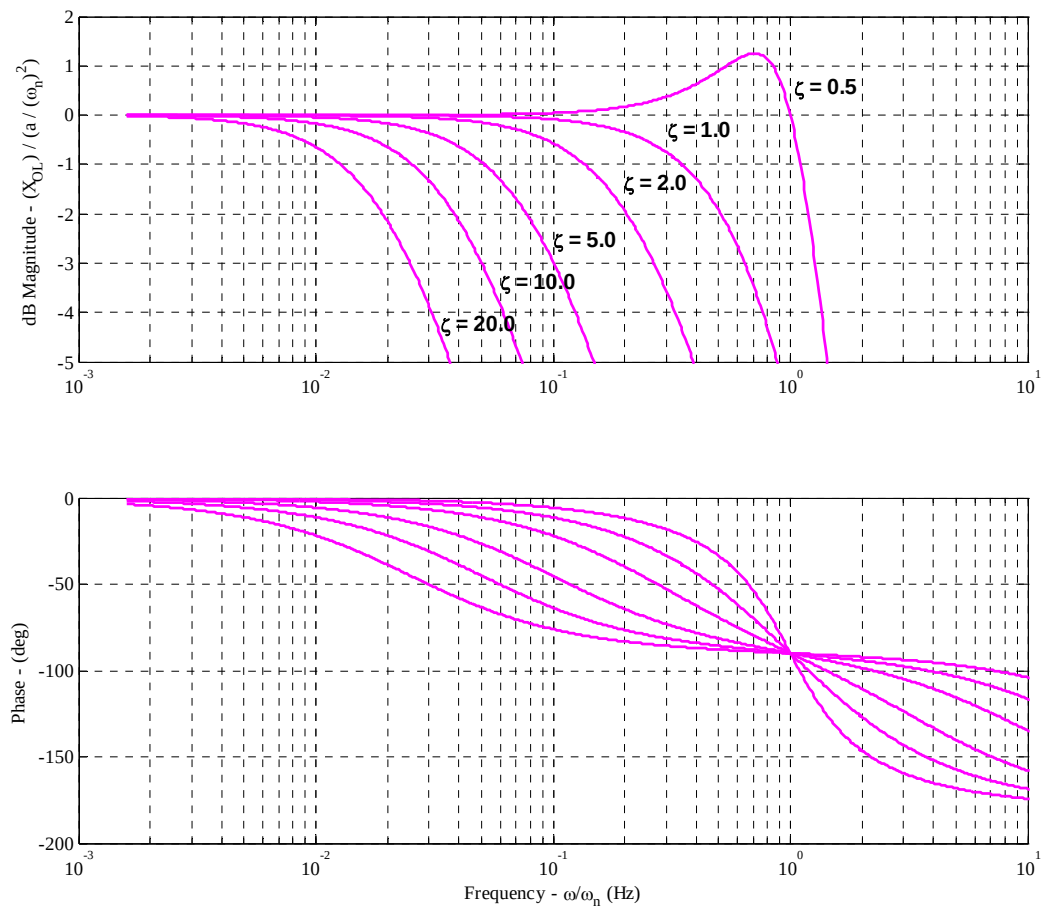

Figure 20: Non-Dimensional Single Degree of Freedom Otolith Transfer Function with Various Levels of Damping

This figure illustrates the effect of damping on the low frequency displacement modes of the turtle utricle using a non-dimensional Single Degree of Freedom Model (Grant et al. 1994). Notice that the dynamic range of the system decreases with damping, as expected. Displacement is scaled here to acceleration and ω_n^2.

The cutoff frequency (ω_{cutoff}), capturing the upper limit of the dynamic range of the OM, is located 3 dB down from the flat gain, and can be estimated from the natural frequency (ω_n) and the damping ratio (ζ):

$$\omega_{cutoff} = \omega_n \zeta - \omega_n (\zeta^2 - 1)^{0.5}$$

Equation 9: Cutoff Frequency (Meirovitch 1985)

Note how the cutoff frequency is dependent on natural frequency and damping of the system. The over-damped OM acts as a low-pass-filter, efficiently transducing displacements between zero hertz and the upper limit of the dynamic range. So, for the turtle utricle, the dynamic range of the utricle OM is between zero and 38.27 Hz if the OM is 20x critically damped. However the dynamic range is expanded by an order of magnitude, between zero and 409 Hz, if the OM is 2x critically damped.

However, damping would not affect the magnitude of the deflection in a seismometer (displacement of OL relative to displacement of skull) for high levels of frequency (ω/ω_n). Damping may effect the phase of the response, but for high frequencies, the gain approaches unity for all levels of damping. Therefore, if a seismometer has a low natural frequency and operating frequencies at least 2 or 3 times ω_n is probably fairly reasonable, then damping should not be a factor for detecting the magnitude of the motion for a seismometer (Meirovitch 1986).

3.4.3. Hair Bundle Displacement and CFL-HB modulus

Although reducing the modulus of the CFL-HB complex may provide more efficient transduction of OM displacement to hair bundles (similar frequency operating ranges), this may be turn out to be unnecessary and damaging to the bundles. Reducing the modulus of the CFL-HB complex would put bundle displacement in the range of 6-10 microns for typical accelerations. This is too large a displacement for striolar bundles whose full operating range is on the order of approximately 200 nm (Nam et al. 2005a). Not even the thicker CGL and CFL in the striolar region of the turtle utricle would be enough to attenuate the deflection in the striolar region to within the operating range of a turtle utricle striolar hair bundle. Thus, if the modulus were lowered in the turtle utricle to the magnitude (i.e.: 16 Pa) that has been used in other models (Grant et al. 1984; Grant and Cotton 1990; Kondrachuk 2001a; b), the bundles may not survive an average stimulus. Remember that damping in the system may also help attenuate the dynamic range of the otolith organs. This is just more evidence that the CFL modulus is within a reasonable range but also opens the door to question if there is also different damping ratio’s between organs.

3.4.4. Limitations of this study

Some limitations of this study are that the hair bundle models only consider the static stiffness of the bundles. As the hair bundle deflects and tip links are stretched, the stiffness of the bundle changes (Nam et al. 2007). Further modeling efforts could include non-linear stiffnesses to account for these changes.

Also the finite element beams representing hair bundles were not placed in physiologically accurate locations on the maculae. Although striolar and ES bundles were differentiated in this study, physiologic placement of hair bundles may give rise to reasons for the different hair bundle morphologies and/or function. Future modeling could start with mesh design from the locations of hair bundles.

CHAPTER 4. Effects of Position and Orientation on the Stimulus at the Utricle

ABSTRACT

Quantifying the stimulus to the utricle is a necessary step in understanding how hair bundles are stimulated naturally. Natural motion of a turtle head is characterized by digitizing & analyzing high speed videos of a turtle during a feeding strike. This provides kinematic data of the head during its motion. Computed tomography (CT) of the turtle head is used to determine the position and orientation of the utricle relative to the head. High speed videos are used in conjunction with CT to determine the stimulus at the utricle.

This chapter outlines the methods used to determine natural stimulus at the utricle. In addition, the effects of orientation on the static mechanical gain are discussed using the previously developed FE model.

4.1 Introduction

Motion and orientation of the head is transmitted through the skull to the vestibular system, which consists of semicircular canals (SCC) (and ampullae) and otoconial organs. These end organs translate head motion and orientation into neural signals by inertially deflecting hair bundles located in either a gelatinous cupula, in the ampulla of SCC, or in the column filament layer (CFL) of otolith organs. As a result of hair bundle displacement, ion channels in individual stereocilia are opened, allowing calcium/potassium ions to flow into the hair cell. This inward flow if an ion depolarizes the hair cell to which the bundle is attached and results in a synaptic relay transmitted to the central nervous system for processing. The magnitude of the response generated is dependent on several elements, one of which is the magnitude of the deflection of the hair bundles within the cupula or CFL as a result of external stimulus. The external stimulus can also be dependent on both orientation and location of the organ within the head.

4.1.1. Utricle Orientation

Previous studies have shown utricle OL deflection to be proportional to acceleration (Lowenstein and Roberts 1949). There is also evidence that utricles are not necessarily oriented in the horizontal plane (Braemer and Braemer 1958; Corvera et al. 1958; Curthoys et al. 1999; Jaeger and Haslwanter 2004). Therefore, determining the utricle's orientation and location in the head (relative to planes of symmetry and external visible landmarks) is crucial to determining the magnitude of acceleration transduced by this end organ during motion of the head. In addition, orienting the utricle relative to the head may help explain the some behaviors of the animal. It has been proposed as far back as 1958 that body orientation could be related to the orientation of the utricular macula. In this study fish were observed positioning their bodies such that the plane of the utricle was close to earth's horizontal plane (Braemer and Braemer 1958). In addition, Curthoys et al. (1999), indicate that the orientation of the utricle maculae in the guinea pig is very close to horizontal, approximately 5 degrees pitched down from horizontal plane, when the it's head is held in a "natural head position:" pitched down 30 degrees relative to stereotaxic horizontal.

Similar observations with the turtle indicate that turtles pitch their heads breaking the surface of water while swimming freely (Peterson and Ulinski 1979). In the Peterson and Ulinski (1979) study, the iris line of the turtle was observed to be in the earth horizontal plane. However, the plane of the utricle could also be in the horizontal plane, thereby maximizing non-visual reflexes interpreted from the vestibular system, in order to stabilize vision while floating.

In this chapter, orientation and position of the utricle in a turtle head is investigated. The effect of in-vivo orientation and position on utricle OM deflection is determined using micro computed tomography (μ–CT), high speed videos of turtle feeding strikes collected by Dr. Blob (Clemson University), and a finite element model of the turtle utricle. In addition the effect of orientation on the static mechanical gain is determined.

4.2 Methods

4.2.1. High speed video kinematics

Turtle feeding strikes are recorded using high speed video cameras, collecting frames at a rate of 100 frames per second. Turtles are placed in a water filled tank and are enticed with food (a worm) which is placed within the viewing frame of the camera. Motion of the turtle's head during the feeding strike is captured on video. Three reference points on the turtle head are used in order to track the kinematics of the head in high speed videos of a turtle feeding. They are: 1) the tip of the nose, 2) the tip of the upper jaw, and 3) the hinge of jaw on the right side of the turtle's head. There is an additional point on the plastron to locate the body of the turtle. These points are digitized in each frame of the feeding strike to record their position relative to the tank.

Displacements are calculated from the digitized position markers in the high speed videos of the turtle feeding. The data is smoothed and differentiated using techniques discussed in Walker (Walker 1998). Accelerations experienced by the utricle are calculated using one of the first three points and the five part acceleration, shown in **Equation 10**. Here, $\vec{a}_{UTR}$ is the acceleration at the COM of the utricle OL, $\vec{a}_{NS}$ is the acceleration of the nose, $\vec{r}_{NS-UTR}$ is the vector between the nose and the COM of the utricle OL, $\vec{\alpha}$ is the angular acceleration of the head, $\vec{\omega}$ is the angular velocity of the head, $\vec{a}_{rel}$ is the relative acceleration between the COM of the utricle OL and the nose, and $\vec{v}_{rel}$ is the relative velocity between the COM of the utricle OL and the nose: all of which are vector quantities. The relative kinematics $\vec{a}_{rel}$ & $\vec{v}_{rel}$ are assumed to be negligible due to the small distances between the epithelium (which should have the same

velocity and acceleration as the head landmarks) and the COM of the utricle OL. The acceleration measured at the nose (and jaw) is referenced to an inertially fixed reference frame.

$$\vec{a}_{UTR} = \vec{a}_{NS} + \vec{\alpha} \times \vec{r}_{NS-UTR} + \vec{\omega} \times \vec{\omega} \times \vec{r}_{NS-UTR} + \vec{a}_{rel} + 2\vec{\omega} \times \vec{v}_{rel}$$

Equation 10: Acceleration of the utricle relative to acceleration of the tip of the nose

Angular acceleration and angular velocity vectors are also calculated from the video data. This is done by tracking the 3 digitized points from the high speed video. A body fixed coordinate system is established using the vector between the nose and the jaw-tip as the b1 direction. The two remaining mutually orthogonal coordinate axes are determined using vector cross products. Angular velocities and accelerations are determined by tracking the movement of this body fixed reference frame in the Newtonian fixed N-frame. This process is outlined in Appendix B.

4.2.2. Micro-CT (μ-CT) imaging & Visualization

To visualize the marker locations used in the high speed video in the μ-CT, a barium paste (see **Figure 21**) was placed on the turtle head at the same locations. A Scanco Viva CT 40 was used, with the help of Dr. Chris Wyatt (SBES & EE at Virginia Tech), to collect the CT micrographs. The barium paste will show up in the CT micrograph as a hot spot allowing us to locate the maker locations used in the high speed video.

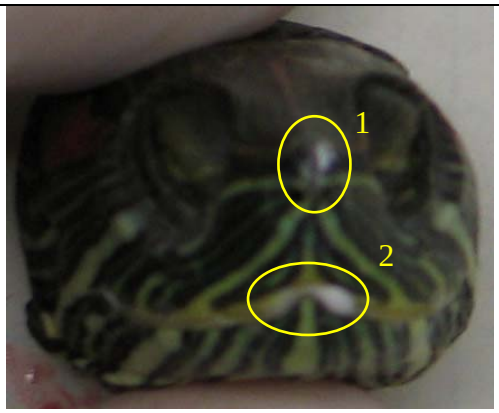

A) Front View of Markers

B) Side View of Markers

Figure 21: Turtle Head marked with Barrium Paste before Micro CT scan

The turtle head was marked with barrium paste at the same three locations indicated in . The barrium will show up at hot spots in the CTs and allow for calcualtion of relative position vectors between utricle OL and video capture marking locations. This information can be used to calculate acceleration at the utricle in conjuction with acceleration results from video capture.

The turtle head was placed in a μ-CT, and the whole turtle head was imaged. Over 2000 images at 19 micron increments (19 micron sided voxels) were collected and analyzed. The resulting micrographs are used to determine position and orientation of 1) the saccule and utricle otoconial organs, 2) the barium paste (marking locations for kinematic measurements on the turtle head) and 3) the mid-sagittal suture.

4.2.2.1. Aligning Skull with Planes of Symmetry

Roll and yaw angles are zeroed relative to the Cartesian planes using the location in which the columnella transitions through the outer ear to the middle ear on the left and right sides of the head as points of symmetry. This approximately aligns the turtle skull in with the frontal and horizontal planes. (These rotations were checked with mean position of the barium jaw hinge marker on the left and right side of the turtle head.)

To align the collected μ-CT data to the rest position in the sagittal plane, line PCA (Brichta et al. 1988) (see **Figure 22**) along the mid-sagittal suture was used.

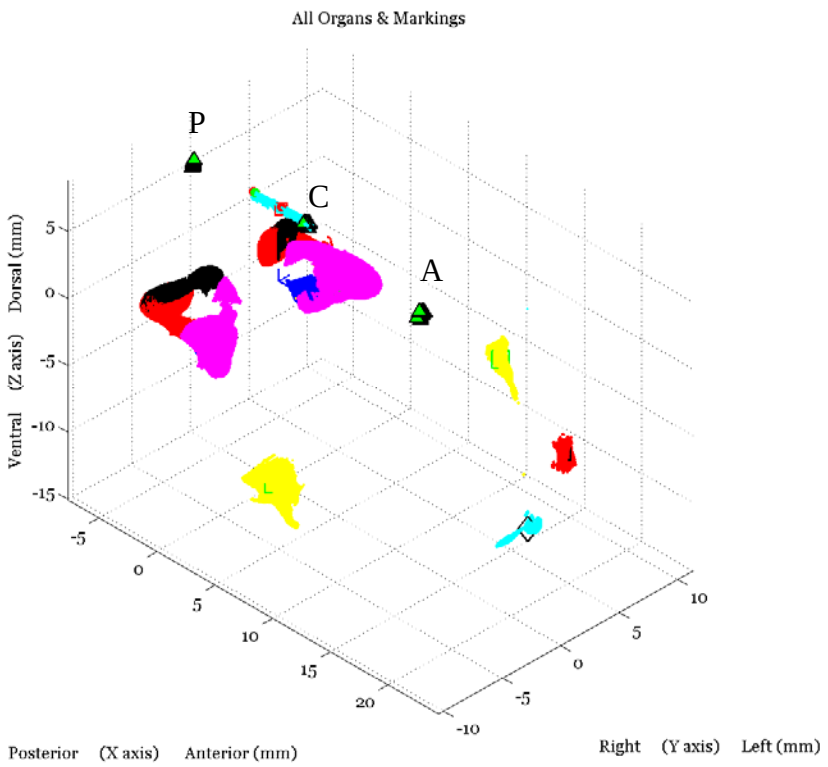

Figure 22: Line PCA is used to orient the pitch of the turtle's head

In order to orient the turtle head to the rest position line PCA was approximated on the mid-sagittal suture. In A) an image from Brichta et al. (1998) shows the points used to align the turtle head with stereotaxic horizontal. In B) these points were mimicked in the CT scans, for the same purpose.

Line PCA was determined by first approximating the location of point C: the location of where ear bars would be used to hold the turtle's head in a stereotaxic holder. This was done by approximating the deepest point into which "ear-bars" of a stereotaxic holder could be placed into the ear of the turtle, (see **Figure 23**), from the images collected from the μ-CT.

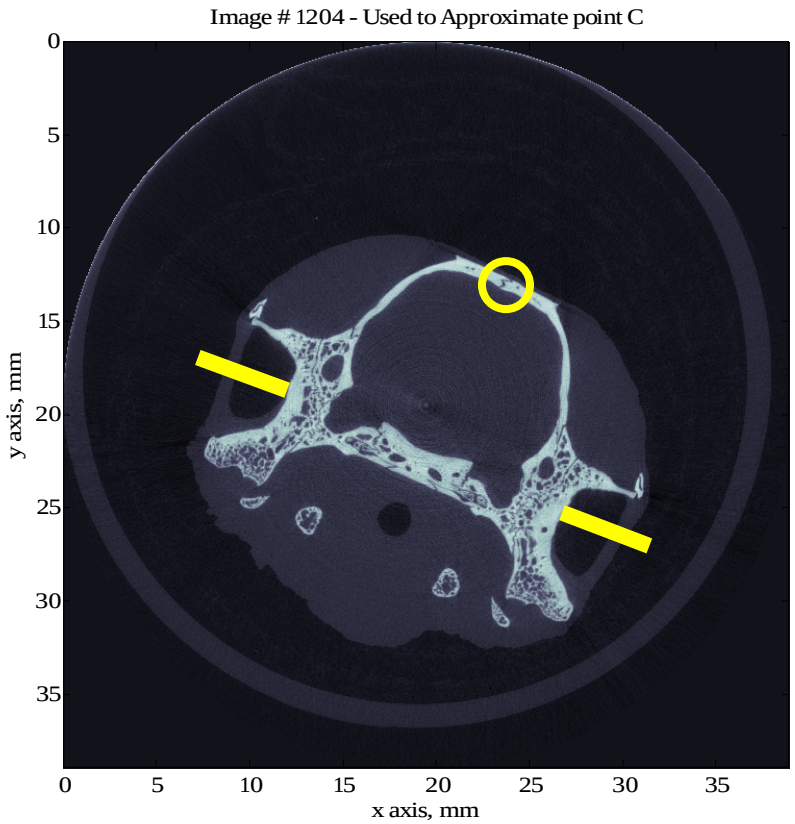

Figure 23: Approximate Location for center of skull (Point C)

Image 1204 was selected to approximate point C (Yellow Circle), this is the section in which the bony cavity of the ear reaches deepest into the head. This is a crude approximation of where the ear bars (Yellow Lines) might be when using a stereotaxic holder. Future studies could include a stereotaxic holder for the μ-CT.

Points A and P were then determined to be 1cm in the anterior and posterior directions along the mid-sagittal suture, respectively. Pitch is adjusted until the line segment connecting P and C is positioned at an angle of 3.4 degrees (anterior end up) relative to earth horizontal. This is the position of the skull in the rest position (Brichta et al. 1988). It is understood that changes in the location of point C, which is approximated, will influence the results of the angles of the utricle, but the influence should be slight. If point C were to move posteriorly on the skull, the pitch of the utricles would increase slightly, as point P would decrease its Z coordinate and vice-versa if point C were to move in the anterior direction.

4.2.2.2. Imaging Otoconial Organs

The utricle and saccule of the red ear slider are located and oriented using the otoconia crystals of the end organ. The OL of both utricles and saccules are outlined in each of the CT micrographs in which they appeared (**Figure 24 A** & **B** – yellow ovals) using a Matlab™ Graphical User Interface (GUI) written by myself to collect the data. The GUI automated the loading of images and saving of data files. The outer boundary of the OL was collected from visual inspection of each image.

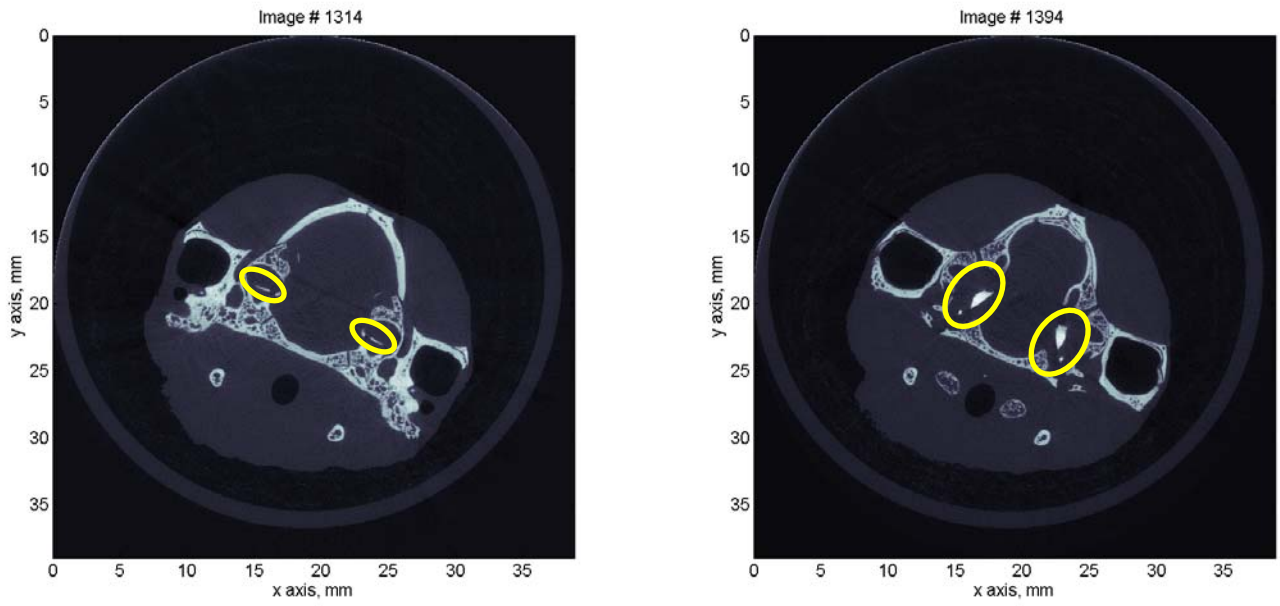

A) Frontal image showing Utricle Otoconial Layer B) Frontal image showing Saccule Otoconial Layer

Figure 24: Otoconial organs are evident through the calcium carbonate crystals that make up the OL

Otoconia crystals of the otoconial organs in the turtle show up as hot spots in the μ-CT scan of the turtle head. From these images the approximate shape and orientation of the OL of the utricle (A) and saccule (B) are determined.

4.3 Results

4.3.1. Organs & Kinematic Measurement Locations

The average of the each otoconial organ curve fit data was determined, thereby approximating the location of the center of mass (COM) of the collection of otoconia crystals in the saccules and utricles. This position can be related to the locations used for kinematic measurements, which are approximated by the mean position of the barium

paste markings. Results are shown in **Figure 25**. Using the relative positions, **Equation 10**, and kinematic data from digitized high speed video, acceleration experienced by the utricle can be approximated.

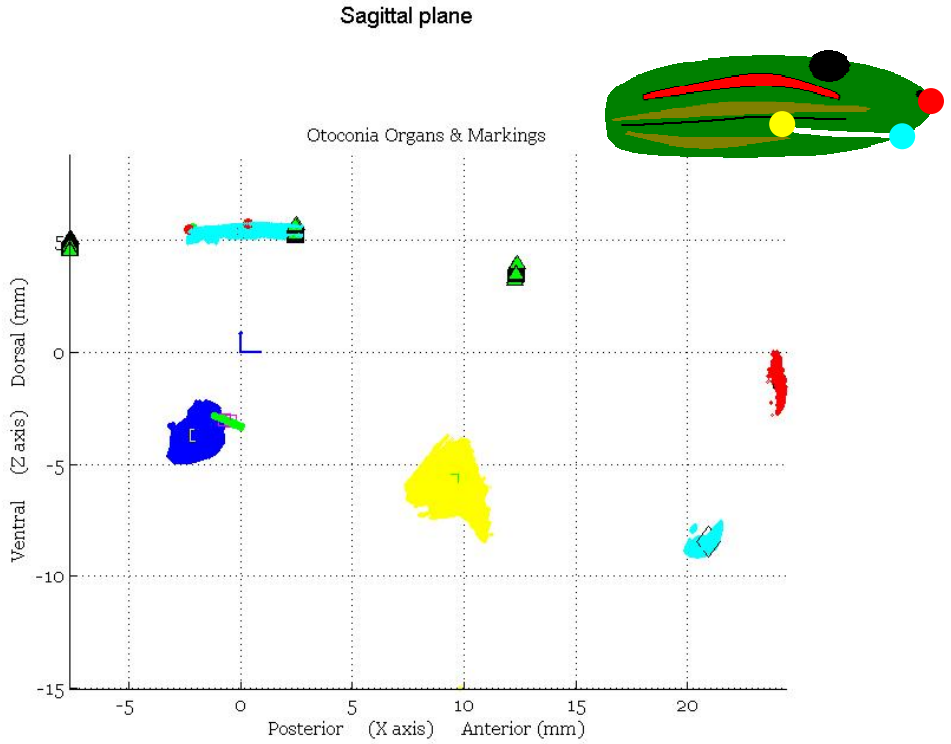

Figure 25: Otoconial Organs and Barium Markings shown in the sagittal plane
These are the results from the CT indicating relative positions between markings used in video tracking studies and position and orientation of the otoconial organs of the turtle.

Green – Utricle (Center-Magenta Square)
Blue – Saccule (Center-Yellow Square)
Cyan – Mid Sagittal Suture
Yellow – Jaw Hinge
Cyan – Jaw Tip (Center – Black Diamond)
Red – Nose Tip

Table 9: Coordinate Means of Indicated Data Sets

These are the locations of the means of each data set shown in **Figure 25**. For the utricles and saccules, this represents the location of the center of mass of the OL of each organ.

Note: +X = Anterior; +Y = Left, +Z = Dorsal

Mean Position	Left			Right		
	AP [X] (mm)	LM [Y] (mm)	DV [Z] (mm)	AP [X] (mm)	LM [Y] (mm)	DV [Z] (mm)
Skull	0.1458	0.0585	5.4080			
Nose	24.0933	0.6530	-1.3445			
Jaw Tip	20.9281	0.6342	-8.4477			
Jaw Hinge	9.4164	9.6938	-5.9462	9.3020	-9.6236	-5.8901
Utricle	-0.4731	4.7861	-3.0888	-0.7471	-4.5708	-3.0135
Saccule	-1.8870	3.8553	-3.6760	-2.0024	-3.6737	-3.6755

4.3.2. Planar Fits of Utricle OL

Utricle OL planar fits are used to approximate the orientation of the utricle relative to the defined coordinate planes. Their orientation in the turtle's head will affect the magnitude of the stimulus observed by the organ. From these results, the position of the utricle while the turtle's head is in a rest position may be inferred from Brichta et al. (1998). The utricle is pitched anterior end down, approximately 24 degrees from the horizontal plane, and rolled lateral end down approximately 6 degrees (also measured from the horizontal plane), while the head is in a rest position.

Table 10: Utricle Fit Data

These are the results of planar fits of the utricle OL. Given here are the equations for each utricles plane, the goodness of the fit, and the normal vector to the plane. This normal vector will later be used to determine the pitch and roll of the utricle OL.

Utricle	Equation for Fit Plane	Goodness of fit (R^2)	Pitch (deg)	Roll (deg)
Right	Z = –0.4501 X + 0.1103 Y – 2.8458	81.33%	24.23	6.29
Left	Z = –0.4604 X – 0.1185 Y – 2.7393	85.93%	24.72	-6.75

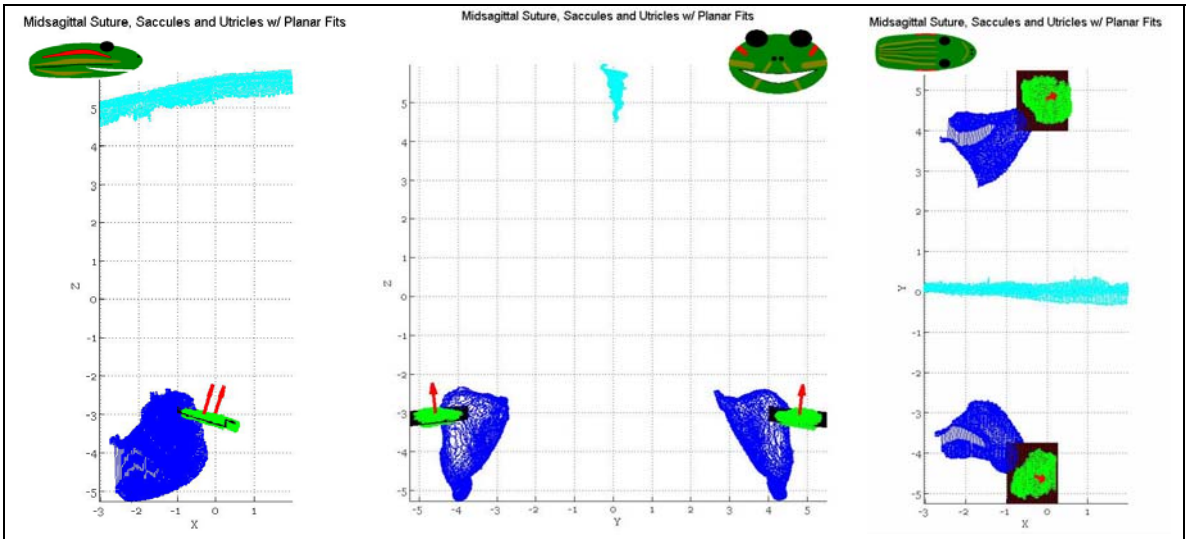

A) Sagittal B) Frontal C) Coronal

Figure 26: Planar fits of utricles and their normals as viewed in different planes of symmetry

Shown here are the Utricles in Green, Saccules in Blue, and the Mid-sagittal suture in Cyan. Utricle planar fits, Dark Red, are shown passing through the utricle OLs with the normals to these planes indicated with red arrows.

4.3.3. Acceleration at the utricle in the N-Frame

Knowing the relative position and orientation of the utricle, the acceleration experienced by the utricle during the recorded motion of the turtle head may now be calculated. The following calculations, assume relative accelerations and velocities to be negligible. These parameters would account for any relative motion between the OL of the utricle and measurement locations used in the motion capture. The data presented is calculated from velocities and accelerations from the tip of the nose to the utricle (see **Figure 27**). The tip of the nose was found to be the most accurate location from which to calculate acceleration (Blob 2007).

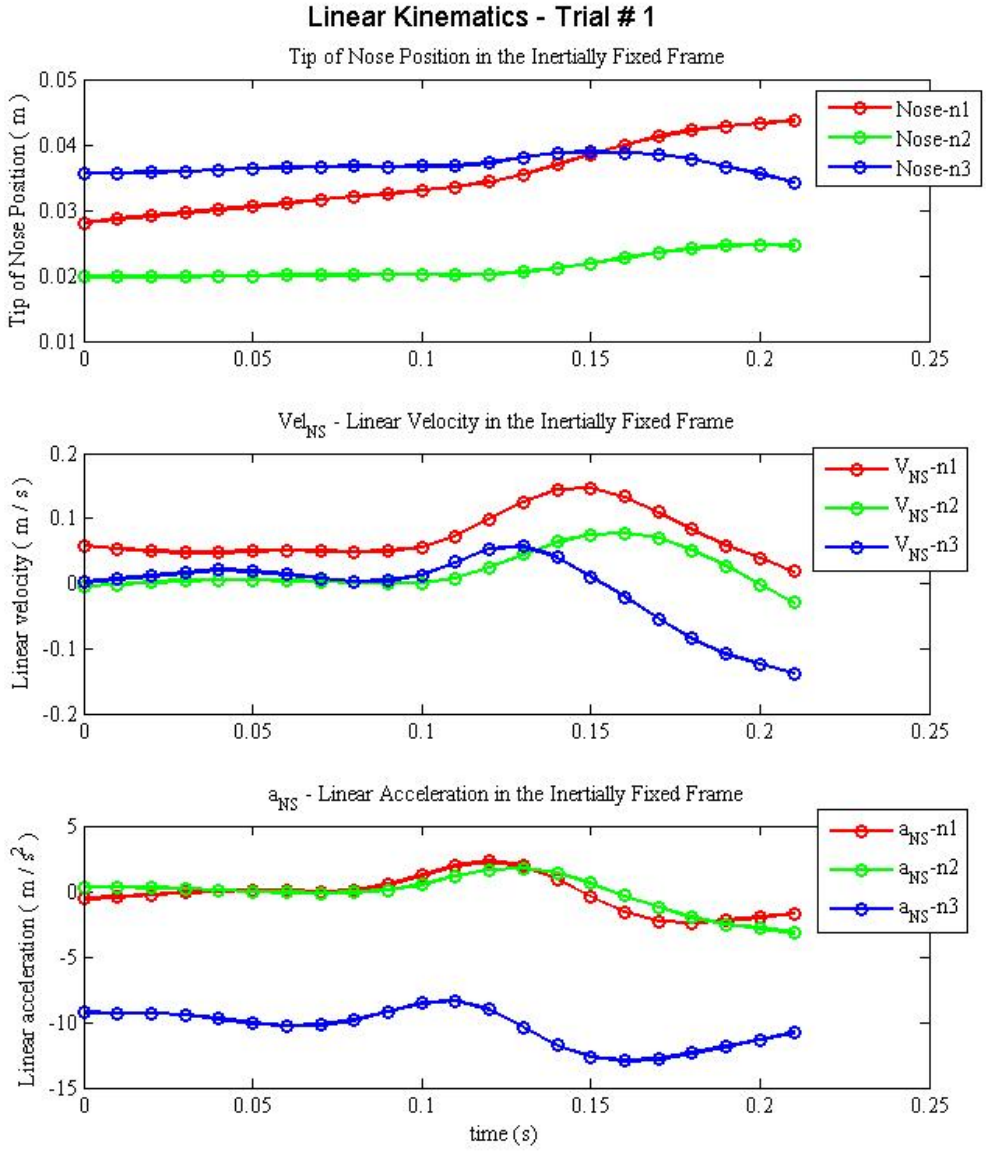

Figure 27: Linear Kinematics Trial #1

This graph shows the Linear Position, Velocity and Accelerations for the tip of the nose for feeding trial #1. These graphs include gravity acting in the minus n3 direction. There is a maximum acceleration magnitude of 13.073 m/s^2.

Linear (N-Frame)	
+X(n1)	Forward in the Tank
+Y(n2)	Left in the Tank
+Z(n3)	Up in the Tank

Position data collected during a feeding strike indicates a maximum acceleration at the utricle (including gravity) is 13.05 m/s^2 (see **Figure 28**) . There is a negligible (0.1-0.2 %) change in the maximum acceleration at the utricle, due to the angular motion of the head and position of the utricle (refer to **Figure 27** above). This change in acceleration would hardly be noticed by hair bundles on the utricle maculae because the maximum change in deformation of the OM would be less than 1 nanometer.

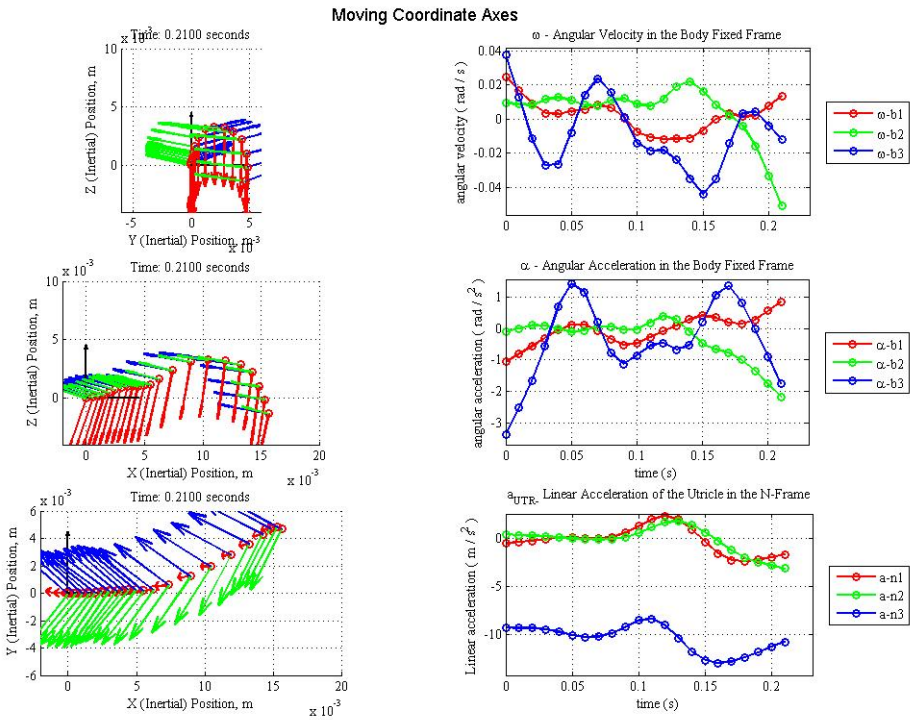

Figure 28: Position views, Angular Kinematics, & Acceleration at the utricle in the N-Frame for Trial #1

On the left, 3 different views (top to bottom : Front view, Side View, Top View) of the position of the nose marker and the body fixed coordinates attached to the nose with the tank coordinates as the fixed coordinate system.

On the right, angular velocity (in the B-frame), angular acceleration (in the B-frame), and linear acceleration at the utricle in the N-Frame based on position measurements from feeding Trial 1 and measurements from the μ-CT.

Linear (N-Frame)		Body Fixed Coordinates (B Frame)	
+X(n1)	Forward in the Tank	b1	Red
+Y(n2)	Left in the Tank	b2	Green
+Z(n3)	Up in the Tank	b3	Blue

4.3.4. Acceleration in the plane of the utricle

However, if orientation of the utricle is considered: pitch and roll approximately 24 and 6 degrees down, respectively, there is a shift in the magnitude of acceleration in the plane of the utricle (u1 & u2 in **Figure 29**) from the acceleration of the nose. The change in orientation of the utricle reduces the maximum acceleration from the nose by approximately 44 percent in this feeding strike (44.1%-trial 1, 28%-trial 2, 31.2%-trial 3).

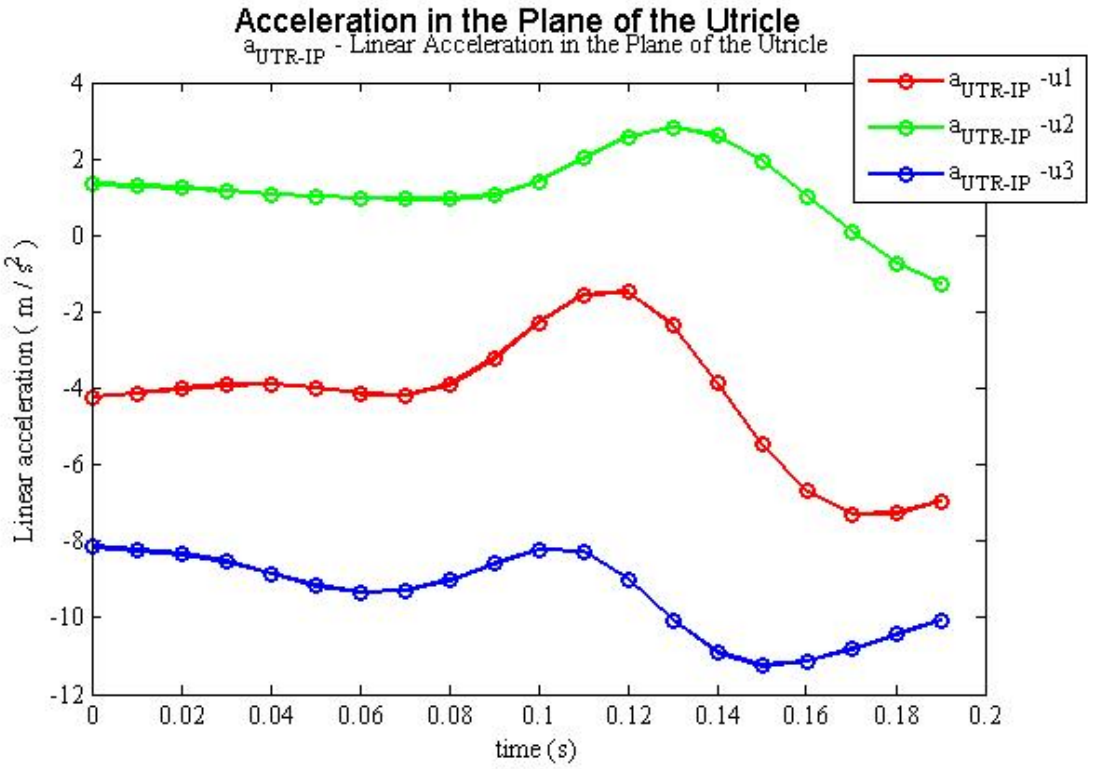

Figure 29: Acceleration in the plane of the utricle - Trial #1

Components of acceleration at the utricle (in the U-Frame) based on measurements from Trial 1.

Here:
u1 is the Anterior-Posterior Direction (+A)
u2 is the Medial-Lateral Direction (+Left)
u3 is the Perpendicular to plane of utricle (+ Dorsal)

In-plane acceleration is considered here because it is the in-plane components of gravitoinertial acceleration that will efficiently excite most of the hair bundles in the utricle OM (see Section 4.3.5, below). However, as the gravitoinertial acceleration vector changes position and magnitude in 3D space, the in-plane acceleration will also change position and magnitude. This idea is illustrated in **Figure 30.** The green arrow represents a gravitoinertial acceleration vector imparted to the utricle through movement of the head. It is centered at the COM of the OL. The blue arrow indicates the in-plane acceleration vector, a projection of the gravitoinertial acceleration vector into the plane of the utricle. The angle between the plane and the gravitoinertial acceleration vector and the plane is designated here as theta (θ). As the gravitoinertial acceleration vector changes position and magnitude in 3D space, the in-plane acceleration vector may also change position and magnitude (remaining in the macular plane). Additionally, if the utricle changes

orientation, while the gravitoinertial acceleration vector remains constant, then the in-plane acceleration may also change magnitude or position. This is why it is important to characterize the acceleration at the utricle, and in the plane of the utricle: because the orientation of the utricle may change the stimulus to the hair bundles.

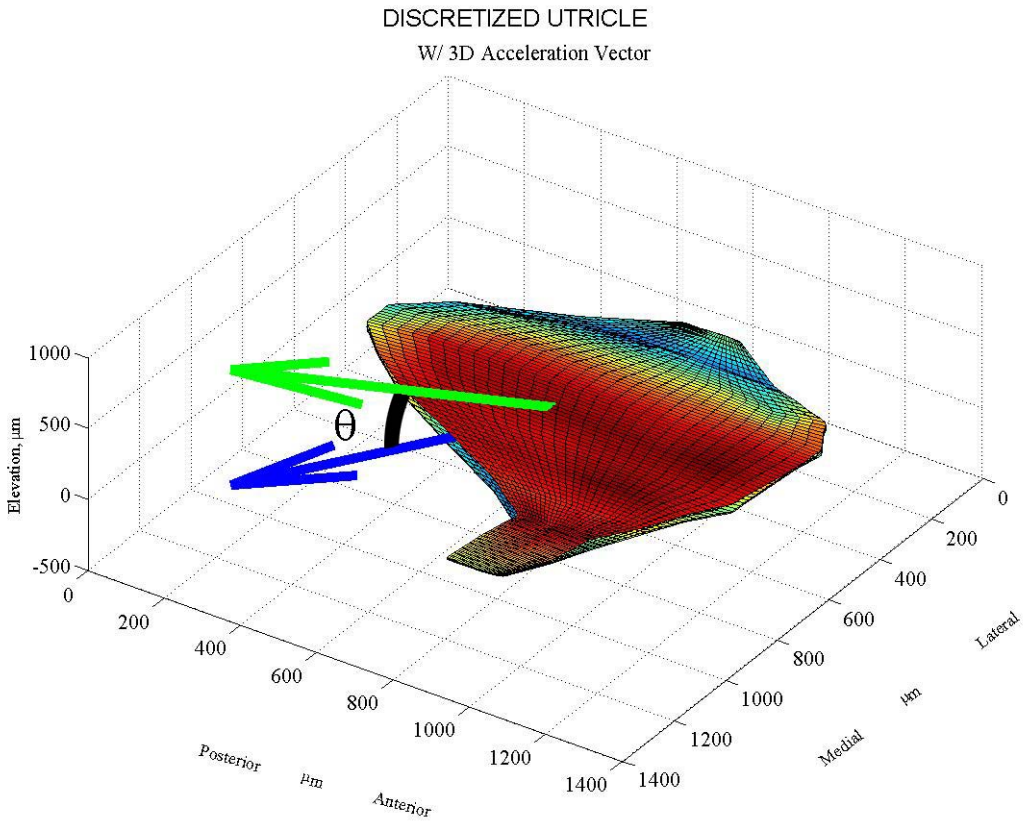

Figure 30: Utricle with 3D Acceleration Vector

This figure illustrates a fictitious gravitoinertial acceleration vector (green arrow) acting on the utricle OM (red-yellow-cyan). The important component of acceleration is the in-plane acceleration (blue arrow), at an angle (θ), relative to the gravitoinertial acceleration. In-plane acceleration will maximally stimulate the hair bundles in the utricle OM. As the gravitoinertial acceleration changes position and magnitude, so will position and magnitude of the in-plane acceleration. In addition, if the orientation of the utricle changes, while the gravitoinertial acceleration remains constant, the in-plane acceleration vector may also change.

4.3.5. Effects of Orientation on Static Mechanical Gain

The effect of orientation on static mechanical gain of the utricle considering a 1G load applied in 3D space to the utricle model is shown in **Figure 31**. Each line represents the average displacement at the CFL-CGL interface for the utricle model for a 1G excitation in a certain plane: starting in the plane of the maculae and then rotating about the pitch axis of the turtle head until the plane reaches a position perpendicular (90 deg) to the macular plane.

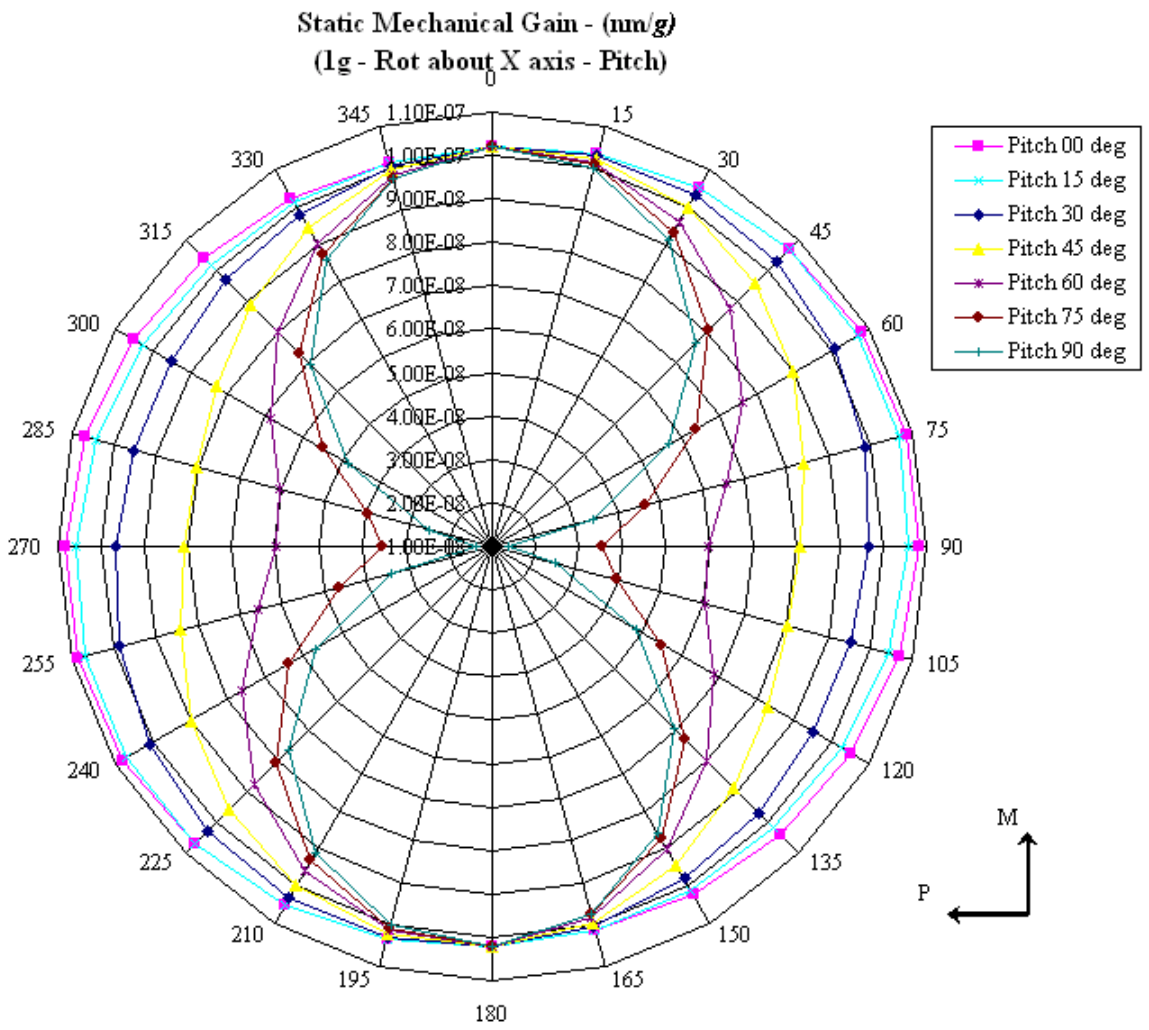

Figure 31: 3D Static Mechanical Gain Peanut In Different Pitch Planes

A plane is rotated in 15 degree increments about the pitch axis of the utricle. The utricle is then stimulated with a 1 g load at 15 degree increments, from 0-360 degrees in the rotated plane. Arrows indicate approximate medial (M) and posterior (P) directions.

The mechanical gain peanut subtly rotates from having a maximum mechanical gain around 75 (255) degrees when the pitch angle is zero degrees to having a maximum mechanical gain at 0 (180) degrees when the pitch angle is 90 degrees.

The maximum static mechanical gain of the utricle occurs when the utricle is oriented with the macular plane, parallel to the shear stimulus. As the plane of loading is rotated about the pitch axis, static mechanical gain clearly decreases overall. A more subtle change is the rotation of the static mechanical gain peanut as the loading plane approaches vertical (i.e.: pitch = 90 degrees). Thus, as the pitch angle of the loading plane approaches 90 degrees (or perpendicular to the maculae of the utricle) the maximum static mechanical gain, for that plane of loading, rotates towards the medial-lateral

position and the minimum rotates towards the dorsal-ventral direction. This indicates that the utricle is most effective transducing acceleration when the stimulus is closest to the plane of the organ.

4.4 Discussion

4.4.1. Implications of Utricle Orientation

From finite element models of the utricle, it has been determined that the most sensitive position (relative to earth horizontal motion) for a turtle to hold its head in order to maximally stimulate hair bundles in the utricle, is pitched up from rest approximately 24 degrees and rolled to the left or right approximately 6 degrees. This position would approximately align one of the turtle's utricle macula with earth horizontal.

It has been observed, with the red ear slider turtle, that they position themselves in the water such that their bodies are held buoyant, near the surface, and their heads are allowed to break the surface of the water at an angle between approximately 15 and 30 degrees, shown in Peterson and Ulinski (1979). In addition, their iris lines are held parallel to the surface of the water. This may be an optimal position for the utricles to be excited, maximizing vestibular-ocular reflexes controlling eye movements.

4.4.2. Implications of Utricle Position

Mean distances between organ Utricle OL COMs and kinematic measurement locations may be used to calculate acceleration imparted to the utricle OM during motion of the head (considering a rigid connection between the Jaw Hinge or Tip and the utricle position). **Equation 10**, along with the relative distances between organs and kinematic measurement locations, shown in **Table 11**, indicate that a red ear slider turtle's head must experience an angular acceleration on the order of 106 – 1535 rad/s^2 [2.6 (m/s) / 0.0246 (m) or 2.6 (m/s) /0.0017 (m)] or an angular velocity on the order of 10 – 39.1 rad/s in order for there to be a 20% (2.6 m/s^2) increase, on the magnitude of the nose tip acceleration, imparted to the utricle.

Table 11: Distance between Mean Positions of Utricle and Jaw Hinge
In CT fixed coordinates, the distance between the utricle and the tip of the nose are given here. These numbers must be rotated into the body fixed coordinated before cross products can easily be taken with ω and α.

CT Fixed Coordinates	AP (x) (mm)	LM (y) (mm)	DV (z) (mm)
Left Utricle – Tip of Nose	24.6 (Anterior)	-4.1 (Medial)	1.7 (Dorsal)
Right Utricle – Tip of Nose	24.8 (Anterior)	5.2 (Medial)	1.7 (Dorsal)

While this type of head acceleration may be observed in turtles, it is not observed in these recorded feeding habits. This calculated angular acceleration is beyond the capable range of angular acceleration and angular velocity of the turtle's head during these measured feeding strikes (see **Figure 28**).

This 20 percent increase on linear acceleration translates to about (9.81 m/s^2 ~ 100 nm) 20 nanometers of deflection in the utricle OM, which is within the operating range, but near the lower limits, of red ear slider turtle utricular hair bundles. This small stimulus could probably most effectively be detected by the striolar hair bundles They tend to be more sensitive to smaller changes in displacements (i.e. current vs. displacement curve is steeper for striolar bundles) (Nam et al. 2005a). Therefore, if a turtle could pitch its head with an angular velocity on the order of 10 rad/s (or angular acceleration ~106 rad/s^2), this motion could potentially increase the stimulus to hair bundles by approximately 20 nanometers. This stimulus would most likely be observed by the more sensitive striolar hair bundles.

4.4.3. Limitations of this study

The most obvious limitation of this study is that results are based on only one turtle head. A better representation of the turtle population could be shown with more turtles analyzed for position and orientation of their utricles. In addition, only 3 feeding trials were analyzed. More feeding trials would provide a better statistical representation of turtle behavior while feeding. However, the goal here was set out to establish the methods necessary for future studies in this area. This was accomplished.

CHAPTER 5. Conclusions

ABSTRACT

Previous models of otoconial membranes usually consider uniformly thick membrane layers with flat macular surfaces and a 2D or rectangular perimeter. This research quantifies the results of 3 different aspects of utricle modeling that may, at times, be overlooked: 3D Macular Curvature, Macular Perimeter and Varying OM layer thickness. Previous OM models ignore three dimensional aspects that may be important in understanding 1) the function of the organ, 2) how it works and 3) the reasons for its unique shape. Using static mechanical gain and natural frequencies, as metrics, several qualities of the utricle are observed to change the deformation characteristics within the OM, and thus the excitation of hair bundles. It is evident from these results that geometric (OM) structure and orientation play a significant role in the deformation of the utricle OM. These should definitely be considered in future models of OMs concerned with hair bundle excitation. Hair bundles play less of a role in the deformation of the utricle OM. However, this conclusion is not the same for the bullfrog saccule. Therefore, stiffness contribution of HBs should be measured before they are structurally eliminated from a model. Finally, utricle position in the head does not play a large role in the deformation of the utricle OM considering the data currently available. However, this conclusion could change analysis of more turtle heads and feeding strikes.

5.1 Macular Geometry & Layer Thickness Conclusions

5.1.1. Macular Perimeter

Adding macular perimeter to the OM models removes the geometric restriction placed on 2D models that forces the only physiologically meaningful OM displacements to be along an axis of symmetry. Thus, a 3D perimeter allows the OM models to displace based on natural geometric restrictions, providing insight into how geometry may influence hair bundle excitation. This change is manifest in a change in static mechanical gain of the organ in addition to a change in direction of the first two displacement mode shapes of the OM.

Coincidentally, due to linear modeling, the first two displacement modes line up with the extremes of the static mechanical gain. This is also the location in which there is a large concentration of hair bundles at the anterior and posterior ends of the striolar region. Although it is not yet clear if this is functionally significant, this result would not have been evident without explicitly including macular perimeter in the OM model.

5.1.2. Macular Curvature

Curvature of the macular surface adds stiffness to the utricle, as demonstrated by the increase in natural frequency of the organ. This stiffness change is also manifest in a reduced deflection in the OM sublayers, thereby reducing the stimulus applied to hair bundles in these layers. Therefore, OM models that do not accurately model the macular surfaces may inaccurately predict deflections applied to hair bundles. In addition, macular curvature is one of the features of the utricle whose purpose could be a fine tuning of the directions of the displacement modes and static mechanical gain.

5.1.3. Layer Thickness

Varying of layer thicknesses is most noticeable in the otoconial layer of the OM models. Redistributing of otoconia mass has been shown to effect static mechanical gain and directions of displacement modes. This variable may be another characteristic of the OM used to fine tune static mechanical gain and direction of displacement modes, in a similar fashion as the macular curvature.

The varying thickness of the column filament and compact gel layers are also observed to reduce the displacements in the striolar region of the utricle. This is hypothesized to be an explanation for functional differences between types of hair

bundles as striolar bundles have a smaller operating range (distance to full activation before saturation) (Nam et al. 2005a), and receive less displacement stimulus due to the thicker CFL and CGL in the striola.

5.2 Shear Stiffness Contribution Conclusions

Using two sets of models of the turtle utricle and the bullfrog saccule (Kondrachuk, 2000), shear stiffness contribution of hair bundles to displacement in the OM were determined. First a bullfrog saccule model was constructed based on the geometry and material properties provided in Kondrachuk 2000. Our methods for quantifying stiffness contribution were tested and confirmed against previously published results (Benser et al. 1993 & Kondrachuk, 2000). These methods were then used with the turtle utricle model.

5.2.1. Turtle Utricle hair bundles are too weak to dominate the stiffness of the CFL-HB complex

Contributing less than 3.25 percent to the shear stiffness of the CFL-HB complex, turtle utricle hair bundles are not stiff enough to dominate the CFL-HB complex as they do in the bullfrog saccule. However, there is somewhat of a dichotomy between efficient energy transduction from the OM to hair bundles, and physiologically meaningful deflections transferred to hair bundles. A lower modulus in the CFL-HB complex translates to more efficient transductions between hair bundles and OM, as the natural frequencies between HBs (200 – 800 Hz (Denk et al. 1989)) and the OM (271 Hz) begin to converge. However, a lower OM natural frequency translates to larger deflections in the OM. These larger OM displacements (~ on the order of μm's) may impart damaging displacements to some of the hair bundles within the OM. This helps confirm that the modulus of the turtle utricle CFL-HB complex should be on the order of 250 Pa.

5.2.2. Turtle Utricle Material properties

Recall that the material properties for any otoconial organ's OM layers have not yet explicitly been determined (for any species). Instead, they have been inferred through models (Kondrachuk, 2000). Additionally, material properties OM layers for any of the otoconial organs of a turtle have not yet been determined. To our knowledge only a bullfrog saccule has explicitly been tested and subsequently modeled to determine the

material properties of the OM layers. In the future, a similar test may be performed and verified with modeling efforts to converge on a solution to the material properties of the turtle utricle.

5.3 Position & Orientation Conclusions

5.3.1. Position Effects

Position of the OM within the skull may effect the stimulus that the utricle can detect. Relative to the back of the neck, about which the turtle may bend its head, the utricle is positioned such that large angular accelerations would be necessary to impart significant changes to linear accelerations at the utricle. These accelerations were measured and are beyond the currently measured range for our species of turtle. However this conclusion may change with more data samples of turtle feeding and otoconial organ position.

5.3.2. Orientation Effects

The effect of orientation of the OM on the static mechanical gain of the utricle is a change in the magnitude and direction of a gravitational stimulus supplied to the OM that can effectively stimulate hair bundles. Orientation may also play a role in the behavior of the turtle as the urticle's most sensitive position to horizontal stimulus is when the turtle's head is pitched up 24 degrees from horizontal. This closely aligns the macular plane of the utricle with earth's horizontal plane – there is still some lateral roll of the macular plane. Thus the turtle would be most sensitive to any stimulus, via ground or water transmission, in earth's horizontal plane. This may be the reason for observations of the turtle with its head pitched up, at approximately 30 degrees from the water's surface or when on land (i.e.: startle response or looking for/trying to detect food).

5.4 Final Thoughts & Future Directions

This research is unique in how it uses finite element methods to study how utricle structure may effect our interpretations of its function. Using natural frequencies and static mechanical gain, the effects of changing OM geometry is quantified. This research is the first to consider the curvature of the whole macular surface, varying OM layer thickness and macular perimeter of the utricle and their effects on the stimulus of hair

bundles. These OM models reveal that the utricle has directions of maximum and minimum static mechanical gain, which are aligned with the first two deflection mode shapes. They also illustrate that minute changes in the structure of the organ may act as a tuning mechanism for the directional sensitivity. One and two dimensional OM models may overlook these aspects of OMs.

Additionally, we use novel methods to quantify shear stiffness contributions of hair bundles to the underlying layers of the OM. Previous authors assume the stiffness of hair bundles to be implicitly included in their models (Kondrachuk 2000; Benser et al. 1993; Grant 1994). However, this work is the first to use finite elements with *implicitly* and *explicitly* modeled hair bundles (with a physiologically accurate utricle model), in order to determine the contribution of hair bundles to the OM shear layer stiffness.

This study is unique in its use of finite element methods in conjunction with computed tomography in order to quantify how position and orientation may effect our interpretations of the utricle function. Computed tomography indicates that the utricle is pitched down 24 degrees from stereotaxic horizontal. It is also evident from the results that the utricle is in its most sensitive position when the macular surface is close to parallel with the stimulus. This may explain the behavior of the turtle, when floating or startled (holding it's head at ~30 degrees to earth horizontal).

Finally, the ground work has been established for understanding which variables must be considered in future OM models and how these variables may affect experimental and modeling results and therefore our understanding of how OMs work. Careful consideration for the intricacies of otocoinal membrane structure and its layered construction may lead to better definitions of displacement and force boundary conditions applied to hair bundles. This may, in turn, lead to a better understanding of the reasons for the otoconial membrane's unique shape and construction and its role in the activation of hair bundles.

In the future, this model could be expanded to include damping and time varying loads to compare displacement results with experimental dynamic tests allowing for the characterization of material properties specific to this species and organ. Understanding how material properties change with respect to the frequency domain will shine more light on to the questions in the research: 1) Why does the organ have a unique shape and

structure? 2) Why are hair bundles morphologically diverse and seemingly organized on the maculae with great care? and 3) How do natural movements of a turtle head stimulate hair bundles in the utricle?

References

(2006). "Strategic Plan - National Institute on Deafness and Other Communication Disorders - FY 2006-2008." <www.nidcd.nih.gov/about/plans/strategic> (11/30, 2007).

(2007). "Statistics: How Many People Have Vestibular Disorders?" <www.vestibular.org/vestibular-disorders/statistics.php> (12/3, 2007).

Ashcroft, D. W., and Hallpike, C. S. (1934). "On the function of the saccule." *J Laryng.*, 49, 450-458.

Baird, R. A. (1994). "Comparative transduction mechanisms of hair cells in the bullfrog utriculus. I. Responses to intracellular current." *Journal of neurophysiology*, 71(2), 666-684.

Benser, M. E., Issa, N. P., and Hudspeth, A. J. (1993). "Hair-bundle stiffness dominates the elastic reactance to otolithic-membrane shear." *Hearing research*, 68(2), 243-252.

Blob, R. W. (2007). "Turtle nose is the most accurately digitized point." J. L. Davis, ed.

Braemer, W., and Braemer, H. (1958). "Orientation of Fish to Gravity." *Limnology and Oceanorgraphy*, 3(4), 362-372.

Brichta, A. M., Acuna, D. L., and Peterson, E. H. (1988). "Planar relations of semicircular canals in awake, resting turtles, Pseudemys scripta." *Brain, behavior and evolution*, 32(4), 236-245.

Carlstrom, D. A. (1963). "Crystallographic study of vertebrate otoliths." *The Biological Bulliten*(125), 441-463.

Corey, D. P., and Hudspeth, A. J. (1979). "Response latency of vertebrate hair cells." *Biophysical journal*, 26(3), 499-506.

Corey, D. P., and Hudspeth, A. J. (1983a). "Analysis of the microphonic potential of the bullfrog's sacculus." *J Neurosci*, 3(5), 942-961.

Corey, D. P., and Hudspeth, A. J. (1983b). "Kinetics of the receptor current in bullfrog saccular hair cells." *J Neurosci*, 3(5), 962-976.

Corvera, J., Hallpike, C. S., and Schuster, E. H. (1958). "A new method for the anatomical reconstruction of the human macular planes." *Acta oto-laryngologica*, 49(1), 4-16.

Crawford, A. C., Evans, M. G., and Fettiplace, R. (1991). "The actions of calcium on the mechano-electrical transducer current of turtle hair cells." *The Journal of physiology*, 434, 369-398.

Crawford, A. C., and Fettiplace, R. (1985). "The mechanical properties of ciliary bundles of turtle cochlear hair cells." *The Journal of physiology*, 364, 359-379.

Curthoys, I. S., Betts, G. A., Burgess, A. M., MacDougall, H. G., Cartwright, A. D., and Halmagyi, G. M. (1999). "The planes of the utricular and saccular maculae of the guinea pig." *Annals of the New York Academy of Sciences*, 871, 27-34.

Davis, J. L., and Grant, J. W. (Year). "Effects of Otoconia Thickness and Overall Curvature on Utricular Otolith Dynamics." *Association of Research in Otolaryngology*, Daytona, FL.

Davis, J. L., Xue, J., Peterson, E. H., and Grant, J. W. (2007). "Layer Thickness and Curvature Effects on Utricle Deflection in the Red Ear Slider Turtle: Static & Dynamic Analysis." *Submitted to Journal of Vestibular Research*.

De Vries, H. (1951). "The mechanics of the labyrinth otoliths." *Acta oto-laryngologica*, 38(3), 262-273.

Denk, W., Webb, W. W., and Hudspeth, A. J. (1989). "Mechanical properties of sensory hair bundles are reflected in their Brownian motion measured with a laser differential interferometer." *Proceedings of the National Academy of Sciences of the United States of America*, 86(14), 5371-5375.

Edge, R. M., Evans, B. N., Pearce, M., Richter, C. P., Hu, X., and Dallos, P. (1998). "Morphology of the unfixed cochlea." *Hearing research*, 124(1-2), 1-16.

Enger, P. S., Hawkins, A. D., Sand, O., and Chapman, C. J. (1973). "Directional sensitivity of saccular microphonic potentials in the haddock." *The Journal of experimental biology*, 59(2), 425-433.

Fay, R. R. (1984). "The goldfish ear codes the axis of acoustic particle motion in three dimensions." *Science*, 225(4665), 951-954.

Fay, R. R., and Edds-Walton, P. L. (1997). "Directional response properties of saccular afferents of the toadfish, Opsanus tau." *Hearing research*, 111(1-2), 1-21.

Flock, A., and Strelioff, D. (1984). "Graded and nonlinear mechanical properties of sensory hairs in the mammalian hearing organ." *Nature*, 310(5978), 597-599.

Fontilla, M. F., and Peterson, E. H. (2000). "Kinocilia heights on utricular hair cells." *Hearing research*, 145(1-2), 8-16.

Freeman, D. M., Abnet, C. C., Hemmert, W., Tsai, B. S., and Weiss, T. F. (2003). "Dynamic Material Properties of the Tectorial Membrane: A summary." *Hearing research*, 180, 1-10.

Freeman, D. M., Cotanche, D. A., Ehsani, F., and Weiss, T. F. (1994). "The osmotic response of the isolated tectorial membrane of the chick to isosmotic solutions: effect of Na+, K+, and Ca2+ concentration." *Hearing research*, 79(1-2), 197-215.

Freeman, D. M., Hattangadi, S. M., and Weiss, T. F. (1997). "Osmotic responses of the isolated mouse tectorial membrane to changes in pH." *Auditory Neuroscience*(3), 363-375.

Freeman, D. M., Hendrix, D. K., Shah, D., Fan, L. F., and Weiss, T. F. (1993). "Effect of lymph composition on an in vitro preparation of the alligator lizard cochlea." *Hearing research*, 65(1-2), 83-98.

Goldberg, J. M., Desmadryl, G., Baird, R. A., and Fernandez, C. (1990). "The vestibular nerve of the chinchilla. IV. Discharge properties of utricular afferents." *Journal of neurophysiology*, 63(4), 781-790.

Grant, J. W., and Best, W. A. (1986). "Mechanics of the otolith organ--dynamic response." *Annals of biomedical engineering*, 14(3), 241-256.

Grant, J. W., Best, W. A., and LoNigro, R. (1984). "Governing equations of motion for the otolith organs and their response to a step change in velocity of the skull." *Journal of biomechanical engineering*, 106(4), 302-308.

Grant, J. W., and Cotton, J. R. (1990). "A model for otolith dynamic response with a viscoelastic gel layer." *J Vestib Res*, 1(2), 139-151.

Grant, J. W., Huang, C. C., and Cotton, J. R. (1994). "Theoretical mechanical frequency response of the otolithic organs." *J Vestib Res*, 4(2), 137-151.

Grant, J. W., Spoon, C., and Nam, J. H. (2007). "Experimental and Computational Analysis of Hair Bundle Mechanics at Different Macular Locations in the Turtle Utricle." *Association for the Research in Otolaryngology*, 13, 947.

Grant, W., and Best, W. (1987). "Otolith-organ mechanics: lumped parameter model and dynamic response." *Aviation, space, and environmental medicine*, 58(10), 970-976.

Highstein, S. M., Fay, R. R., and Popper, A. N., eds. (2004). *The Vestibular System*, Springer, New York.

Hillman, D. E., and Lewis, E. R. (1971). "Morphological basis for a mechanical linkage in otolithic receptor transduction in the frog." *Science*, 174(7), 416-419.

Howard, J., and Ashmore, J. F. (1986). "Stiffness of sensory hair bundles in the sacculus of the frog." *Hearing research*, 23(1), 93-104.

Hudetz, W. J. (1973). "A computer simulation of the otolith membrane." *Computers in biology and medicine*, 3(4), 355-369.

Jaeger, R., and Haslwanter, T. (2004). "Otolith responses to dynamical stimuli: results of a numerical investigation." *Biological cybernetics*, 90(3), 165-175.

Jaeger, R., Takagi, A., and Haslwanter, T. (2002). "Modeling the relation between head orientations and otolith responses in humans." *Hearing research*, 173(1-2), 29-42.

Jorgensen, J. M. (1974). "The sensory Epithelia of the Inner Ear of Two Turtles, *Testudo graeca* L. & *Pseudemys scripta* (Schoepff)." *Acta Zoologica*, 55, 289-298.

Kachar, B., Parakkal, M., and Fex, J. (1990). "Structural basis for mechanical transduction in the frog vestibular sensory apparatus: I. The otolithic membrane." *Hearing research*, 45(3), 179-190.

Kondrachuk, A. V. (2000). "Computer simulation of the mechanical stimulation of the saccular membrane of bullfrog." *Hearing research*, 143(1-2), 130-138.

Kondrachuk, A. V. (2001a). "Finite element modeling of the 3D otolith structure." *J Vestib Res*, 11(1), 13-32.

Kondrachuk, A. V. (2001b). "Models of the dynamics of otolithic membrane and hair cell bundle mechanics." *J Vestib Res*, 11(1), 33-42.

Kondrachuk, A. V., and Ross, M. D. (1997). "Modeling of the otolith structure behavior under static loads (internal forces and endolymphmatic pressure)." In: *Association for Research in Otolaryngology - Midwinter meeting*.

Lewis, E. R., Leverenz, E. L., and Bialek, W. S. (1985). *The vertebrate inner ear*, CRC Press, Boca Raton, Fla.

Lowenstein, O., and Roberts, T. D. (1949). "The equilibrium function of the otolith organs of the thornback ray (Raja clavata)." *The Journal of physiology*, 110(3-4), 392-415.

Lowenstein, O., and Saunders, R. D. (1975). "Otolith-controlled responses from the first-order neurons of the labyrinth of the bullfrog (Rana catesbeiana) to changes in linear acceleration." *Proceedings of the Royal Society of London. Series B, Containing papers of a Biological character*, 191(1105), 475-505.

Meirovitch, L. (1985). *Introduction to dynamics and control*, Wiley, New York.

Meirovitch, L. (1986). *Elements of vibration analysis*, 2nd Ed., McGraw-Hill, New York.

Money, K. E., and Correia, M. J. (1972). "The vestibular system of the owl." *Comparative biochemistry and physiology*, 42(2), 353-358.

Moravec, W. J., and Peterson, E. H. (2004). "Differences between stereocilia numbers on type I and type II vestibular hair cells." *Journal of neurophysiology*, 92(5), 3153-3160.

Nam, J. H., Cotton, J. R., and Grant, J. W. (2005a). "A Computational Study of the Effect of Hair Bundle Shape and Loading Condition on the Mechanosensory Response." In: *Society For Neuroscience*, 47.43.

Nam, J. H., Cotton, J. R., and Grant, J. W. (2005b). "Effect of fluid forcing on vestibular hair bundles." *J Vestib Res*, 15(5-6), 263-278.

Nam, J. H., Cotton, J. R., and Grant, W. (2007). "A virtual hair cell, I: addition of gating spring theory into a 3-D bundle mechanical model." *Biophysical journal*, 92(6), 1918-1928.

Nam, J. H., Cotton, J. R., Peterson, E. H., and Grant, W. (2006). "Mechanical properties and consequences of stereocilia and extracellular links in vestibular hair bundles." *Biophysical journal*, 90(8), 2786-2795.

NIDCD, N. I. H.-. (2007). "Balance Disorders." <www.nidcd.nih.gov/health/balance/balance_disorders.asp> (2007, 12/2).

Peterson, E. H. (2004). "Percentage of Striolar Hair Bundles in Lateral-Meidal Transect of Turtle Utricle: Personal Communication." J. L. Davis, ed.

Peterson, E. H., and Ulinski, P. S. (1979). "Quantitative studies of retinal ganglion cells in a turtle, Pseudemys scripta elegans. I. Number and distribution of ganglion cells." *The Journal of comparative neurology*, 186(1), 17-42.

Pote, K. G., Weber, C. H., and Kretsinger, R. H. (1993). "Inferred protein content and distribution from density measurements of calcitic and aragonitic otoconia." *Hearing research*, 66(2), 225-232.

Reddy, J. N. (1984). *An introduction to the finite element method*, McGraw-Hill, New York.

Ross, M. D., Komorowski, T. E., Donovan, K. M., and Pote, K. G. (1987). "The suprastructure of the saccular macula." *Acta oto-laryngologica*, 103(1-2), 56-63.

Rowe, M. H., and Peterson, E. H. (2006). "Autocorrelation analysis of hair bundle structure in the utricle." *Journal of neurophysiology*.

Severinsen, S. A., Jorgensen, J. M., and Nyengaard, J. R. (2003). "Structure and Growth of the Utricular Macula in the Inner Ear of the Slider Turtle *Trachemys Scripta*." *Journal of the Association for Research in Otolaryngology*, 4, 505-520.

Shah, D. M., Freeman, D. M., and Weiss, T. F. (1995). "The osmotic response of the isolated, unfixed mouse tectorial membrane to isosmotic solutions: effect of Na+, K+, and Ca2+ concentration." *Hearing research*, 87(1-2), 187-207.

Silber, J., Cotton, J., Nam, J. H., Peterson, E. H., and Grant, W. (2004). "Computational models of hair cell bundle mechanics: III. 3-D utricular bundles." *Hearing research*, 197(1-2), 112-130.

Spoon, C., Moravec, W. J., Peterson, E. H., and Grant, J. W. (2005). "Bundle Mechanics Depends on Bundle Structure." In: *Association for Research in Otolaryngology - Midwinter Research Meeting*.

Strelioff, D., and Flock, A. (1984). "Stiffness of sensory-cell hair bundles in the isolated guinea pig cochlea." *Hearing research*, 15(1), 19-28.

Tribukait, A., and Rosenhall, U. (2001). "Directional sensitivity of the human macula utriculi based on morphological characteristics." *Audiology & neuro-otology*, 6(2), 98-107.

Trincker, D. (1962). "The Transformation of Mechanical Stimulus into Nervous Excitation by Labyrinthine Receptors." *Soc. Exp. Biol. Symp.* , 16, 289-316.

Walker, J. A. (1998). "Estimating Velocities and Accelerations of Animal Locomotion: A Simulation Experiment Comparing Numerical Differentiation Algorithms." *Journal of Experimental Biologu*, 201, 981-995.

Wilson, V. J., and Melvill Jones, G. (1979). *Mammalian vestibular physiology*, Plenum Press, New York.

Xue, J., and Peterson, E. H. (2002). "Structure of Otolithic Membranes in Utricular Striola." In: *Association for the Research in Otolaryngology - Midwinter Meeting*.

Xue, J., and Peterson, E. H. (2003). "Spatial Patterns in the Structure of Otolithic Membranes." In: *Association for the Research in Otolaryngology*.

Xue, J., and Peterson, E. H. (2006). "Hair bundle heights in the utricle: differences between macular locations and hair cell types." *Journal of neurophysiology*, 95(1), 171-186.

Appendix A – Model Convergence

FE Models – Maximum Displacement in 3D Utricle Models –Convergence

FC3D	1g x	
Mesh	Max. Disp.	% Diff
# Elem/vol	nm	
1	131.49	
8	131.77	0.21
27 (9)	131.89	0.09

FV3D	1g x	
Mesh	Max. Disp.	% Diff
# Elem/vol	nm	
1	130.22	
8	130.40	0.14
27(9)	130.48	0.06

CC3D	1g x	
Mesh	Max. Disp.	% Diff
# Elem/vol	nm	
1	109.76	
8	110.17	0.37
27 (9)	110.36	0.17

CV3D	1g x	
Mesh	Max. Disp.	% Diff
# Elem/vol	nm	
1	106.09	
8	105.48	-0.57
27(9)	105.52	0.038

FE Models – Maximum Displacement in 2D Utricle Models –Convergence

FC2D	1g x	
Mesh	Max. Disp.	% Diff
# Elem/vol	nm	
1	132.72	
8	132.84	0.09
27	132.88	0.03

FV2D	1g x	
Mesh	Max. Disp.	% Diff
# Elem/vol	nm	
1	134.83	
8	134.86	0.02
27	134.91	0.04

CC2D	1g x	
Mesh	Max. Disp.	% Diff
# Elem/vol	nm	
1	124.69	
8	125.07	0.31
27	125.21	0.11

CV2D	1g x	
Mesh	Max. Disp.	% Diff
# Elem/vol	nm	
1	126.32	
8	126.99	0.53
27	127.12	0.10

FE Models Natural Frequencies Convergence Data

Models were converged using an increased mesh size and two formulations of mass matrices. Consistent (C) and Lumped (L) mass formulations converge to the analytical solution from above and below respectively. Thus using both mass matrix formulations, the analytical solution may be bracketed and the mesh converged to a point necessary for accurate results.

8C meshes were used in reporting the results.

3D Utricle Models – Frequency Convergence

FC3D	ω_1	ω_2	ω_3
Mesh			
# Elem/vol	Hz	Hz	Hz
1 C	1397.47	1397.86	1399.55
8 C	1396.06	1396.7	1399.1
8 L	1394.62	1395.46	1397.6
1 L	1391.44	1392.89	1393.89

FV3D	ω_1	ω_2	ω_3
Mesh			
# Elem/vol	Hz	Hz	Hz
1 C	1378.09	1425.91	1743.78
8 C	1376.84	1425.05	1743.32
8 L	1375.57	1423.78	1740.43
1 L	1373.01	1420.84	1732.32

CC3D	ω_1	ω_2	ω_3
Mesh			
# Elem/vol	Hz	Hz	Hz
1 C	1519.33	1577.95	1642.26
8 C	1515.06	1569.84	1631.94
8 L	1513.57	1571.62	1634.07
1 L	1513.41	1568.24	1629.87

CV3D	ω_1	ω_2	ω_3
Mesh			
# Elem/vol	Hz	Hz	Hz
1 C	1537.1	1598.5	1994.7
8 C	1530.2	1591.6	1984.9
8 L	1531.3	1592.1	1981.3
1 L	1528.7	1590	1980.6

Quasi-2D Utricle Models – Frequency Convergence

Highlighted in green are the frequencies that correspond to displacement along the LM transect. This is the only mode that is significant in these Quasi-2D models because of their geometry.

FC2D	ω_1	ω_2	ω_3
Mesh			
# Elem/vol	Hz	Hz	Hz
1 C	1389.1	1390.5	1390.6
8 C	1387.9	1389.6	1389.76
8 L	1382.9	1383.7	1384.7
1 L	1367.3	1369.3	1370.6

FV2D	ω_1	ω_2	ω_3
Mesh			
# Elem/vol	Hz	Hz	Hz
1 C	1370.47	1378.39	1711.98
8 C	1369.08	1377.9	1710.09
8 L	1364.25	1373.05	1699.57
1 L	1351.45	1359.35	1670.89

CC2D	ω_1	ω_2	ω_3
Mesh			
# Elem/vol	Hz	Hz	Hz
1 C	1401.47	1417.08	1440.94
8 C	1400.06	1414.7	1436.09
8 L	1394.9	1408.74	1430.69
1 L	1381.12	1393.7	1419.84

CV2D	ω_1	ω_2	ω_3
Mesh			
# Elem/vol	Hz	Hz	Hz
1 C	1384.19	1431.13	1748.57
8 C	1382.79	1426.88	1745
8 L	1377.89	1421.7	1734.23
1 L	1364.89	1410.9	1706.59

FE Models with Hair Bundles – Frequency Convergence

Turtle Utricle with Hair Bundles Model

CV3D-Beams	ω_1	ω_2	ω_3
Mesh			
# Elem/beam	Hz	Hz	Hz
1	271.67	280.62	396.77
3	271.459	280.413	396.197
5	272.559	281.58	398.165

Converged w/ E-beam Striola = 30.13 kPa &
E-beam MES = 23.37 kPa

Bullfrog Saccule with Hair Bundles Model – Based on Kondrachuk, 2000

FC2D-Beams	ω_1	ω_2	ω_3
Mesh			
# Elem/beam	Hz	Hz	Hz
1	1170.87	1171.74	1228.57
3	1170.86	1171.73	1228.55
5	1170.86	1171.74	1228.56

Converged w/ E-beam = 426.85 kPa

Appendix B – Angular Kinematics

From Scott Hendricks Advanced Dynamics Notes.

The first step in determining the angular kinematics of rigid body motion is determining the relation between the Newtonian fixed (N) frame and a body fixed (B) frame. This relation is a rotation matrix [C].

$$\begin{Bmatrix} b_1 \\ b_2 \\ b_3 \end{Bmatrix} = \begin{bmatrix} C_{11} & C_{12} & C_{13} \\ C_{21} & C_{22} & C_{23} \\ C_{31} & C_{32} & C_{33} \end{bmatrix} \begin{Bmatrix} n_1 \\ n_2 \\ n_3 \end{Bmatrix} \quad \text{B1}$$

Equation B1: N-B Rotation

Now, if the angular kinematics during the motion of a rigid body is desired, start by finding the rate of change of a left hand side of Equation B1. The time derivative of the b-vector may be written as:

$$\frac{d}{dt} b_i = \dot{b}_i + {}^N\omega^B \times b_i \quad \text{B2}$$

Equation B2: Derivative of b-vector

But since the b-vectors are unit vectors, $\dot{b}_i = 0$. The angular velocity vector may be written in the B–frame, the cross product becomes routine. Therefore what remains is:

$$\frac{d}{dt} b_i = {}^N\omega^B \times b_i = (\omega_1 b_1 + \omega_2 b_2 + \omega_3 b_3) \times b_i \quad \text{B3}$$

Equation B3: Derivative of b-vector with angular velocity in B–frame

This can be re-written in matrix form:

$$\frac{d}{dt}\begin{Bmatrix} b_1 \\ b_2 \\ b_3 \end{Bmatrix} = \begin{bmatrix} 0 & -\omega_3 & \omega_2 \\ \omega_3 & 0 & -\omega_1 \\ -\omega_2 & \omega_1 & 0 \end{bmatrix} \begin{Bmatrix} b_1 \\ b_2 \\ b_3 \end{Bmatrix} = -\left[\tilde{\omega}\right] \{b_i\} = -\left[\tilde{\omega}\right] [C] \{n_i\} \quad \text{B4}$$

Equation B4: Derivative of b-vector with angular velocity in N–frame

Next, the right hand side of equation B1 is considered. Taking the derivative of the $[C] \{n_i\}$ term and noting that the n-vectors do not change length or position, the only part that has a time derivative is [C]:

$$\frac{d}{dt}\left\{\begin{bmatrix} C_{11} & C_{12} & C_{13} \\ C_{21} & C_{22} & C_{23} \\ C_{31} & C_{32} & C_{33} \end{bmatrix} \begin{Bmatrix} n_1 \\ n_2 \\ n_3 \end{Bmatrix}\right\} = \left[\dot{C}\right] \{n_i\} \quad \text{B5}$$

Equation B5: Derivative rotation matrix and n-vector

Thus equation B1 may be rewritten as:

$$-\left[\tilde{\omega}\right] [C] \{n_i\} = \left[\dot{C}\right] \{n_i\} \quad \text{B6}$$

Equation B6: Derivative of b-vector rewritten in term of angular velocities

Therefore, in order to solve for the angular velocities (referenced to the B-Frame) equation B6 may be rewritten as (shown below):

$$\begin{Bmatrix} \dot{C}_{11} \\ \dot{C}_{12} \\ \dot{C}_{13} \\ \dot{C}_{21} \\ \dot{C}_{22} \\ \dot{C}_{23} \\ \dot{C}_{31} \\ \dot{C}_{32} \\ \dot{C}_{33} \end{Bmatrix} = \begin{bmatrix} 0 & -C_{31} & C_{21} \\ 0 & -C_{32} & C_{22} \\ 0 & -C_{33} & C_{23} \\ C_{31} & 0 & -C_{11} \\ C_{32} & 0 & -C_{12} \\ C_{33} & 0 & -C_{13} \\ -C_{21} & C_{11} & 0 \\ -C_{22} & C_{12} & 0 \\ -C_{23} & C_{13} & 0 \end{bmatrix} \begin{Bmatrix} \omega_1 \\ \omega_2 \\ \omega_3 \end{Bmatrix} \quad \text{B7}$$

Equation B7: Solve for Angular Velocities

Angular accelerations are time derivatives of the angular velocities and will also be referenced to the B-frame. Thus, the angular velocities and accelerations (about the body fixed coordinates) for a particular time series may be solved for using this set of equations. Therefore it is necessary to have enough information to determine the rotation matrix between the B-Frame and the N-Frame at every point in the time series in order to use these methods.

Appendix C – Utricle Acceleration

In the following figures the N-Frame is a Newtonian Fixed Frame whose unit vectors are (n1, n2, n3) corresponding to X,Y, and Z in the graphs.

Newtonian (N) Frame	
+X(n1)	Forward in the Tank
+Y(n2)	Left in the Tank
+Z(n3)	Up in the Tank

The body fixed frame (or B-Frame) is indicated with unit vectors (b1, b2, b3).
The b1 vector is determined as the vector between the nose and the tip of the jaw.
The b3 vector is then determined as the cross product between the b1 vector and a vector between the nose and jaw hinge marker.
Finally the b2 vector is determined by crossing the b3 vector into the b1.

Body Fixed (B) Frame	
b1	Nose to Jaw Tip
b2	b3 X b1
b3	Normal to plane of marker points

Although not directly used in the kinematic analysis, the CT fixed reference frame is used as an intermediate step to get from the body fixed coordinates to the utricle fixed coordinates.

CT Fixed (C) Frame	
c1	Anterior
c2	Left
c3	Dorsal

Finally, the utricle fixed frame (U-Frame) is indicated with unit vectors (u1, u2, u3)
The u1 vector is in the anterior-posterior direction (+ Anterior).
The u2 vector is in the lateral-medial direction (+ Left).
The u3 vector is out of the plane of the utricle (+ Dorsal).

Utricle Fixed (U) Frame	
u1	Anterior
u2	+ Left
u3	Out of plane

The results of 3 feeding trials were analyzed. Figures of trial #1 data are in the text. Figures of trials 2 and 3 are below.

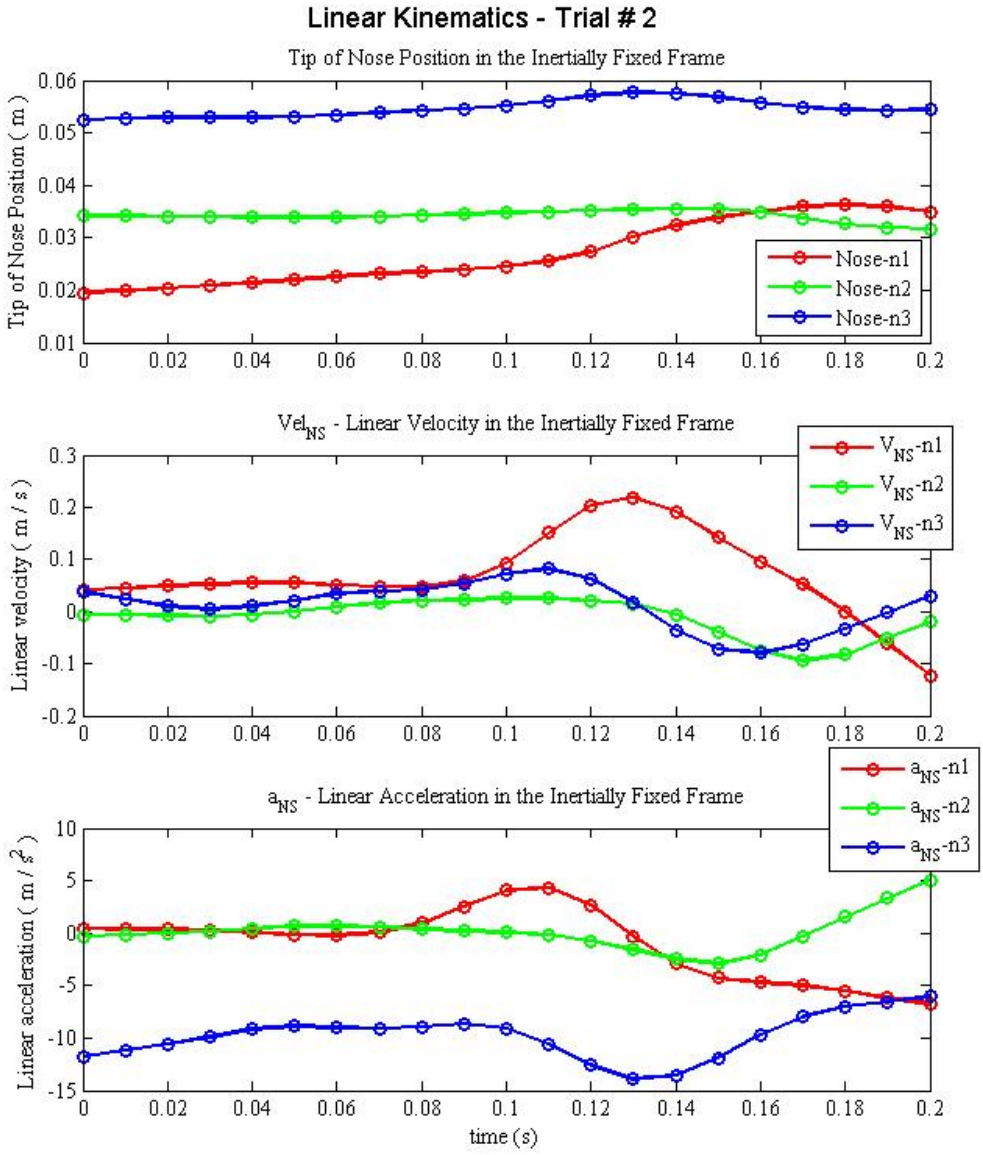

Figure C1: Linear Kinematics Trial #2

This graph shows the Linear Position, Velocity and Accelerations for the tip of the nose for feeding trial #2. These graphs include gravity acting in the minus n3 direction. There is a maximum acceleration magnitude of 13.073 m/s^2.

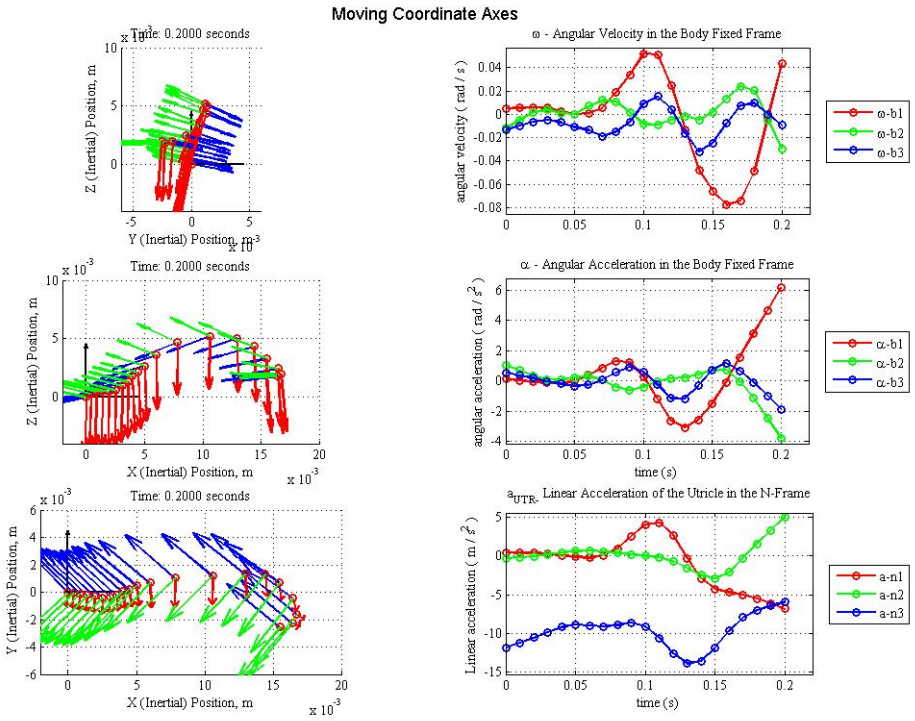

Figure C2: Position Views, Angular kinematics & Acceleration at the utricle in the N-Frame for Trial #2

Position and kinematics for the 2nd feeding trial

On the left, 3 Different views (top to bottom : Front view, Side View, Top View) of the position of the nose marker and the body fixed coordinates attached to the nose with the Tank coordinates as the fixed coordinate system.

On the right, angular velocity (in the B-frame), angular acceleration (in the B-frame), and linear acceleration at the utricle in the N-Frame based on position measurements from Clemson Tests (Trial 1) and measurements from the μ-CT.

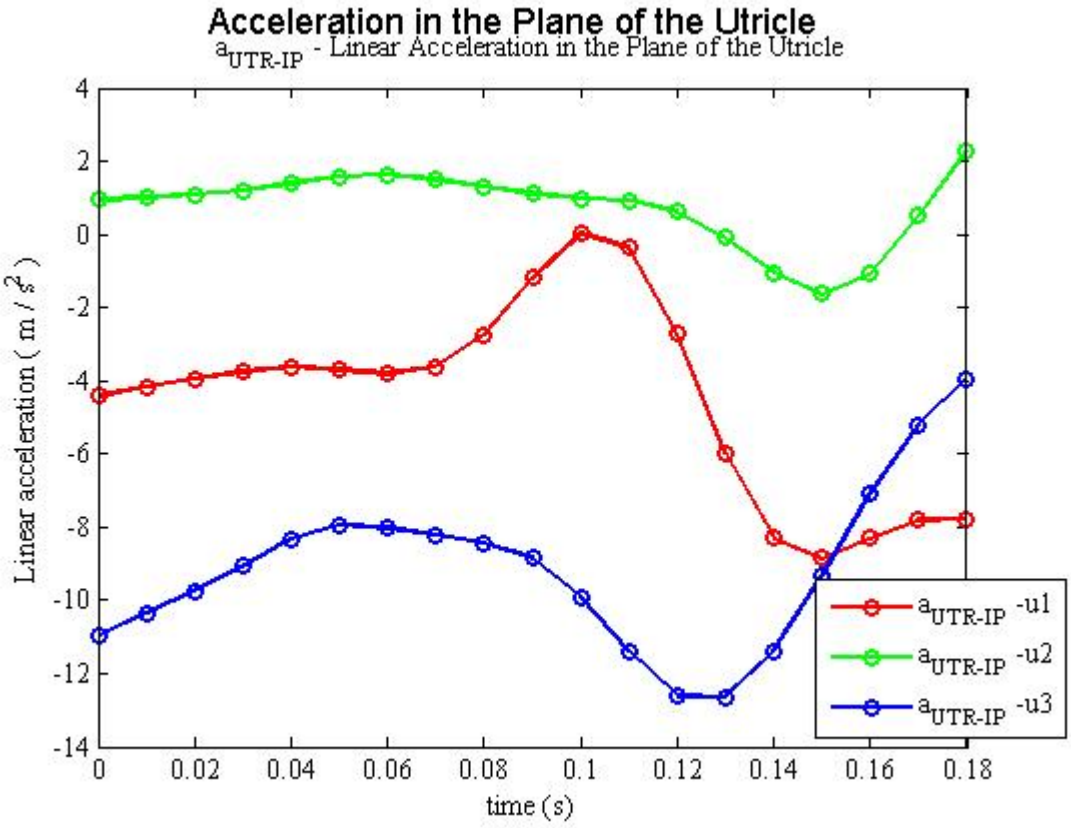

Figure C3: Acceleration in the plane of the utricle – Trial 2

Components of acceleration at the utricle (in the U-Frame) based on measurements from Trial 2.

Here:
u1 is the Anterior-Posterior Direction (+A)
u2 is the Medial-Lateral Direction (+Left)
u3 is the Perpendicular to plane of utricle (+ Dorsal)

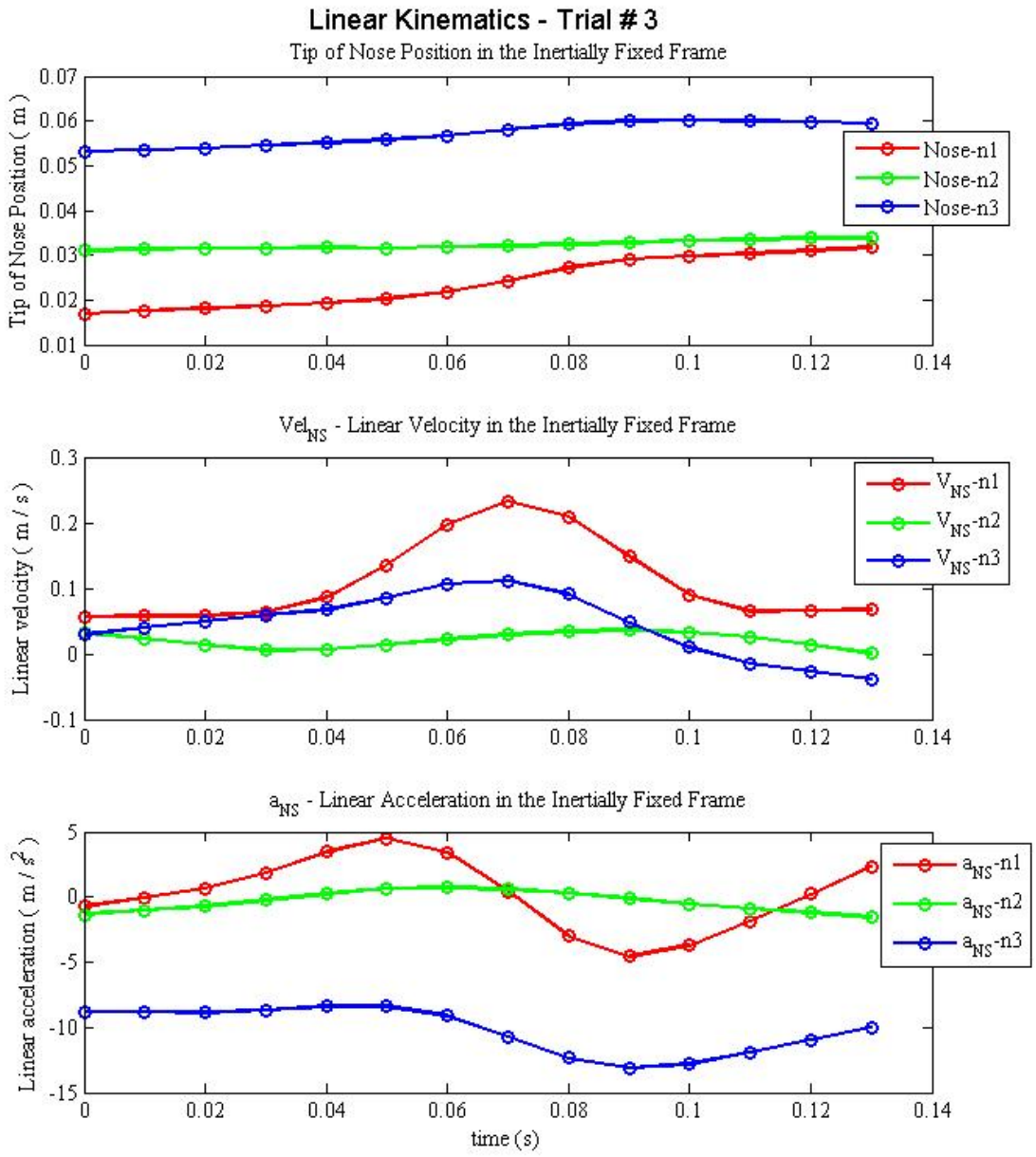

Figure C4: Linear Kinematics - Trial #3

This graph shows the Linear Position, Velocity and Accelerations for the tip of the nose for feeding trial #3. These graphs include gravity acting in the minus n3 direction. There is a maximum acceleration magnitude of 14.102 m/s^2.

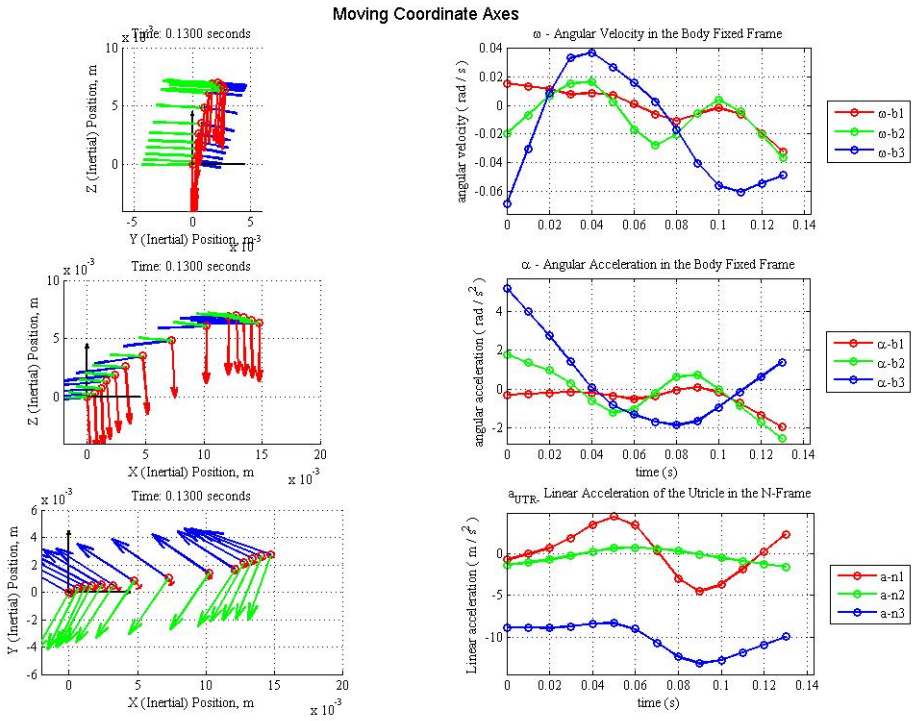

Figure C5: Position Views, Angular kinematics & Acceleration at the utricle in the N-Frame for Trial #3

Position and kinematics for the 3rd feeding trial

On the left, 3 Different views (top to bottom : Front view, Side View, Top View) of the position of the nose marker and the body fixed coordinates attached to the nose with the Tank coordinates as the fixed coordinate system.

On the right, angular velocity (in the B-frame), angular acceleration (in the B-frame), and linear acceleration at the utricle in the N-Frame based on position measurements from Clemson Tests (Trial 3) and measurements from the μ-CT.

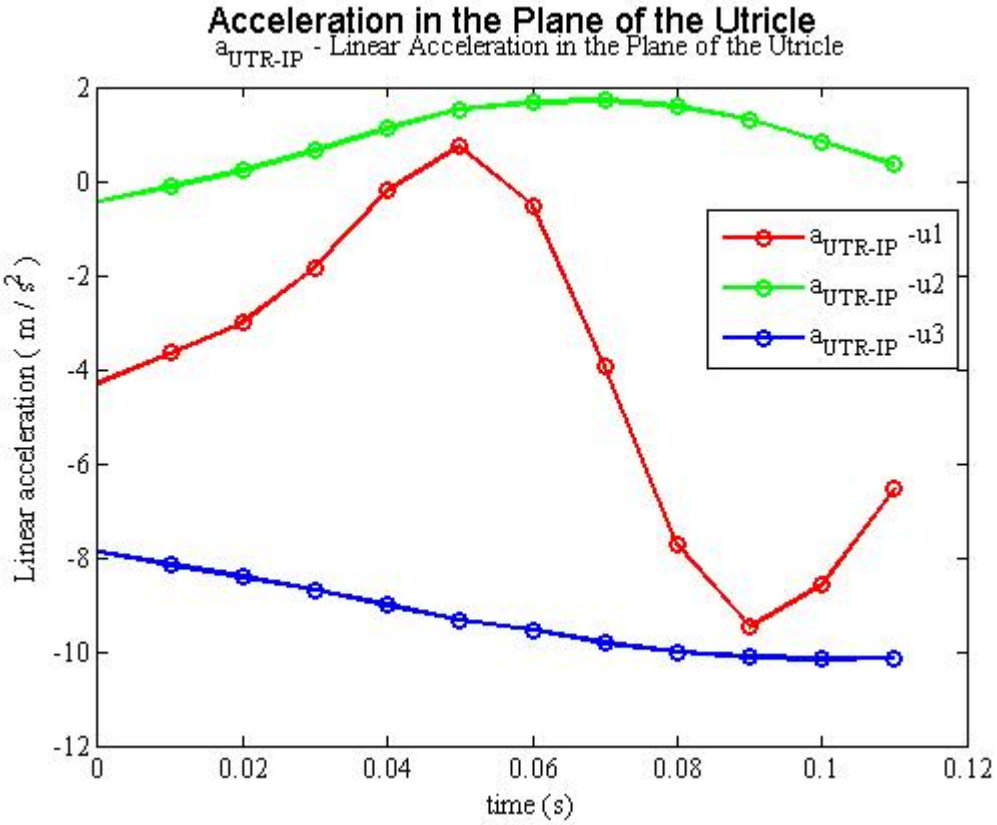

Figure C6: Acceleration in the plane of the utricle – Trial 3

Components of acceleration at the utricle (in the U-Frame) based on measurements from Trial 3.

Here:
u1 is the Anterior-Posterior Direction (+A)
u2 is the Medial-Lateral Direction (+Left)
u3 is the Perpendicular to plane of utricle (+ Dorsal)